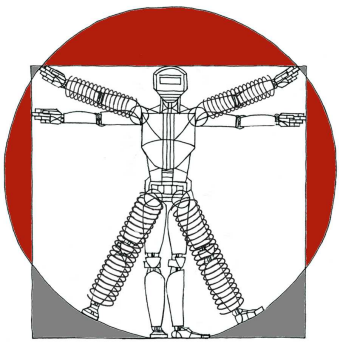

FP7-ICT-2007-3-231554

VIACTORS
Variable Impedance ACTuation: systems embodying advanced interaction behaviORS

Specific Targeted Research or Innovation Project
Seventh Framework Programme
Information Society Technologies IST

Deliverable D5.1
Analysis (definition of metrics), modelling, simulation and control for legged locomotion systems with variable impedance actuators

Deliverable due date: January 31, 2011	**Actual submission date: January 31, 2011**
Start date of project: February 1, 2009	**Duration: 36 months**
Lead contractor for this deliverable: UT	**Revision Status: Draft 1.0**
Reference WP and Tasks: WP5, T5.1-2-3	**Authors: UT**

Project co-funded by the European Commission within the Seventh Framework Programme (2007-2011)		
Dissemination Level		
PU	Public	X
PP	Restricted to other programme participants (including the Commission Services)	
RE	Restricted to a group specified by the consortium (including the Commission Services)	
CO	Confidential, only for members of the consortium (including the Commission Services)	

Executive Summary

This report presents our work on legged locomotion with variable impedance actuators. This first Deliverable of Work Package 5 focusses on analysis, modelling, simulation and control of legged locomotion systems, actuated by variable impedance actuators.

In Chapter 1, we present an analysis of the human gait, and in particular the power flows between knee and ankle. From this analysis, it is shown why humans are energy efficient in locomotion, and how this level of efficiency can be introduced to robotic systems using variable impedance actuation.

Chapter 2 presents an overview of nonlinear oscillation dynamics. The concept of limit cycle oscillations and their relation to locomotion is studied, and it is investigated how variable impedance actuation can improve robustness of the limit cycle. In particular, an analysis of introducing variable impedance actuation in bipedal and hexapedal locomotion is presented.

Since limit cycles are a key concept in legged locomotion, research effort is put into energy efficient actuation of oscillatory motions using variable impedance actuation. Chapter 3 presents a generic port-based model for variable stiffness actuators, which makes explicit the power flows between the controller, the actuator and the load.

From analysis of the same port-based model, Chapter 4 presents a performance measure that provides a measure of how efficient a variable stiffness actuator is in transferring power from the controller to the load. This is an important measure in legged locomotion, because the available energy for actuation is limited due to the mobile nature of the system.

In Chapter 5, two energy efficient control strategies for actuation of periodic motions are presented. The first strategy is based on the analysis of the the port-based model, and is capable of storing disturbance energy during actuation. The effectiveness is illustrated by a simulation of actuation of a oscillation subject to disturbances. The second control strategy actively tunes the natural dynamics of the actuated system to the frequency of the desired periodic motion. Experimental results are presented to validate the approach.

Chapter 6 presents a geometric interpretation of the Zero Moment Point, which is an important concept in legged locomotion. The geometric interpretation presented herein provides a coordinate free description of the ZMP, which can be advantageous in deriving dynamic control laws for legged locomotion systems.

Contents

Chapter 1

Physical Properties of the Human Gait

This Chapter presents an analysis of the human gait. In particular, the principal physical properties of the human gait will be analyzed in order to understand how to apply them in legged locomotion systems and so to obtain a high performance motion.

This Chapter is divided in two Sections: Section 1.1 provides a description of the human gait. In particular, it summarizes the research lead in [1] and [2] on the introduction to human walking and in [3] on the analysis on kinematic, kinetic and muscle activation. Section 1.2 presents an analysis of the human gait in terms of power flow, functionality and biomechanical properties and refers to the work conducted in [4], [5], [6] as part of the REFLEX-LEG project, granted by the Dutch Technology Foundation STW.

1.1 The human gait

The human gait is defined as a composition of repetitive events and, therefore, it is often called *walking cycle* or *gait cycle*. These events are independent of time, so the whole walking cycle can be given as a percentage of the cycle itself. In general, the cycle is considered to start and finish with heel-strike of the same foot, which corresponds to 0% and 100% of the cycle. For the other leg, there is a $180°$ phase shift for the same events.

In most of the studies on human gait, the walking cycle is divided into two main phases:

- *Stance phase* - In this phase, the foot is in contact with the ground (60% of a gait cycle). This phase starts with heel-strike and ends with toe-off of the same foot.
- *Swing phase* - In this phase, the foot is off the ground (40% of a gait cycle). This phase starts with toe-off and ends with the heel-strike of the same foot.

During the cycle, it is possible to highlight three main instants:

- *Heel-strike* - This instant fixes the beginning of the cycle, i.e. 0% or 100%, and it consists of the first contact of the foot with the ground.
- *Push-off* - This instant occurs at the 40% of the gait cycle, i.e. when the heel starts to leave the ground.
- *Toe-off* - This instant occurs at the 60% of the gait cycle, i.e. when the foot completely leaves the ground.

1.2 Properties of the human gait

In this study, we are mainly interested in the healthy human gait from an energetic point of view and we aim to highlight the main features that would be highly interesting for robotic applications, prosthesis and rehabilitation devices.

1.2.1 Power flow during the human gait cycle

In order to grasp the nature of walking, we analyze the bio-mechanical data of the human gait, as been presented by Winter [3]. In particular, Fig. 1.1 depicts the power flow at the knee (upper) and ankle (lower) joints during one complete stride of a healthy human, normalized in body weight. The figure highlights the three instants, i.e. heel strike, push-off and toe-off, and three main phases:

- Stance: the knee absorbs a certain amount of energy during flexion and generates as much as the same amount of energy for its extension. In the meantime, the ankle joint absorbs energy, represented by A_3 in the figure, due to the weight bearing.
- Pre-swing: the knee starts absorbing energy, represented by A_1 in the figure, while the ankle generates the main part of the energy for the push-off, represented by G, which is about the 80% of the overall generation.
- Swing: the knee absorbs energy, represented by A_2 in the figure, during the late swing phase, while the energy in the ankle joint is negligible.

The analysis of the values of energy absorption (corresponding to the areas $A_{1,2,3}$) and generation (G) gives insightful information. It can be noted that, in the healthy human gait, the knee joint is mainly an energy absorber whereas the ankle joint is an energy generator. In particular, the knee absorbs about 0.09 J/kg during pre-swing phase (A_1) and 0.11 J/kg during late swing phase (A_2). On the other hand, the ankle absorbs approximately 0.13 J/kg during stance phase (A_3) and generates about 0.35 J/kg for push-off (G). These values show that there is almost a complete balance between the generated and the absorbed energy, since the energy for push-off generation (G) is almost the same as the total energy absorbed in the three intervals $A_{1,2,3}$.

1.2.2 Modeling

In order to deeply understand how power flows during one complete stride, we present the model of a healthy human in a port-based graphical representation. In particular, we intend to use the bond graph modeling language to visualize the human dynamical behavior so to have an intuitive approach for the design of legged systems.

The basic idea behind this modeling language is that every physical system can be modeled by interconnecting simple elements, which are characterized by a particular port behavior [7]. The interconnections are realized through bonds, which represent the power flow between the different elements. The generalized representation of the power flows is made through a Dirac structure $\mathcal{D}$, as depicted in Fig. 1.2. The multi-bonds allow any number of storage elements $\mathbb{C}$ or $\mathbb{I}$, dissipative elements $\mathbb{R}$ and of external inputs $\mathbb{S}_{f,e}$

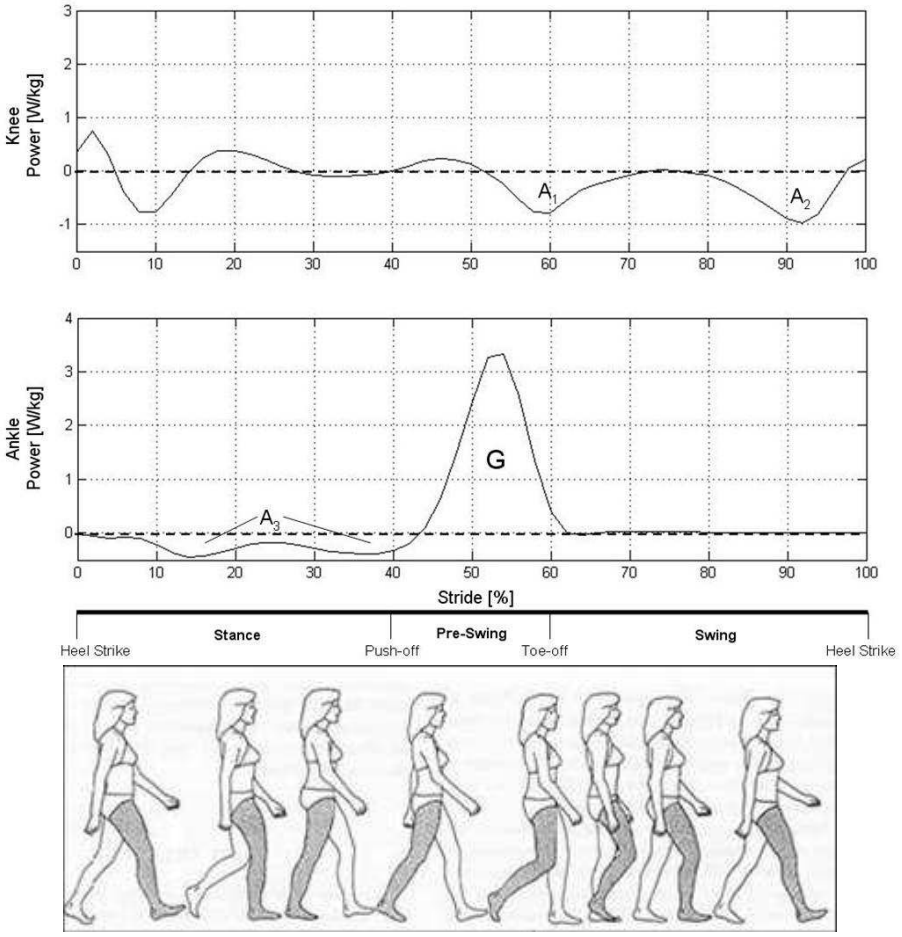

Figure 1.1: The power flow of the healthy human gait normalized in body weight in the knee (upper) and the ankle (lower) joints during one stride [3]. The areas $A_{1,2,3}$ indicate the energy absorption, whereas G indicates the energy generation. The cycle is divided into three phases (stance, pre-swing and swing) with three main instants (heel-strike, push-off and toe-off).

(source of flow or effort, respectively velocities and forces in the mechanical domain). Note that the Dirac structure is power continuous and not necessarily constant.

We now detail the generic representation of the Dirac structure of Fig. 1.2 for the specific case of the human dynamics, with the aim of visualizing how the power flows between the joints of the leg during a healthy gait, according to the data presented in [3] and plotted in Fig. 1.1.

The scenario is depicted in Fig. 1.3. Let $\mathbb{I}_t$, $\mathbb{I}_{ul}$, $\mathbb{I}_{ll}$ and $\mathbb{I}_f$ be the inertia of torso, upper leg, lower leg and foot, respectively. Let g be gravity, i.e. a source of effort, and $\mathbb{S}_e$ a source of effort, namely the torque exerted by the hip. The 1-junctions are flow junctions and are characterized by the property that all the connected bonds are constrained to assume the same flow value, i.e. the same velocity. In particular, the figure presents three 1-junctions that indicate the angular velocities of the hip, knee and ankle joints. In the junction structure, the kinematics of the leg can be recognized. The Dirac structures $\mathcal{D}_i$, with $i = 1, \cdots, 4$ realize the interconnections between the different parts of the system and regulate how the energy is flowing. Finally, after analyzing the data in Fig. 1.1, we introduce three storage elements $\mathbb{C}_1$, $\mathbb{C}_2$ and $\mathbb{C}_3$, which are representing the muscle activity. In

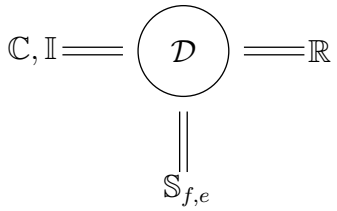

Figure 1.2: Generalized representation of power flow in a dynamical system - The Dirac structure $\mathcal{D}$ defines the power-conserving interconnections between the different bonds and, therefore, how power is distributed among the ports. The multi-bonds allow any number of storage elements $\mathbb{C}$ or $\mathbb{I}$, of dissipative elements $\mathbb{R}$ and of external power source $\mathbb{S}_f$ or $\mathbb{S}_e$.

particular, they are in charge of storing the absorbed energies A_1, A_2 of the knee and A_3 of the ankle, respectively. The element $\mathbb{C}_2$ facilitates the energy transfer from the knee to the ankle, i.e., the coupling between the knee and the ankle joints. No dissipation element $\mathbb{R}$ is considered.

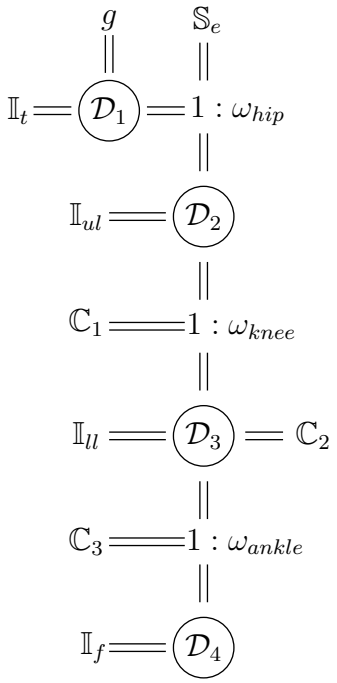

Figure 1.3: Power flow in the human gait - The Dirac structures $\mathcal{D}_i$, with $i = 1, \cdots, 4$ define the power-conserving interconnections between the different bonds, i.e. the different inertias of the human leg ($\mathbb{I}_t$, $\mathbb{I}_{ul}$, $\mathbb{I}_{ll}$ and $\mathbb{I}_f$ of torso, upper leg, lower leg and foot), the joints characterized by angular velocities ω_{hip}, ω_{knee}, ω_{ankle}, the hip torque $\mathbb{S}_e$, the gravity g, the storage elements $\mathbb{C}_1$, $\mathbb{C}_2$, $\mathbb{C}_3$.

1.2.3 Analysis of the power flow

During human gait, the power flows from one joint of the leg to another. The core of the analysis of the gait consists in the consideration that human muscles are in charge of efficiently transferring the energy between the leg joints. The energy generated by the

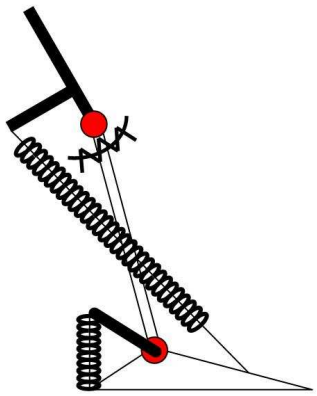

Figure 1.4: The conceptual sketch presents three storage elements, one torsional spring at the knee joint, one linear spring between upper leg and foot via a lever arm and one linear spring at the ankle joint via a second lever arm.

ankle for push-off (G in Fig. 1.1) is balanced by the total energy absorbed by the knee during pre-swing and late swing (A_1 and A_2) and by the ankle (A_3) during stance. This means that the ankle, in order to generate a quantity of energy in an efficient way, should exploit the energy absorbed by the knee. Therefore, a coupling between the knee and the ankle joints in terms of energy is at the basis of the efficient human gait: the energy absorbed by the knee should be transferred to the ankle.

This evaluation is crucial in the design of legged systems and, therefore, a passive and efficient legged system should rely on energy transfers between the ankle, i.e. the main generator, and the knee, i.e. the main absorber. This can be realized through properly designed storage elements. The three elements $\mathbb{C}_1$, $\mathbb{C}_2$, $\mathbb{C}_3$ in Fig. 1.3 energetically couple the knee and the ankle joints so to obtain an exchange of energy from the absorption intervals $A_{1,2,3}$ to the generation G.

Following this discussion, we summarize this concept in Fig. 1.4, in which we introduce:

- one torsional elastic element $\mathbb{C}_1$ at the knee joint, responsible for the absorption A_1 during the pre-swing phase and for the transfer of this energy to the elastic element $\mathbb{C}_2$, by releasing it during the swing phase.

- one linear elastic element $\mathbb{C}_2$, which physically connects the upper leg (via a lever arm) and the foot and, therefore, couples the knee and ankle joints. This element is responsible for the absorption A_1 (received from $\mathbb{C}_1$) and A_2 during the swing phase and for a part of absorption $A3$ during the stance phase.

- one linear elastic element $\mathbb{C}_3$ connected between heel and a lever arm fixed on the ankle joint and responsible for the main part of the absorption A_3 during the stance phase.

It is assumed that the knee joint absorbs and generates the same amount of energy during stance phase, therefore for this phase, the knee joint is not considered as a contributor to the ankle push-off generation. For this reason, elastic elements to mimic this behavior are not included in the conceptual design.

1.2.4 Analysis of the stiffness

In order to highlight the functionality of the knee and the ankle joints, we analyze the relations between the torques and the corresponding angles, normalized in body weight, during one complete walking cycle at natural cadence.

Fig. 1.5 shows the plot of the knee torque with respect to the knee angle. By examining the figure, it is possible to observe that from heel-strike to full-extension (approximately 52% of the gait), the knee joint presents an elastic behavior, for both absorption and generation, which is approximately linear. Following the full-extension of the knee joint, energy exchange between the ankle and knee joint takes place. Around this point, some portion of the kinetic energy due to push-off generation is absorbed by the knee joint during flexion of the knee, until the full-flexion point with a nonlinear elastic behavior. This behavior can be considered as pseudo-elasticity due to similarity of the loading behavior at the knee joint during this part of the swing period (pre-swing phase). After that, the knee joint shows approximately linear elastic behavior until the end of the swing period.

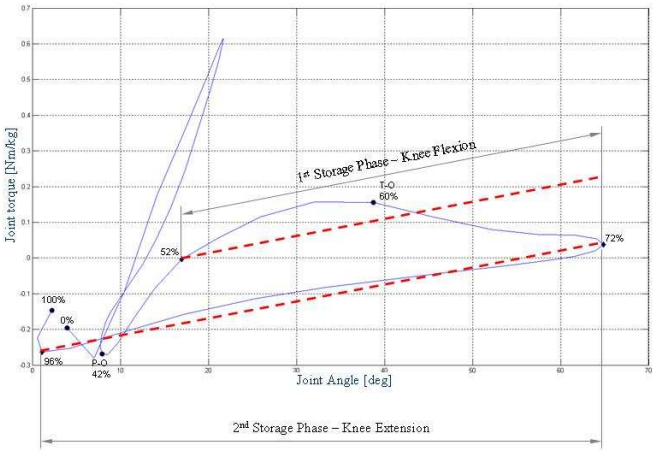

Figure 1.5: Knee angle vs knee torque during one stride of natural walking. The dashed lines indicate the elastic behavior of the joint and highlight the two storage phases during the swing period. Heel-strike at 0%, push-off at 47% and toe-off at 60% of the walking gait are highlighted to better visualize the functional behavior of the knee joint.

In order to reproduce this elastic behavior of the knee joint, we can determine the elastic constant for a legged system mimicking a human behavior. A line between the points referring to 52% and 72% (pre-swing phase) and a second line between the points referring to 72% and 96% (late swing phase) can identify approximately the elastic behavior requirements of the legged system. Therefore, the torsional elastic constant can be determined by

$$\tau_k = K \times \theta_k$$

where τ_k is the joint torque in Nm/kg, θ_k is the joint angle during late swing phase in radiants, and K is the torsional elastic constant in Nm/kg/rad.

The torque provided by the linear swing storage element can be obtained by the equation

$$\tau = L \wedge F_s$$

where L is the position vector between the force F_s exerted by the spring and the knee

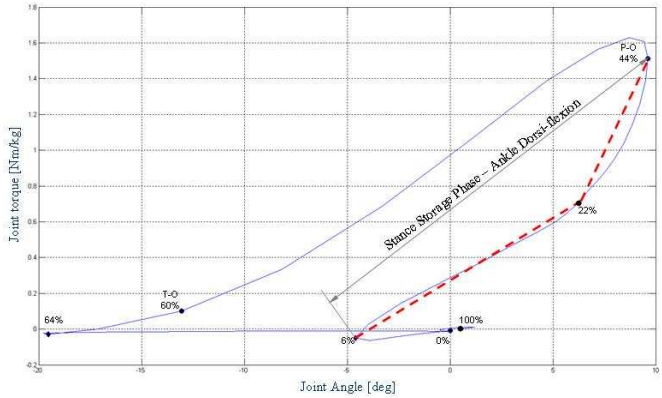

Figure 1.6: Ankle angle vs ankle torque during one stride of natural walking. The dashed lines indicate the elastic behavior of the joint and highlight the storage phase during stance period. Heel-strike at 0%, push-off at 47% and toe-off at 60% of the walking gait are also highlighted to better visualize the functional behavior of the ankle joint.

joint. From this expression linear elastic constant can be found by

$$F_s = K_s \times \delta s$$

where K_s is the elastic constant of the element for swing storage, δs is the length change of the elastic element during late swing phase.

Fig. 1.6 shows the plot of the ankle torque with respect to the ankle angle. By examining the figure, it is possible to observe that from heel-strike to flat foot (approximately 6% of the gait) the ankle joint presents an elastic behavior, for absorption, which is approximately linear. Following the flat foot, dorsi-flexion action takes place during the loading of the ankle due to weight bearing. This action shows stiffening elastic behavior, until around the push-off point, which is the roll-over part of the stance period. This elastic behavior can be approximated by two linear elastic loading actions, which are represented by two dashed lines in the figure. After that, planter-flexion of the ankle joint takes place with the elastic unloading, until the point of toe-off. Small energy generation takes place with approximately linear elasticity in order to have foot clearance from the ground. Between this point and the end of the stride the action of the ankle joint can be neglected, which shows the chance of the decoupling of the two joints during swing period.

In order to reproduce this elastic behavior of the ankle joint, we can determine the elastic constant for the legged system mimicking a human behavior. Two lines between the points referring $6\% - 22\%$ and $22\% - 44\%$ (roll-over phase) can identify approximately the elastic behavior requirements of the legged system. Therefore, torsional elastic constant can be determined, such as

$$\tau_{a_{1,2}} = K_{1,2} \times \theta_{a_{1,2}}$$

where $\tau_{a_{1,2}}$ is the ankle joint torque in Nm/kg, $\theta_{a_{1,2}}$ is the ankle joint angle during roll-over phase in degrees, and $K_{1,2}$ are the torsional elastic constants in Nm/kg/rad.

The torque provided by the stance storage element can be obtained by the equation

$$\tau = L \wedge F_s$$

where L is the position vector between the force F_s exerted by the spring and the joint.

From this expression, the linear elastic constant can be found by

$$F_s = K_s \times \delta s$$

where K_s is the elastic constant of the element for stance storage, and δs is the length change of the elastic element during roll-over phase.

The foregoing analysis provides a way to approximate the behavior of muscle activity in the ankle and knee by linear springs. Based upon the conceptual design described in Fig. 1.4, we have realized a working prototype, which makes use of only two elastic elements, i.e., $\mathbb{C}_2$ and $\mathbb{C}_3$ [4], [5]. However, Fig. 1.5 and Fig. 1.6 show that muscle activation is more complex than a linear approximation can capture. Hence, it is expected that, if a variable stiffness can be realized that can reproduce the apparent behavior shown in Fig. 1.5 and Fig. 1.6 sufficiently accurate, performance can be improved. However, a gain of performance can only be expected if changing the variable stiffness itself can be achieved efficiently. This desired functionality is available in the form of variable stiffness actuators that can change their apparent output stiffness in an energy efficient way. This class of variable stiffness actuators is described in Chapter 3.

Chapter 2

Limit Cycle Walking

The goal of this Chapter is to present and analyze the nonlinear oscillation dynamics from a mathematical point of view, and to study these dynamics in the context of walking. The gait of a *planar compass* walker is analyzed, and a performance comparison of a planar biped robot with rigid and compliant legs is carried out. In addition, gait pattern generation in hexapedal walking is analyzed.

This Chapter is organized as follows: in Section 2.1, we present the mathematical background on limit cycle and refers to [8],[9], [10] and [11]. Section 2.2 presents a performance comparison of a planar bipedal robot with rigid and compliant legs. This Section refers to [12]. In Section 2.3, gait pattern generation with compliant joints is investigated for a hexapod walker.

2.1 Nonlinear Oscillation Dynamics

In the previous Chapter, we analyzed the physical properties of the human gait, in order to understand how to obtain a high performance also in the motion of robotic systems in terms of both robustness and efficiency. In particular, we intend to use a bio-mimetic paradigm to study the nonlinear dynamics of legged locomotion systems with a biological insight. This bio-mimetic paradigm suggests that the combination of limit cycles of internal motions (e.g. periodic motions in the phase space) and constraints with the ground (intermittent ground contact) results in robust and efficient locomotion of the total system. Therefore, we want to understand the nonlinear oscillation dynamics and their synchronizations, and use this knowledge as search guideline for the design of new robotic morphologies.

Research on dynamic walking was initiated by McGeer [13] in the early nineties. Originally inspired by toys, he developed several passive walking mechanisms that could walk down a shallow slope only powered by gravity. From his results the view emerged that dynamic walkers could be created based on the same principle, with the addition of actuators to provide energy instead of using gravity. The stable gait of a dynamic walker can be interpreted as a stable limit cycle of the system [14]. Once the walker has converged to the stable gait, it keeps repeating the same pattern over and over again. Unfortunately, the dynamic walkers that have been built so far suffer from a lack of robustness. The stability of the gait is easily destroyed by even relatively small disturbances, usually resulting in the robot falling down. Apparently, the limit cycle of the system, although being stable, has only a small basin of attraction. Current research is

focused on improving this shortcoming and is expected to yield more robust behavior.

The dynamics of a walking robot are generally nonlinear and on top of that, the regular impacts with the ground causes a switching behavior that makes it difficult to understand the dynamics of these systems in an analytical way. This explains why the current generation of dynamic walkers is more often a result of trial and error and parameter optimization rather than a thorough analysis of the dynamic behavior that is responsible for the stable limit cycle oscillation.

2.1.1 Definition of a Limit Cycle

A *limit cycle* is a periodic solution of a differential equation with the additional property that it is isolated. In the phase space of the system, a periodic solution is a trajectory that is a closed orbit. Isolated means that any neighboring trajectory of the limit cycle is not closed, they spiral either towards or away from the limit cycle. Mathematically, it could also be said that there exists an open neighborhood that contains only one periodic solution. If all neighboring trajectories spiral towards the limit cycle it is *stable* or *attractive*, otherwise it is *unstable* or *half-stable* in some exceptional cases, as depicted in Figure 2.1. For the design of robust walking robots it is interesting to look at stable limit cycles, with a basin of attraction that is as large as possible. The possibility of a limit cycle solution is restricted to nonlinear systems. In a linear system, if $x(t)$ is a solution then because of linearity also $c\,x(t)$ is a solution for any constant c. In the phase space, this can be seen as an infinite number of closed trajectories encircling the single equilibrium point in the origin. However, none of these trajectories is isolated, and therefore not a limit cycle.

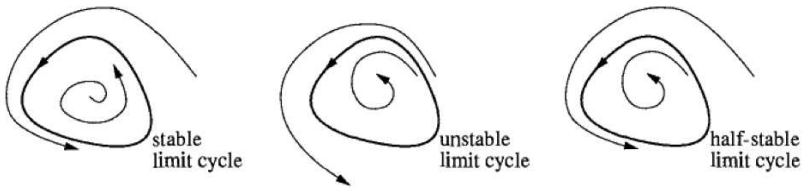

Figure 2.1: Limit cycle.

2.1.2 Lienard systems

There exist nonlinear systems which are known to have a globally attractive limit cycle. An example is the famous Van der Pol oscillator that is described by:

$$\ddot{x} + \mu(x^2 - 1)\dot{x} + Kx = 0 \tag{2.1}$$

The equation is similar to the damped harmonic oscillator but with a nonlinear damping term $\mu(x^2 - 1)\dot{x}$. For $\mu > 0$, the damping term is negative for $\mid x \mid < 1$ and positive for $\mid x \mid > 1$. This results in small amplitude oscillations being pumped up, while large amplitude oscillations are damped down. Intuitively it is understandable that this must lead to a stable oscillation of intermediate amplitude, as depicted in Figure 2.2.

An oscillator closely related to the Van der Pol oscillator is the Rayleigh oscillator that is based on the same principle. In this oscillator the damping term only depends on the

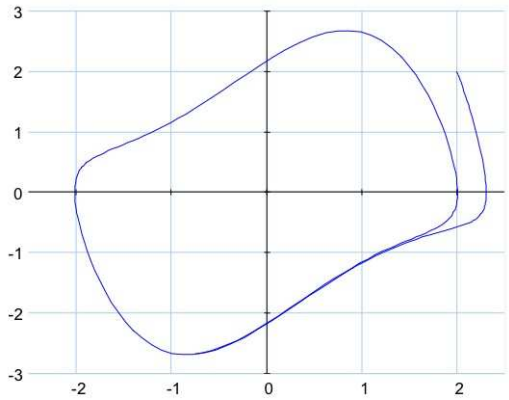

Figure 2.2: Phase diagram of the Van der Pol oscillator.

derivative $\dot{x}$. The equation describing the Rayleigh oscillator is:

$$\ddot{x} + \mu(\dot{x}^2 - 1)\dot{x} + Kx = 0 \tag{2.2}$$

The relation between the two oscillators described above can be found by first differentiating (2.2) with respect to time and then replacing $\dot{x}$ with y. The phase diagram of the Rayleigh oscillator is shown in Figure 2.3

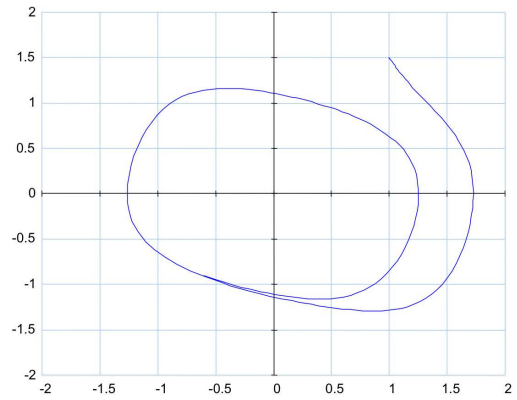

Figure 2.3: Phase diagram of the Raleigh oscillator.

The Van der Pol equation is a specific case of a Lienard system as described by the equation below:

$$\ddot{x} + f(x)\dot{x} + g(x) = 0 \tag{2.3}$$

Here $f(x)$ and $g(x)$ may be nonlinear functions. Lienard theorem states that (2.3) has a unique, stable limit cycle surrounding the origin of the phase space if the following conditions are satisfied [8]:

1. $f(x)$ and $g(x)$ are continuously differentiable for all x
2. $g(-x) = -g(x)$, $\forall x$, i.e. $g(x)$ is odd
3. $g(x) > 0$ for $x > 0$
4. $f(-x) = f(x)$, $\forall x$, i.e. $f(x)$ is even

5. The odd function $F(x) = \int_0^x f(u)du$ has exactly one positive zero at $x = a$, is negative for $0 < x < a$, is positive and nondecreasing for $x > a$, and $F(x) \to \infty$ as $x \to \infty$

The conditions on $g(x)$ ensure that its behavior is like that of a restoring force, like a spring, and the conditions on $f(x)$ ensure a damping behavior that amplifies small amplitude oscillations, but dampens large amplitude oscillations. More information on nonlinear oscillators and nonlinear dynamics in general can be found in books such as [8, 9, 10].

2.1.3 Passivity based oscillators

Another approach to the analysis of limit cycle oscillations is taken in [15]. Here the authors use dissipativity theory to characterize oscillators as open systems. This makes it possible to interconnect a network of oscillators and analyze their common behavior. The passivity approach is useful because it allows looking at system connections from an energy based point of view.

A system is passive with respect to its input $u(t)$ and output $y(t)$ if there exists as storage function $S(x(t)), S(0) = 0$ such that:

$$S(x(t)) \geq 0 \quad \text{and} \quad \dot{S}(x(t)) \leq u(t)y(t) \tag{2.4}$$

Starting point for the analysis in [15] is the above described Van der Pol oscillator and the Fitzhugh-Nagumo oscillator, which is a simplified model of spike generation in neurons. The author generalizes these two types of oscillators to a form as shown in Figure 2.4. The forward path consists of a passive system and the negative feedback is formed by a nonlinearity $\phi_k(y)$ that is the sum of a passive part $\phi(y)$ and an anti-passive or active part $-ky$, such as:

$$\phi_k(y) = \phi(y) - ky$$

Here $\phi(y)$ is a smooth, static nonlinearity in the sector $(0, \infty)$ (thus passive), and moreover $\phi(y)$ is a stiffening nonlinearity, i.e. $\lim_{|y|\to\infty} \frac{\phi(y)}{y} = \infty$. Now take as $G_k(s)$ the system formed by the linearized passive system with negative feedback $-ky$. Increasing k will eventually lead to instability of $G_k(s)$ as poles cross the imaginary axis and move onto the right half s-plane. Define k^* the smallest $k > 0$ for which $G_k(s)$ has a pole on the imaginary axis.

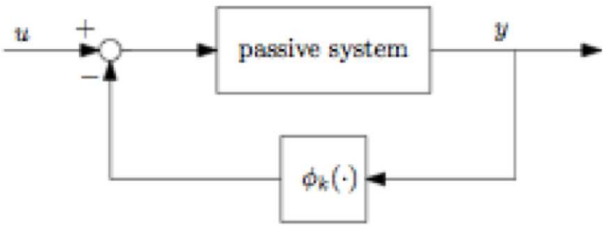

Figure 2.4: Passive system with nonlinear feedback.

Under the assumption of absolute stability of the system shown in Figure 2.4 for $k = k^*$ two scenarios are possible:
Scenario 1 - Van der Pol type: For $k = k^*$ a pair of complex conjugate poles cross the imaginary axis at non- zero speed causing a supercritical Hopf bifurcation. In this

bifurcation the stable origin becomes unstable and a stable limit cycle emerges from the origin.
Scenario 2 - Fitzhugh-Nagumo type: For $k = k^*$ a single pole crosses the imaginary axis causing a pitchfork bifurcation that results in a bistable system. Extending the negative feedback with a slow adaptation mechanism $\frac{1}{\tau s+1}$ transforms the bistable system into a system with a globally stable limit cycle.

In the isolated case where the system is not connected ($u = 0$), the system will exhibit a self-sustained stable limit cycle oscillation for $k >\sim k^*$. The existence of this limit cycle is not guaranteed for all $k > k^*$, since further bifurcations may occur that alter the system behavior.

2.2 Performance comparison of a planar bipedal robot with rigid and compliant legs

Bipedal walking is the main form of locomotion for humankind. Although it is very easy for us to walk, making a robot to have a human-like gait is not easy due to the complex dynamics of walking. The interest in building human-like walkers is motivated by the applications in rehabilitation to the field of entertainment [14].

After the introduction of the model of the simplest passive dynamic walker by McGeer [13], the research area of dynamic walking has received a lot of interest in robotics. A passive dynamic biped shows a human-like gait, and it can walk faster than so-called static walkers. Comparing to static walking machines, the passive dynamic walking approach moves towards simple and low-gain control and emphasizes on the passive dynamics of the legs. Moreover, this approach aims at obtaining an overall stability for the system *over the course of multiple steps* [14], instead of stability at each step.

Since a walking machine should carry its source of energy, one of the challenging problems in this field is reducing the cost of energy of the robot. In addition, robustness of a passive walker is a critical issue. Some studies [16] showed that the stability of a passive walker can be improved by increasing the dissipated energy (adding passive dissipative elements in the joints). Therefore, a trade-off should be pursued to achieve both energy efficiency and robustness.

The motivation behind this work is to increase the robustness of a passive walker by adding a passive compliance (springs) along the robot legs. At each step, the compliant elements store part of the impact energy associated with foot impact. By absorbing this impact energy, the robustness of the walker can be increased, because the hip dynamics are isolated from the ground impacts, which can disturb the gait (e.g. during a step down). It is noted that the springs cannot absorb arbitrary amounts of energy, because the gait must still be sustained. By adding the compliance along the legs, we thus expect robustness to be increased, while still maintaining an energy efficient gait.

So far, several studies have been done on ideal compliant legs [17] and compliant hip/ankle joint walking robots [18]. However, a desired performance meeting the requirements of energy efficiency and robustness has not been achieved yet.

This Section is organized as follows. In Sec. 2.2.1, we explain the port-based model of the passive walker with compliant ground contact. It should be noted that in this Chapter, the term *compliant element* refers to both ground stiffness, used in the contact model, and the springs, placed along the legs. In Sec. 2.2.2, the results of numerical analysis of the

model are reported. The idea of applying a passive storage element to the model is presented in Sec. 2.2.3, in which simulation results are presented and discussed.

2.2.1 The Planar Passive Bipedal Walker

In this Section, we describe the model of the planar bipedal walker. The model has the mass configuration of the simplest passive walker over a gentle slope, introduced in [19], with two main differences. First, the ground contact model is not assumed to be rigid but compliant. Second, the feet are arc-shaped, although their radius is small compared to the leg-length.

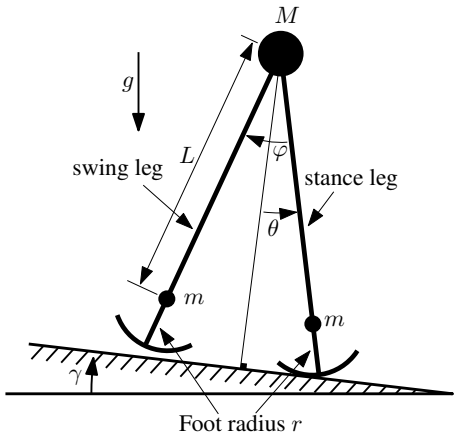

Figure 2.5: The passive walker over a slope. θ is the angle of the stance leg with respect to the slope normal, φ is the angle between the stance leg and the swing leg, γ is the slope angle, M is the hip mass, $m \ll M$ is the foot mass, L is the leg length (from the center of the hip to the center of the foot), r is the foot radius, g is the gravity.

Model configuration

The model, shown in Fig. 2.5, has two rigid massless legs of length L connected by a frictionless hinge at the hip. It is composed of three point masses, a mass M at the hip and masses $m \ll M$ at the each of the feet. The feet have a curved shape with radius r. Due to the chosen mass ratio, the influence of the swing leg on the motion of the hip can be neglected, which makes the equations of motion fairly simple.

The biped walks down a gentle slope, with angle γ, and is actuated by the gravity g. As a result of not having knees, a non-physical property for the model is assumed that let the swing leg to briefly pass through the slope surface during the mid-stance phase (foot scuffing).

The configuration variables of the system are: the angle θ of the stance leg with respect to the slope normal and the angle φ between the stance leg and the swing leg. The equations of motion of the system are comparable with the equations of a simple double pendulum, representing the angular momentum balance of the whole system around the stance foot, and the angular momentum balance of the swing leg around the hip. The physical properties for the implemented model are: hip mass $M = 3$ kg, feet mass $m = 0.1$ kg, leg length $L = 0.7$ m, feet radius $r = 0.05$ m.

Contact model

During walking, the feet of the biped interact with the ground. We distinguish three phases of interaction: impact (the instant of going from a non-contact state to a contact state), contact, and contact-loss (the instant of going from a contact state to a non-contact state). Generally, there are two main approaches towards modeling such interaction of two rigid bodies: the rigid [14, 19] and the compliant model [20].

In rigid contact, the impact force is modeled as an impulsive force. During the contact phase, the exact contact force is calculated that keeps the relative acceleration of the two bodies equal to zero, *e.g.*, with Lagrangian multipliers. The tricky part is determining contact-loss; it needs to be checked if, when there is no contact force, the two bodies would bump into each other. One of the ways to solve this is by using Linear Complementarity Problem solving techniques [21]. In the case of a two-dimensional passive walker the implementation of the model during contact phase can be simplified by modeling the contact point as a simple hinge and assuming that contact loss takes place if and only if the other foot hits the ground. Care should be taken however, because this does not always reflect what happens in nature, *e.g.*, a negative normal force is impossible in reality, but can easily occur in the model.

For a passive walker, using a rigid contact model implies a fully plastic impact and an instantaneous double support phase. Since the different phases of interaction require different models, the system needs to be modeled as a hybrid system. Such models are generally not easily extensible (*e.g.*, by adding a spring). Also, since the interaction of a robot with the ground in the real world is not infinitely stiff, a rigid contact model is not closely correlated with reality.

The compliant contact model describes the impact phenomenon as a result of changes in the deformation and compression of the surfaces of the bodies due to their elasticity and damping properties. This model is capable of describing the interaction between two rigid bodies by approaching them as just being very stiff, *i.e.*, the deformation of the bodies is very small [20]. The compliant model can approach the rigid model arbitrarily close by choosing a high stiffness. In addition to the conformity to the nature of impact, the implementation of the compliant model is much simpler than the rigid model [22]. For a passive walker, using a compliant contact model implies that the double support phase is not instantaneous, *i.e.*, for a short while both feet are penetrating the ground simultaneously.

To formulate the compliant contact model, we use the Hunt-Crossley model. This model represents the contact force by a nonlinear spring-damper in which the damping coefficient is dependent on the penetration depth, *i.e.*,

$$F(z) = \begin{cases} Kz^n(t) + \lambda z^n(t)\dot{z}(t), & z \geq 0 \\ 0, & z < 0 \end{cases}$$

where K is the spring (elastic) constant, λ is the damping constant, z is the penetration depth, and n is a real number, usually chosen to be unity [22].

Port-based representation

The implementation of the planar passive biped with compliant contact is done in a port-based framework using the 20-sim [23] simulation program. The motivations behind

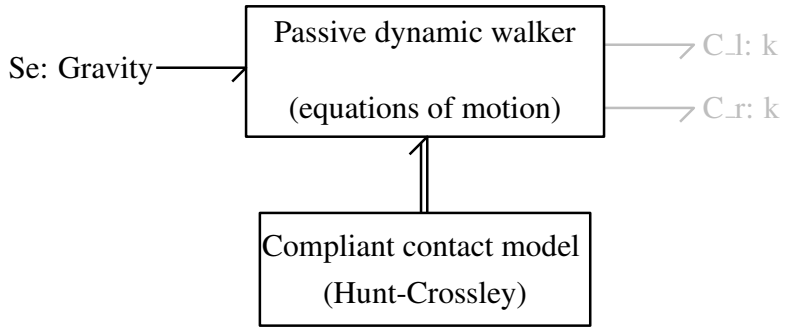

Figure 2.6: Port-based representation of the passive walker. The sub models are linked together with energy exchanging bonds. The C elements represent ideal springs with a fixed stiffness k placed along the each of the legs after as an extension to the model.

using a port-based model are the simplicity of the implementation, the ease of future extension, and the possibility of energy-based analysis. The energy-based bond graph representation makes it easy to model a system by splitting it into subsystems that are interacting with each other via port variables, called *flow* and *effort*, whose product defines the exchanged power. This way of modeling offers a unified way to model physical systems from different physical domains.

Fig. 2.6 shows the port-based representation of the passive compass walker. To have an impression of the simplicity of future extension, two springs with stiffness k are connected to the model. The connection point refers to the joint that the spring is located along it, *i.e.*, left/right foot-leg joint. This way, the rigid legs are replaced by compliant legs. The contact model is defined as a sub-system which is interacting with the dynamic of the robot. In order to simulate fast yet accurately, the *backward differentiation method* was chosen as integration method. For the model used in this study, the stiffness and damping properties of the ground were set to $K = 10^6$ N/m and $\lambda = 5.2 \cdot 10^7$ Ns/m^2. The value of the stiffness is a design choice to provide the steady-state penetration depth of 10^{-5} m. For the chosen stiffness, the damping coefficient was calculated by maximizing the dissipated energy of the impact, *i.e.*, the exchanged energy of Hunt-Crossley model.

2.2.2 Analysis of the Model

In this Section, after introducing the system state, we analyze the stability, robustness and energy of the modeled passive dynamic walker. The aim is to have a base to compare these properties with the walker with compliant legs.

System state and leg swapping

Considering the configuration variables of the system (as mentioned in Sec. 2.2.1), the state of the system is $x = \left[\theta\ \dot{\theta}\ \varphi\ \dot{\varphi}\right]^T$. At each step the right and left leg swap the role of stance and swing leg. For a passive walker with rigid contact model, the role of the legs is switched at the instant of double support, *i.e.*, when the geometric condition $\varphi = 2\theta$ is satisfied and the legs are not parallel [19]. Because of the switching of the legs, the state representation also changes instantaneously: $\varphi^+ = -\varphi^-$, $\theta^+ = -\theta^-$, where $\bullet^-$ denotes the

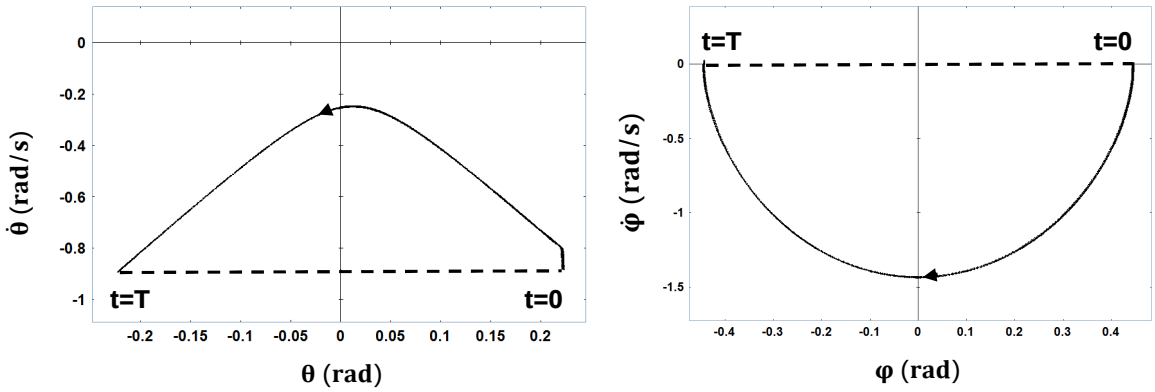

Figure 2.7: The phase plots (limit cycles) of the planar passive walker with rigid legs and compliant ground contact model over the slope angle $\gamma = 0.012$ rad. After some steps, the system state converge to this limit cycles, then each step starts at $t = 0$ and ends at $t = T$. The dashed lines show the leg-swapping moment. The discontinuity in the plot of θ is as a result of the sudden change of the velocity of the stance phase upon impact with the ground.

value before leg switching and $\bullet^+$ the value after leg switching. The values for $\dot{\varphi}^+$ and $\dot{\theta}^+$ can be calculated by using the impact equations, as described in [19].

When using the compliant model, the double support phase is non-instantaneous, hence there is freedom in choosing when to swap the role of the legs. In order to keep the results comparable to the rigid case used by other researchers, we choose to switch the role of the legs when the penetration depth of both feet is equal, *i.e.*, again when the condition $\varphi = 2\theta$ is satisfied. Since both feet are in contact with the ground, the legs cannot move relatively to each other, *i.e.*, $\dot{\varphi} \approx 0$. Hence the system full state x^+ just after leg switching can thus be described by the reduced state $\tilde{x} = \left[\theta\ \dot{\theta}\right]^T$. We define a Poincaré section at this moment when the state of the system is reduced to two. We call this moment *the start of a new step*. The analysis of stability and robustness are done at this moment because of the decrease in system dimension.

Stability

If a passive walker over a slope starts to repeat a pattern after some walking steps, it means that it manages to continue walking without falling down. This periodic pattern is a limit cycle. By definition, a limit cycle is an isolated closed trajectory, which means that other neighboring trajectories either diverge from or converge towards it [8]. The definition of stability for a limit cycle indicates that, if all trajectories in a neighborhood of the limit cycle approach towards it, it is a stable or attractive limit cycle. Fig. 2.7 shows the limit cycles for the two variables φ and θ obtained for the modeled walker over the slope angle of $\gamma = 0.012$ rad.

To verify the stability of a limit cycle, the linearization of the stride function S around the *fixed point* $\tilde{x}^*$ is used. The stride function $\tilde{x}_{k+1} = S(\tilde{x}_k)$ is a Poincaré map that, given the reduced state $\tilde{x}_k$ at the start of step k, returns the reduced state $\tilde{x}_{k+1}$ at the start of the next step $k + 1$ [24]. A fixed point $\tilde{x}^*$ is a point in the reduced state space (Poincaré section) that satisfies $\tilde{x}^* = S(\tilde{x}^*)$. The gait limit cycle crosses the Poincaré section in a fixed point.

Stability of the limit cycle is determined by calculating the eigenvalues of the Jacobian

$$J = \frac{\partial S}{\partial \tilde{x}}\Big|_{\tilde{x}^*}$$

In this method, a small perturbation is applied to the fixed point to evaluate the system response. If the state of the system converges to the fixed point, it means that the error caused by the perturbation shrinks and the limit cycle is stable. In this study, the Jacobian of the stride function around its fixed-point is numerically calculated for some slope angles. Table 2.1 shows the calculated eigenvalues for state space $[\theta\ \dot{\theta}]^T$. Results are calculated using backward differentiation numerical method, with absolute and relative tolerance of 10^{-10}. The passive walker over slope can show a period-p behavior. The system behavior is called period-one if any two consecutive steps are indistinguishable, that is, all the spatiotemporal variables exactly repeat themselves in each step [16]. For the modeled passive walker in this Chapter, the period-one gait is observed for the slope angles $0 < \gamma < 0.0157$ rad. For steeper slopes, higher-period gaits are recognized. This result is comparable with results obtained by other researchers [19]. The calculation of eigenvalues was done for a range of slope angles $0 < \gamma < 0.022$ rad and it shows that there is a stable limit cycle for this range that contains both period-one ($0 < \gamma < 0.0157$ rad) and period-two ($0.0157 < \gamma < 0.022$ rad) gaits.

Table 2.1: Eigenvalues for a planar passive walker over several slope angles.

Slope angle (rad)	Eigenvalues of state space: $[\theta\ \dot{\theta}]^T$
γ=0.007	[-0.2856 -0.0005]
γ=0.009	[-0.3147 -0.0007]
γ=0.012	[-0.3623 -0.0008]
γ=0.018	[-0.5177 -0.0007]

Robustness

Disturbances are always present in all environments, so the robustness of the system has a significant importance. For a walking robot, a rough terrain is an example of the cause of disturbances that can disturb the positions and velocities of the system. A passive walker is also very sensitive to the changes in its initial conditions.

The definition of stability for a passive dynamic walker is based on the criterion of converging to a limit cycle. Contrary, the definition of the robustness for this system can be related to the area around the stable limit cycle that contains the converging trajectories towards it. By definition, the basin of attraction (BOA) of a fixed point on the limit cycle is the intersection of the system Poincaré section with the vicinity around the limit cycle which contains all of the converging trajectories towards it [14].

The BOA contains all possible (reduced) system states $\tilde{x} = [\theta\ \dot{\theta}]^T$ at the start of each step with which, if the walker starts to walk, its trajectory will asymptotically converge to the limit cycle, *i.e.*,

$$BOA = \left\{ \tilde{x} \in \mathbb{R}^2 \mid \lim_{k\to\infty} S^k(\tilde{x}) = \tilde{x}^* \right\}$$

Fig. 2.8 shows the basin of attraction of the passive walker over the slope angles of $\gamma = 0.007$ rad and $\gamma = 0.012$ rad. The plots show the range of the variations in the state

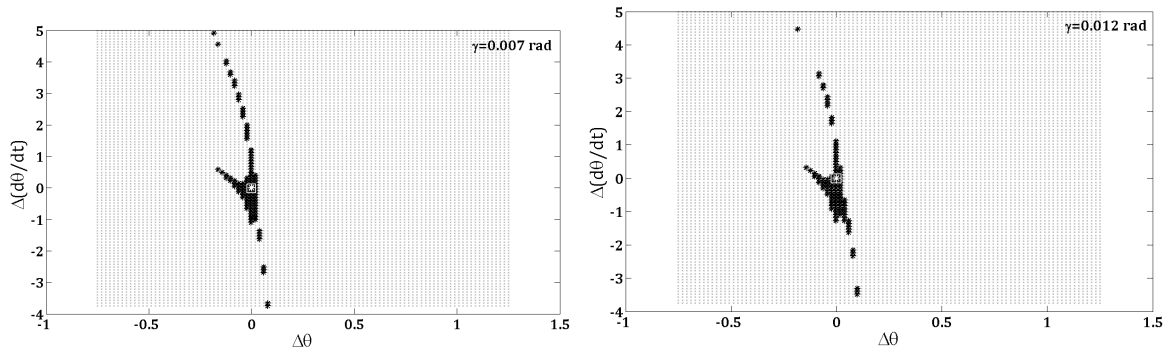

Figure 2.8: BOA of passive dynamic walker over slope angles 0.007 rad (upper plot) and 0.012 rad (lower plot). The x-axis shows deviation from θ^* and y-axis represents deviation from $\dot{\theta}^*$. The small dots show the unsuccessful initial conditions (their trajectories diverge from the stable limit cycle) and the stars show the successful initial conditions. The fixed points are marked by a star inside a rectangle.

$\Delta\tilde{x} = (\Delta\theta,\ \Delta\dot{\theta})$ around the fixed point $\tilde{x}^*$. The plots are numerically calculated by perturbing the initial condition of the model and, by forward simulation, checking if the walker could manage to walk at least 50 steps. The small dots show the variations for which the related trajectories diverge from the stable limit cycle; the stars show the variations for which the related trajectories converge towards the stable limit cycle. The fixed points are marked by a star inside a rectangle. To compare the area, shape and distribution of the deviations from the fixed point for different BOAs, the values are scaled by nominal values of $\theta = 0.4$ and $\dot{\theta} = 0.8$.

Obtaining the plot of the BOA for a passive walker requires an enormous amount of time-consuming computations. Moreover, comparing two basins of attraction in order to see which walker is more robust is not easy, since the basin of attraction of the passive walker is very narrow and also it does not have a simple symmetric shape. Measures like the area of the BOA or the distance from the fixed point to the boundaries of the BOA are not appropriate enough [14]. The distances from the fixed point to the boundaries of the BOA are different in various directions, and as a result it is difficult to define one measure based on the BOA. For instance, if we define *the biggest radius form the fixed point* as the measure of robustness, we should specify the direction in which the radius should be measured. Therefore, we should be more detailed in our criterion, *i.e.*, the biggest radius in a specific direction. In this case, calculation of the whole BOA is not required, since the specific criterion can be measured independently. Although the BOA contains all possible converging trajectories to the system limit cycle, some of these trajectories are more probable to happen in reality. For instance, the measure can be defined as *the largest applied disturbance with which the walker motion will still converge to its stable limit cycle*.

In this Chapter, we choose the step-down as a measure of robustness, since one of the probable disturbances is the change in the level of the surface. The measure is the largest step-down size (difference between levels of ground) that the robot can handle and converge to its stable walking pattern. This measure is practical and it has a good relevancy to the reality. Moreover, its related calculation is much less time-consuming than the BOA. Fig. 2.9 shows the step-down experiment for the passive walker over different slope angles. The step-down size was given some discrete values. As can be seen from the plot, for angles larger than 0.012 rad, which mainly represents the period-two gait, the

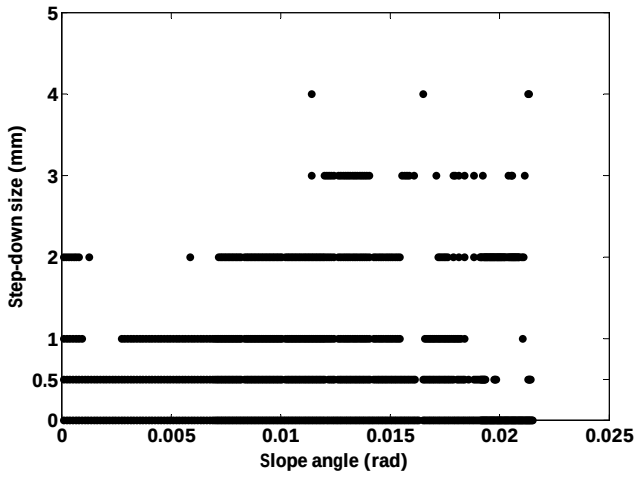

Figure 2.9: Step-down experiment for planar passive walker over range of slope angles. The experiment was done by applying some discrete values as the step-down level for a range of slope angles between [0–0.022 rad]. The dots indicate that the walker walking over the given slope managed to handle a step-down of the given height without falling down. For a range of slope angles, the steeper slope results in a bigger allowable step-down size.

robot may handle bigger step-downs, but they may not manage small step-downs. The step down results show an improvement in the robustness of the system by increasing the slope angles in the range of $0 < \gamma < 0.012$ rad. The system in this range of slope angles shows a period-one gait.

Dissipated energy, velocity and robustness

Using the compliant contact model of the ground, we can calculate the amount of dissipated energy due to the impact of the foot with the ground at each step by

$$\Delta H = \int_{t_b}^{t_e} F_n v \, \mathrm{d}t,$$

where t_b and t_e are the time before and after the collision, F_n is the normal force acting on the foot and v is the vertical velocity of the foot. Fig. 2.10 shows the plot of total (kinetic plus potential) energy H of the system for slope angle 0.012 rad for ten consecutive steps. At the end of each step, H is decreased by the impact energy loss ΔH. During a step, H is almost constant; some fluctuations can be seen due to the ground compliant contact model. By increasing the slope angle, the velocity will increase and more energy will be dissipated. Fig. 2.11 shows the trend of changes of velocity, robustness and dissipated energy over a range of slope angles. A steeper slope implies more dissipated energy, higher velocity and more robustness.

2.2.3 The Planar Passive Bipedal Walker with Compliant Legs

In this Section, we discuss the idea of applying compliancy to the robot legs. In particular, the model presented in Sec. 2.2.1 is modified such that a passive storage element (a

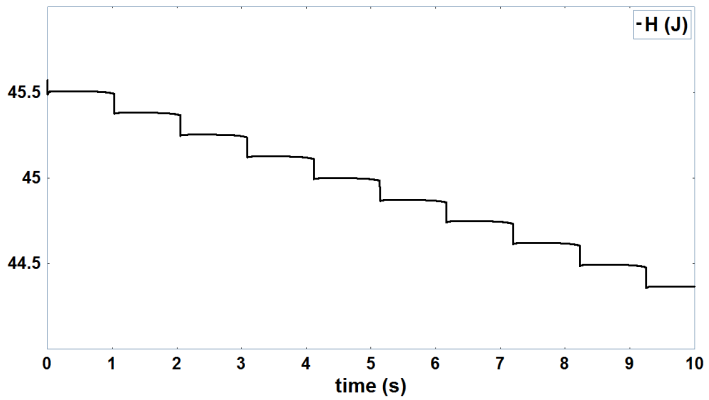

Figure 2.10: The plot of total energy of the system (H) over the slope angle 0.0012 rad for ten walking steps. At the end of each step, H is decreased as a result of impact of the foot with the ground. During a step, H is almost constant.

spring) is placed along the robot legs, as shown in Fig. 2.12. The reason behind adding springs along the legs is to absorb impact energy in order to increase robustness. In addition, part of the absorbed energy can be reused to sustain the gait.

Compliant leg parameters

As shown in Fig. 2.12, a linear spring, with constant stiffness k (in [N/m]), connects the end side of the leg to the center of mass of the foot. The motion is constrained to the movement along the leg. We introduce the (dimensionless) *scaled stiffness* K of the leg to be

$$K = kL/(M+m)g.$$

In order to make the system behave well, a damper with damping D (in [Ns/m]) is added parallel to each spring. While the leg is in the swing phase, the effective mass is the foot mass m and during the stance phase the effective mass is the sum of the hip mass and the swing foot mass, *i.e.*, $M+m$, resulting in the relative damping ζ_{st} during stance phase and ζ_{sw} during swing phase:

$$\zeta_{st} = \frac{D}{2\sqrt{(M+m)k}} \text{ and } \zeta_{sw} = \frac{D}{2\sqrt{mk}}. \tag{2.5}$$

By adding the damping in parallel to the spring, a portion of the impact energy will be dissipated, and hence cannot be used to sustain the gait. However, the realized desired behavior of this configuration is:

- to have an under-damped system to absorb the impact force, store its energy during the stance phase and return as much of it as possible to the system at the moment that the foot leaves the ground ($\zeta_{st} < 1$), in order to sustain the gait;
- to have a bounce-less swing phase that makes it possible for the swing foot to properly find the ground contact point to land ($\zeta_{sw} > 0.7$, according to our simulation experiments a moderately-damped condition is sufficient).

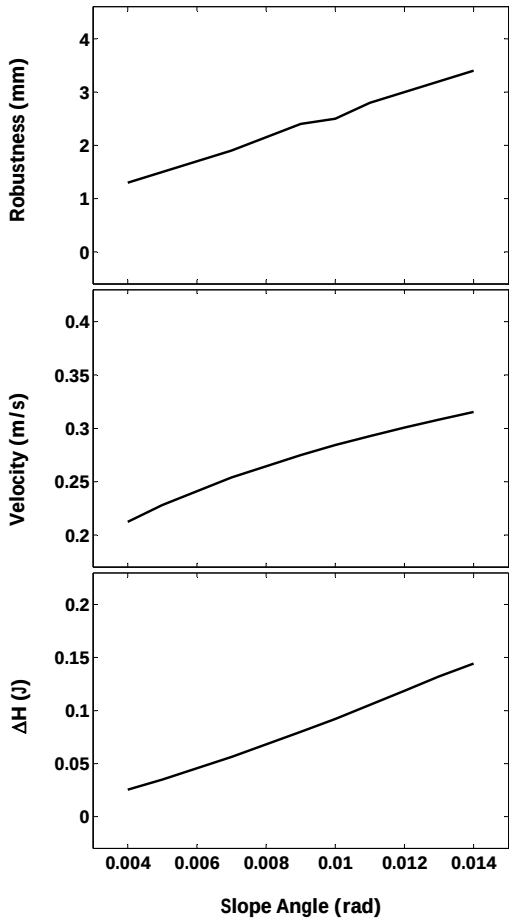

Figure 2.11: Plot of robustness, velocity and dissipated energy per step (ΔH), velocity over a range of slope angles [0.004–0.0014 rad]. The measure of robustness is step-down experiment. By increasing the slope angle, the trend of changes for these three parameters is the same. The more dissipated energy, the more velocity and robustness.

With the described mass configuration ($M = 3$ kg, $m = 0.1$ kg), a single damping parameter D can be chosen such that the criteria for both ζ_{st} and ζ_{sw} are satisfied. From (2.5), it can be deduced that $\zeta_{st} = \sqrt{\frac{m}{M+m}}\zeta_{sw} \approx 0.18\ \zeta_{sw}$. Therefore, in order to keep the swing phase at least moderately-damped ($\zeta_{sw} > 0.7$) and the stance phase under-damped, we must restrict the damping ratio to $0.13 < \zeta_{st} < 1$.

The exact choice of ζ_{st} is important since it appears to affect the range of stiffness with which robot can walk stably (we refer to this range as *stable stiffness range*). Also, it has an effect on the robustness of the system.

Fig. 2.13 shows the plot of the system behavior over the choice of ζ_{st} for the chosen mass/length configuration. Again the step-down experiment is the measure of the system robustness.

- $\zeta_{st} < 0.13$: note that we violate the damping criteria here; indeed it appears that having an under-damped compliancy during swing phase is not good for the robustness. The stable stiffness range is limited; it is not possible to find a stable gait for low values of stiffness. Moreover, if a stable gait can be found for small stiffness, the step down experience shows poor robustness. For high stiffness, a *chaotic robustness* is

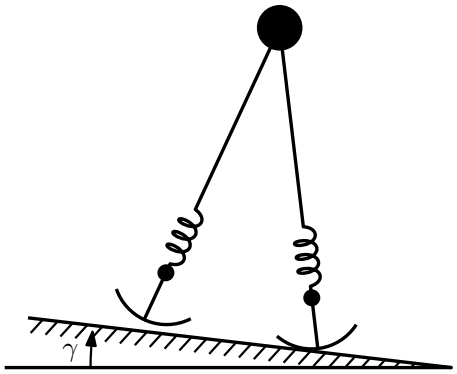

Figure 2.12: An impression of the configuration of the passive walker with compliant legs. A spring with stiffness k is placed along each leg to increase energy efficiency of the gait.

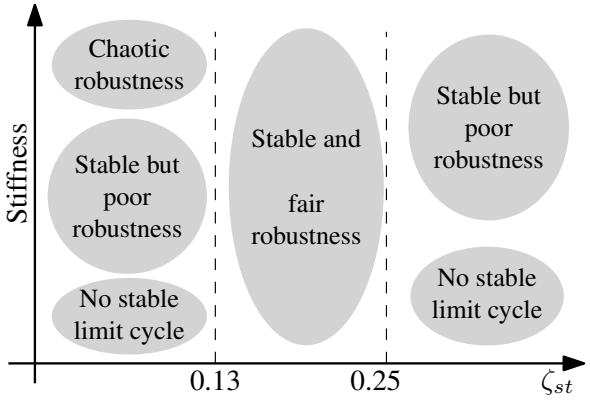

Figure 2.13: This plot shows the dependency of the system behavior to the choice of ζ_{st} and spring stiffness. The choice of ζ_{st} affect the stable stiffness range of the compliant legs as well as robustness of the system.

resulted. Chaotic robustness refers to random behavior of the system, for example it can handle a step-down size of 3.5 mm but it fails a step-down size of 1 mm.

- $0.13 < \zeta_{st} < 0.25$: the system shows the best robustness comparing to other values of ζ_{st}. This area is pointed out by the expression *fair robustness* that refers to the ability of the system to handle the step-down in a continuous range and up to a maximum value that is comparable with the results of the system with rigid legs.

- $\zeta_{st} > 0.25$: the third area of the plot shows the system behavior for larger values of ζ_{st}. In this region, again the stable stiffness range is limited. Although the system does not show a chaotic behavior, it shows a comparably poor robustness.

Simulation and results

In this Section, we discuss the simulation results of the passive dynamic walker with compliant legs and make a comparison with rigid leg walkers.

When comparing performance of two walking machines, the three properties, robustness, the required energy (energy efficiency) and velocity should be considered. To make a fair comparison between the performances of two walkers, we can fix a value for one of these

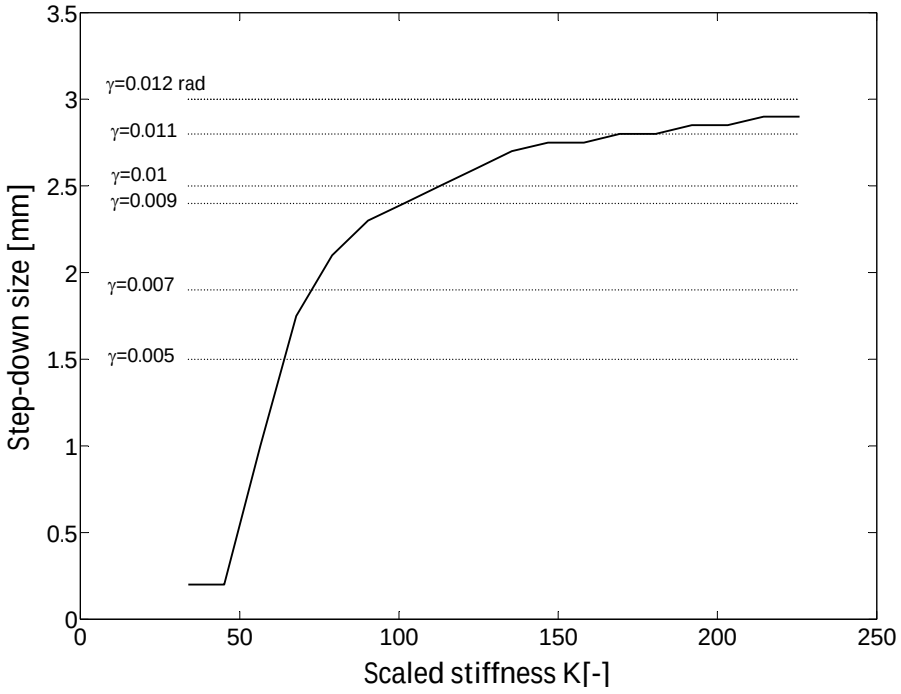

Figure 2.14: Robustness of two passive walkers: compliant legs and rigid legs. The compliant-leg robot walks over a slope angle of 0.009 rad. The horizontal lines show the maximum step-down size that a passive walker with rigid legs can handle for different slope angles.

parameters and compare the two other parameters. For example, we may choose one rigid and one compliant walker walking at the same velocity (but on a different slope) and compare their robustness and energy efficiency.

In our simulations of compliant walkers, we kept the slope angle fixed at $\gamma = 0.009$ rad. The damping ratio (ζ_{st}) for the experiments of this section is 0.15.

Fig. 2.14 shows the result of the analysis of the robustness of the two passive walkers: one with compliant legs and the other with rigid legs. The robot with compliant legs walks over a fixed slope angle of 0.009 rad and its robustness is reported over a range of stiffness. The robot with rigid legs walks over several slope angles. K is changed from 34 to 226, and the plot indicates an improvement of robustness as the stiffness of the legs increases. For stiffnesses smaller than 34 either there is no stable gait or the robustness is very poor. The horizontal lines show the maximum step-down size that a passive walker with rigid legs can handle for different slope angles.

It should be noted that all of these angles and the values of stiffness share the same property: the system shows a period-one behavior and it continuously can handle the step-down experience up to a maximum value. It can be seen that the robustness of the passive walker with compliant legs for stiffness larger than 102 is bigger than the robustness of the same passive walker with rigid legs over the same slope angle (0.009 rad).

By applying a stiff enough spring along the leg (for low stiffness spring the stored energy will be mainly dissipated by the oscillation of the spring), the stored energy during the stance phase will increase the velocity of the motion. According to the numerical results obtained by simulation:

- The velocity of the passive walker with compliant legs for stiffness larger than 68 is

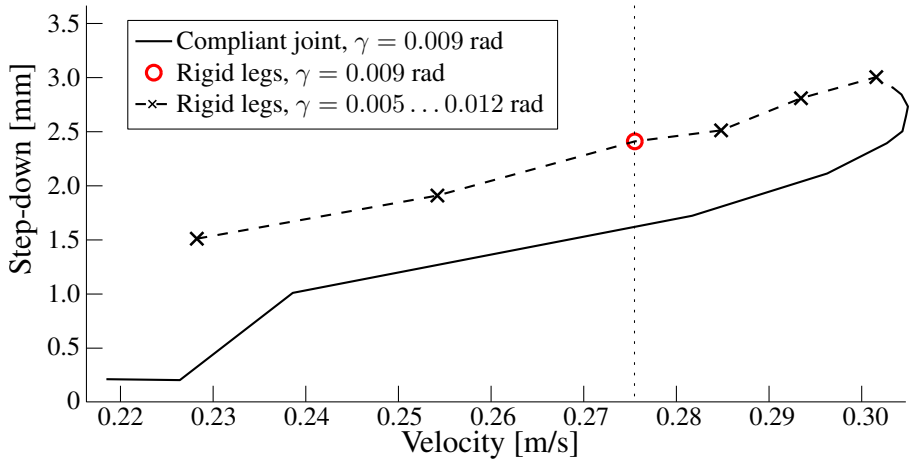

Figure 2.15: Robustness over the velocity. The dashed line shows the plot of robustness over velocity for rigid leg walker over different slope angles in the range of 0.005 rad to 0.012 rad (the slope angle 0.009 rad is marked by a circle on the plot). The continuous line shows the plot of robustness over velocity for the compliant leg walker over the fixed slope angle of 0.009 rad with different stiffness in the range 34 to 226.

bigger than the same passive walker with rigid legs over the same slope angle (0.009 rad).

- The amount of dissipated energy, due to impact of the foot with the ground, of the passive walker with compliant legs is about 12 times smaller than the dissipated energy of the same passive walker over the same slope angle (0.009 rad). It means that applying the stiffness is successful to prevent loss of energy and improve the energy efficiency of the system.

Fig. 2.15 shows the plot of the robustness over the velocity for two cases: the dashed line is related to the rigid leg walker over different slope angles in the range of 0.005 rad to 0.012 rad (the slope angle 0.009 rad is marked by a circle on the plot); the continuous line is related to the compliant leg walker over the fixed slope angle of 0.009 rad with different stiffness in the range 34 to 226.

From Fig. 2.15, the following conclusions can be derived:

- For a certain velocity, the robustness of the passive walker with rigid legs is bigger than the robustness of the passive walker with compliant legs. This difference will be smaller by increasing the leg stiffness.

- By varying the stiffness of the robot legs walking over a fixed slope angle, the velocities of a range of slope angles (smaller and bigger than the fixed slope angle) can be obtained.

- For a proper choice of leg stiffness (*e.g.*, 180) over the slope angle 0.009 rad, the velocity of the slope angle 0.012 rad is obtained, also their robustness is almost the same (it is 9% smaller than the robustness of the slope angle 0.012 rad). It should be noticed that the amount of injected energy for slope angle 0.009 rad is smaller than 0.012 rad. So, the gait properties of a larger slope angle are obtained by applying a passive storage element along the walker legs.

In summary, it is concluded that adding compliance along the legs of a compass walker can indeed increase the robustness of the gait. In particular, if the compliance is variable, robustness can be maintained over different slope angles. It is observed that the stiffness of the legs should be relatively large. Although this results in dynamics that approach the dynamics of a rigid legged walker, the small compliance in fact absorbs sufficient impact energy to reject disturbances, while at the same time the passive gait can be maintained.

In addition, if the stiffness is varied appropriately, different walking gaits can be obtained, corresponding to behaviors exhibited by passive rigid walkers on various slopes. In particular, the forward velocity can, to some extent, be controlled by variation of the leg stiffness.

2.3 Hexapod walking with compliant legs

The use of legs for locomotion through rough terrain promises superior performance in comparison to wheeled vehicles. Nevertheless, most of today's legged machines lack a thorough design that incorporates elastic elements in order to achieve the elastic behavior that is observed in animal running. To build a robot which is able to walk and run smoothly, even on rough terrain, new biologically inspired leg concepts need to be developed. These new legs should have the capability to absorb impacts, to store elastic energy, and to change their stiffness in order to achieve a desired gait. At the same time, the legs need to allow a dexterous foot placement that is required in running.

Exploiting the benefits of passive compliance directs the research concerning the implementation of elastic systems to replace motors and gears within distinct joints. This will be a step towards a deeper understanding of elastic multi-legged robots and should guide further experimental and analytical research.

Motivated by the question of how robots can take advantage of passive elastic elements, this work explores if considerable mechanical compliance contributes significantly to the stability and the robustness of multi-legged robotic running. In particular, one of the research goals is to show by simulation studies that an appropriately designed self-stabilizing structure could ease the control and improve the performance of running robots. This work explores if considerable mechanical compliance contributes significantly to the stability and the robustness of multi-legged robotic running. For this purpose, three passive elastic leg concepts with increasing complexity have been developed and simulated.

2.3.1 Challenges

The purpose of this study is to gain knowledge of how to combine actuated and passive, elastic joints within a leg, such that it enables a hexapedal robot to run stably, within a broad range of forward velocities. Furthermore, it is important to analyze the behavior from a energetic point of view, by investigating the possibility of energy recovery during each step. In fact, from literature it is known that insects, mammals and humans are able to store a certain amount of kinetic energy as elastic or potential energy and release it, triggering a complex and continuous exchange of power. Since this phenomenon increases the efficiency of the gait, the use of springs in the joints potentially makes the hexapod robot more energy efficient.

Parallel to the springs, dampers are important in achieving a robust and stable running behavior. Since this study puts one focus on energy recovery, damping factors are chosen low enough to keep losses at a low level, and high enough to provide stability.

With these aims, three leg concepts are presented. For each of the leg concepts, hexapod robots are modeled and simulated with different total leg stiffness settings and a variety of forward velocities. In this way, the relation between stiffness and velocity, and in particular their influence on the energy efficiency, is investigated.

2.3.2 Leg concepts

This work considers three different leg types. In particular, the first design is inspired by the simplification of the 3D spring-loaded inverted pendulum (SLIP). The second design is closer to the biomechanical insect leg design, and the third model captures characteristics from both the first and second designs. For each concept, simplifications have been considered in order to obtain a structure that, while preserving the main features of the ideal model, can easily be controlled with only two actuated degrees of freedom.

The main features of the legs are passive compliant elements that allow the leg to absorb energy during one phase of a step and to release it during a next phase. The second important aspect of the compliance elements is to reduce the impact forces for the main body of the robot during leg touchdown. In order to have a light leg and to reduce the number of motors, only the hip joint of each leg has two actuated degrees of freedom.

Running at high velocity means high velocity of the limbs, and this results in high ground impact forces. If the intensity of these vibrations is excessive, it can damage gears and motors. To protect the hip actuators, a decoupler was inserted between the leg and the hip. Those elements were realized using a planar joint controlled by springs and dampers.

The contact between the foot and the ground is modeled as a point contact with friction. The normal force is calculated using a unilateral spring-damper system, while the tangential force is calculated using Coulomb friction.

Concept 1

This leg model is the most simple, because the leg is composed of only two segments. The segments are connected with a prismatic joint, which is controlled by a passive spring-damper system. The goal is to achieve gaits that exploit the SLIP model in a 3D configuration, embodying a richer behavior than the planar model. This concept is shown in Figure 2.16.

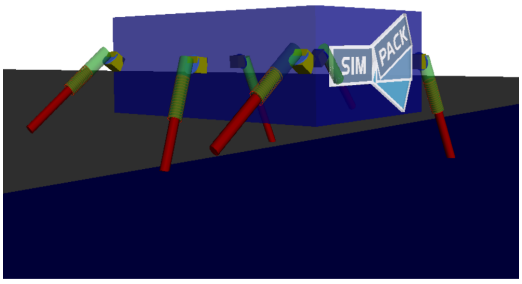

Figure 2.16: Conceptual design 1.

Concept 2

This leg concept design, depicted in Figure 2.17, is related to the biomechanical design of insect legs. The main aspect of insect legs is their adaptability to different terrains, and the possibility to run using a fast and simple gait. These features make the insect leg interesting to be used as a template to develop a structure able to satisfy the requirements for a running hexapod machine.

Between femur and coxa, a passive rotational joint with only one degree of freedom is implemented. Tibia and femur are connected with another passive rotational joint with two degrees of freedom. The second degree of freedom is intended to better damp impacts of the foot with obstacles on rough terrain. The “foot” link is a linear joint that tries to emulate the behavior of the tarsal insect segments.

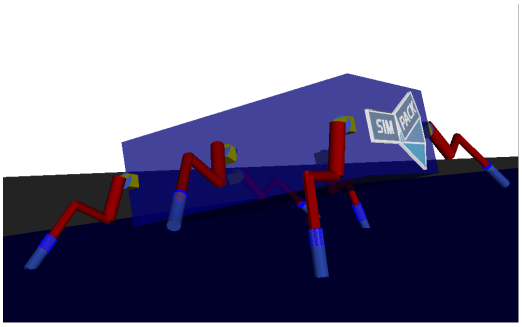

Figure 2.17: Conceptual design 2.

Concept 3

This concept, shown in Figure 2.18, combines aspects of the previous two concepts. In fact, it is more complex than the first concept, but is a simplification of the second. There are again only two sections in each leg, but in this case connected with a rotational joint.

Additionally, two linear springs were added. The “foot” is connected to the leg with a linear spring in order to absorb ground impacts. The lower segment is connected to the upper segment with a rotational joint, and the upper spring stabilizes the body against lateral disturbances. The knee rotational joint gives the leg a forward-backward degree of freedom to damp foot collisions during the step.

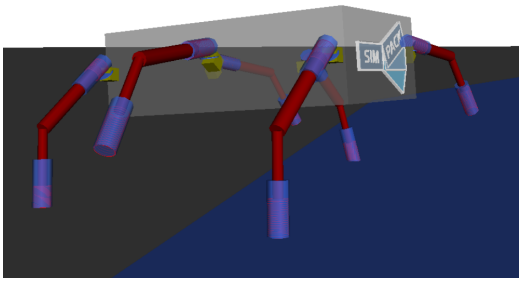

Figure 2.18: Conceptual design 3.

2.3.3 Simulation results

All simulations are performed as a co-simulation employing Simpack for the multi-body dynamics and SIMULINK realizing the control of the hexapods by simple Central Pattern Generators (CPG). The mass of the robots is 3 kg, and the main part of the mass is contributed by the main body, assuming that it incorporates all motors.

Using the simulation data, different energetic phenomena, like phase relations, energy recovery, specific resistance and energy consumption per step, can be analyzed for each of the design concepts. Only the first two concepts are considered, because the third concept experienced unexpected internal oscillations due to some poor design decisions.

For the first two concepts, the joint stiffness has been varied from very soft to almost rigid settings at different velocities, while the joint damping has been fixed at low values. Nevertheless, the damping effects need to be studied in more detail in future work. For both concepts, stable running at velocities above 2 m/s was achieved using an open-loop tripod gait, as presented in Figure 2.19 and Figure 2.20. The stronger biologically motivated concept achieved even higher speeds of up to 3 m/s at the same tripod excitation frequency compared to the first concept.

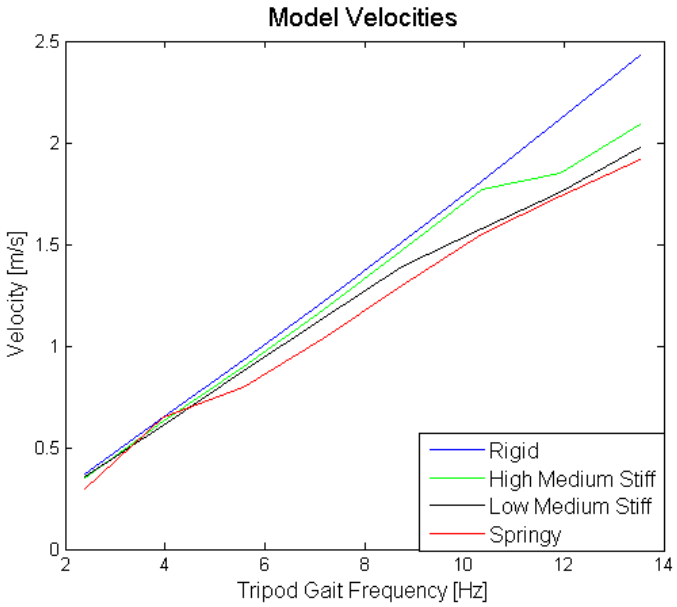

Figure 2.19: Achievable forward velocities for the first design.

The energy consumption for the two designs is shown in Figure 2.21 and Figure 2.22, respectively. The energy consumed at each tripod stance phase is higher for the second concept, which is attributed to its higher number of joints and thus higher number of damping elements. Both concepts are more efficient at higher joint stiffness settings, which is most likely a result of limited joint motions and thus limited energy dissipation by the joint dampers. At high velocities and high joint stiffness settings, the second concept experiences large energy dissipation, which is a hint that the system is not well tuned and only a small amount of energy is stored and recovered. For both concepts the amount of recovered energy decreased at higher speeds for all stiffness settings and the specific resistance was within a range of 1 to 4.

The models of both concepts showed, for each stiffness setting, velocity ranges that

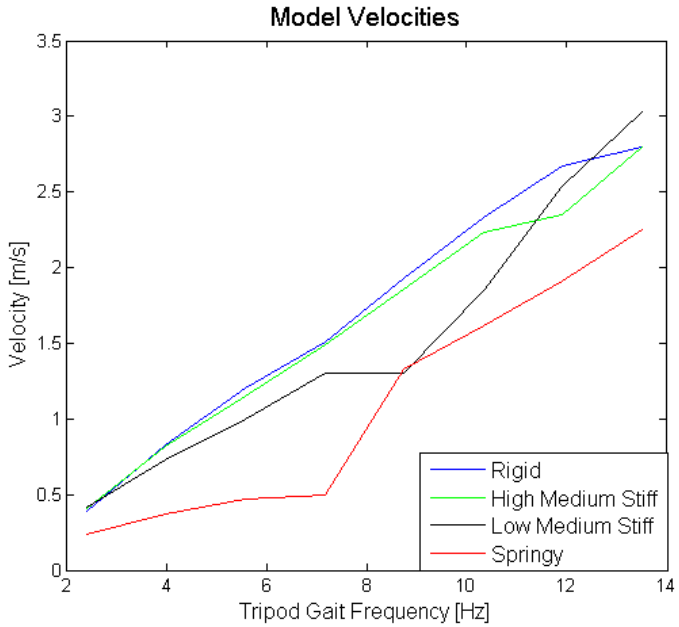

Figure 2.20: Achievable forward velocities for the second design.

resulted in smooth running with a slightly upward pitched nose, while leaving these ranges leads to more shaky motions. This is a clear hint that variable joint stiffness actuators will result in a broader range of smooth gaits.

2.3.4 Conclusions

This simulation study just provides an intuitive insight into the effects of the use of passively compliant joints in hexapedal locomotion and supports the general feasibility of such a robot. In future work, the impact of the kinematic configuration and the contribution of each compliant joint on the overall behavior has to be analyzed in more detail. Furthermore, a meaningful measure has to be defined that allows to evaluate the robustness, stability and efficiency of a design. Additionally, control algorithms have to be developed that exploit the mechanics to generate the required oscillatory motions for locomotion.

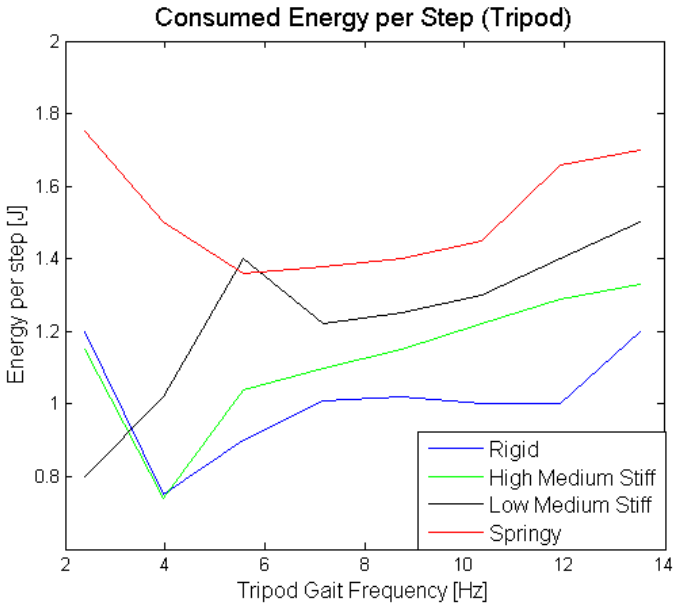

Figure 2.21: Energy consumption of the first design.

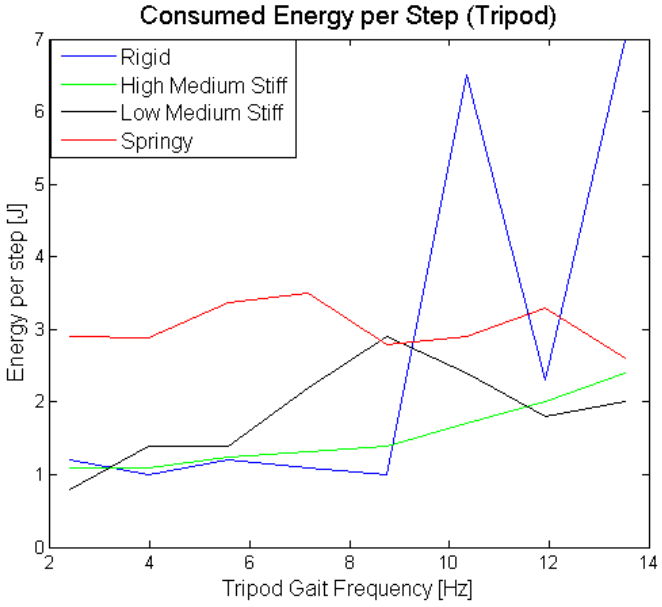

Figure 2.22: Energy consumption of the second design.

Chapter 3

Port-based Modeling of Variable Stiffness Actuators

In this Chapter, we present a generic, port based model for variable stiffness actuators, with which a wide variety of actuator designs can be modeled. We use a port-based approach, because this framework captures perfectly the energy flows between the actuator, the controller, and the load. Then, using this framework, we show how energy efficient control of robotic systems can be achieved. In particular, we show that, if the actuator design has certain properties, disturbance energy can be stored and effectively reused for actuation.

This approach is especially relevant for locomotion systems. As was shown in the preceding Sections, locomotion systems can benefit from the use of variable stiffness actuators, both in terms of robustness and energy efficiency. Using the port-based approach gives important insights in the energy flows, and thus a generic, port-based model of variable stiffness actuators will aid in the analysis and application of such actuators when it comes to energy efficiency.

3.1 Motivation

In this Chapter, we consider a class of variable stiffness actuators that have internally a number of elastic elements, usually springs, and a number of actuated degrees of freedom. It is this mechanical characteristic that allows to change the apparent output stiffness of the actuator independently from its output position. The apparent output stiffness K is defined as the ratio of the infinitesimal change of the actuator output force δF as a result of an infinitesimal displacement of the actuator output position δr, i.e.,

$$K := \frac{\delta F}{\delta r} \tag{3.1}$$

If we consider a variable stiffness actuator as a collection of elastic elements and ideal actuated degrees of freedom, i.e., the degrees of freedom are without mass and without friction, then the electrical energy supplied to the internal actuators can either be used to do work at the actuator output, or it can be internally stored in the elastic elements. For example, the energy is stored when the internal degrees of freedom are used to change the pretension of internal springs to achieve a different apparent output stiffness. However, in this case, the energy is irreversibly stored, in the sense that it cannot be used to do work at

the output. This means that changing the apparent output stiffness has a negative impact on the energy efficiency of the actuator, as already observed in [25].

In robotic applications in which energy efficiency is of particular concern, all power supplied to a variable stiffness actuator should be used only to do work at the actuator output, and not to change the apparent output stiffness. Following this argument, by *energy efficient variable stiffness actuators*, we mean actuators for which the apparent output stiffness can be changed without injecting or extracting energy to and from the internal elastic elements.

The aim of this Chapter is to find which properties variable stiffness actuators must satisfy to be energy efficient. To facilitate this search, a port-based model is used, since it perfectly captures the energy flows between the internal degrees of freedom, the internal elastic elements, and the actuator output. The required kinematic properties of energy efficient variable stiffness actuators are derived from the analysis of the port-based model, which allowed for the introduction of a conceptual design of a novel working principle and for the realization of a prototype.

3.2 Port-based Modeling Framework

In this Section, we intend to briefly introduce the port-based modeling framework, with the aim of providing more insights in the energy flows in variable stiffness actuators. For a more comprehensive treatment of port-based modeling and bond graphs, the reader is referred to e.g. [26, 27].

3.2.1 Port-based Modeling

Any physical system can be modeled in a port-based framework. A key element in this modeling framework is the concept of power conjugate variables, called *efforts* and *flows*. In the mechanical domain, flows are physically interpreted as velocities and efforts as forces. The dual product $\langle e|f\rangle$ of an effort e and a flow f yields power. A pair of effort and flow variables thus defines a power flow.

If f is an element of a real vector space $\mathcal{V}$, and e is an element of the dual vector space $\mathcal{V}^*$, then we can define a subspace $\mathcal{D} \subset \mathcal{V} \times \mathcal{V}^*$, called *Dirac structure*, such that

$$\langle e|f\rangle = 0, \quad \forall\,(f,e) \in \mathcal{D} \tag{3.2}$$

A Dirac structure defines a network topology, i.e., a distribution of power flows among the ports of the structure, and from (3.2) it follows that a Dirac structure is power continuous. Note that a Dirac structure is allowed to vary in time, as long as the power continuity is preserved.

Using a Dirac structure, we can model the behavior of the system by making explicit its network topology. The generic network topology is shown in Figure 3.1, where four separate power ports can be distinguished. The *interaction port* is available for interaction with the environment, i.e., (a composition of) other systems. The associated port variables are denoted by the pair (f_I, e_I). The *control port* is used for control action, with associated port variables (f_C, e_C). The port variables of the *storage port* are denoted by the pair (f_S, e_S) and are associated with the internal energy storage of the system, represented by a

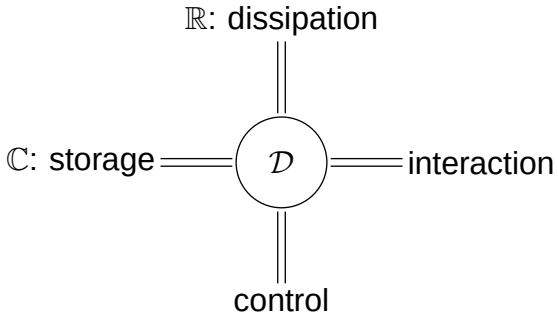

Figure 3.1: Network structure of a generic physical system - The Dirac structure $\mathcal{D}$ defines a power continuous connection between the ports. Internal energy storage is represented by the $\mathbb{C}$-element, and energy dissipation by the $\mathbb{R}$-element. The system interacts with the environment via the control port and the interaction port.

Hamiltonian energy function H. At this port, the power conjugate variables satisfy the energy balance

$$\frac{\mathrm{d}H}{\mathrm{d}t} = \langle e_S | f_S \rangle \tag{3.3}$$

Energy is dissipated via the *dissipation port*, with associated port variables (f_R, e_R) satisfying

$$\langle e_R | f_R \rangle \leq 0 \tag{3.4}$$

Often, a linear model of the dissipative element is used, and then the port variables are related as

$$f_R = -R e_R \tag{3.5}$$

with a positive semi-definite matrix $R = R^T \geq 0$.

The Dirac structure $\mathcal{D}$ defines the power continuous port interconnection. From the definition of a Dirac structure (3.2), it follows that

$$\langle e_S | f_S \rangle + \langle e_R | f_R \rangle + \langle e_I | f_I \rangle + \langle e_C | f_C \rangle = 0$$

Substituting (3.3), we have

$$\frac{\mathrm{d}H}{\mathrm{d}t} = -\langle e_R | f_R \rangle - \langle e_I | f_I \rangle - \langle e_C | f_C \rangle \tag{3.6}$$

i.e., the rate of change of the internal energy is determined by the amount of energy dissipated, and the power flow through the control and the interaction ports. It follows that the system is passive with respect to the input ports, i.e., the control port and the interaction port.

3.2.2 Input/Output Representation of Port-Hamiltonian Systems

The Dirac structure representation of a system, as given in the previous Section, does not consider causality. This representation is close to the physical reality, since causality is an artificial concept. However, often it is more convenient to consider a causal representation of the system dynamics, with respect to the *input port*, i.e., the composition of the interaction port and the control port. Therefore, we define the system state manifold $\mathcal{X}$, with

coordinates x, and assume that it is a Poisson manifold and satisfies the integrability conditions [27]. Under these conditions, we can derive the input/output representation of the port-Hamiltonian system.

The Hamiltonian energy function $H : \mathcal{X} \to \mathbb{R}$ is defined as a smooth function on the state manifold $\mathcal{X}$. In addition, we consider the port interaction space W_x, which is a vector bundle over $\mathcal{X}$. The power conjugate variables (u, y) of the input port then belong to $W_x \times W_x^*$. Let ϕ_x denote a linear map from W_x to $T_x\mathcal{X}$ and ϕ_x^* its dual, and let $\mathcal{J}_x$ denote a Poisson tensorfield, which defines a fibre bundle morphism from $T_x^*\mathcal{X}$ to $T_x\mathcal{X}$. The port-Hamiltonian system can then be represented as

$$\begin{aligned} \dot{x} &= \mathcal{J}_x \, \mathrm{d}H(x) + \phi_x \, u \\ y &= \phi_x^* \, \mathrm{d}H(x) \end{aligned} \tag{3.7}$$

where $\mathrm{d}H(x)$ denotes the differential of the Hamiltonian energy function $H(x)$. The coordinate function x is the state of the system, and the port variables u and y can be considered as inputs and outputs of the system, respectively.

If we choose local coordinates on $\mathcal{X}$, we can write (3.7) as

$$\begin{aligned} \dot{x} &= J(x)\frac{\partial H}{\partial x}(x) + g(x)u \\ y &= g^T(x)\frac{\partial H}{\partial x}(x) \end{aligned} \tag{3.8}$$

where the skew-symmetric matrix $J(x)$ represents the network topology between the ports, and thus represents the Dirac structure. In local coordinates, it is also more apparent how the dissipative element defined in (3.5) can be included into the system dynamics. Indeed, by letting the pair (u, y) only represent the ports by which the system interacts with other systems, i.e., the composition of the control port and the interaction port, the system dynamics are given by

$$\begin{aligned} \dot{x} &= \big(J(x) - R(x)\big)\frac{\partial H}{\partial x}(x) + g(x)u \\ y &= g^T(x)\frac{\partial H}{\partial x}(x) \end{aligned} \tag{3.9}$$

with $R(x) = R^T(x) \geq 0$ a positive semi-definite matrix.

3.2.3 Bond Graph Representation

The concept of power conjugate variables, and thus of power flows, lends itself for a compact graphical representation. In Figure 3.2, the interconnection of two port-Hamiltonian systems A and B is shown. The power flow between the two systems is represented by a *bond*, i.e., the half arrow. In particular, the power flow $\langle e|f \rangle$ is defined positive in the direction of the half arrow. In this example, the systems A and B can be port-Hamiltonian systems, as given in (3.9), or, on a more conceptual level, power continuous interconnection structures as defined in (3.2), energy storing elements as defined in (3.3) or energy dissipating elements as defined in (3.4).

Using the concept of bond graphs, we can graphically represent the concept of a port-Hamiltonian system of Figure 3.1, as shown in Figure 3.3, in which the multi-bonds

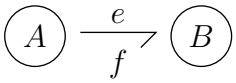

Figure 3.2: Interconnection of two port-Hamiltonian systems A and B - The power flow $\langle e|f\rangle$ is defined positive in the direction of the bond, i.e., the half arrow.

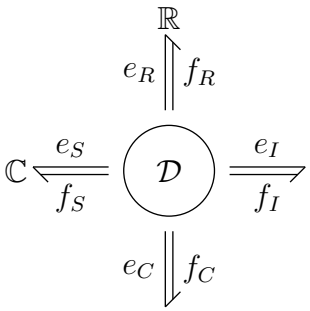

Figure 3.3: Bond graph representation of a port-Hamiltonian system - The $\mathcal{D}$ is the Dirac structure, the $\mathbb{C}$-element represents energy storage and the $\mathbb{R}$-element energy dissipation.

indicate a multidimensional interconnection. Note that in order to comply with the power continuity constraint (3.2), all bonds must have the same orientation with respect to the Dirac structure.

3.3 Variable Stiffness Actuators as port-Hamiltonian Systems

With the aim of getting more insights into the power flows between the variable stiffness actuator, the controller, and the actuator output, in this Section, we present a port based model of variable stiffness actuators. This model was first presented in [28], but we provide here an extension to include a load, and a more detailed analysis of its properties and behavior.

3.3.1 Variable Stiffness Port

To get a better understanding of variable stiffness actuators, we first model the concept of a *variable stiffness port*. In this concept, the behavior of a linear spring is modulated by an external variable, so that at the port the spring appears to have a variable stiffness.

The concept is shown, using bond graphs, in Figure 3.4. The $\mathbb{C}$-element represents a linear spring and, therefore, a storage of elastic energy. Let s denote the state of the spring, i.e., its elongation or compression, then the elastic energy is given by $H_s(s) = \frac{1}{2}ks^2$, where k is the elastic constant of the spring. The power conjugate variables are

$$f_S = \dot{s}, \quad e_S = \frac{\partial H_s}{\partial s}(s) \tag{3.10}$$

The interaction port is characterized by the power conjugate variables (f_I, e_I), corresponding to the rate of change of the actuator output position r and the generated output force F, i.e., $(\dot{r}, F)$. The storage element and the interaction port are connected by

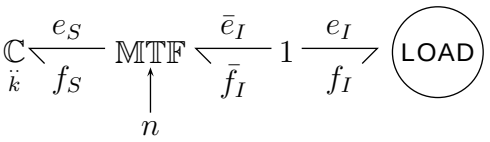

Figure 3.4: Model of a variable stiffness port - The external variable n modulates the transformer $\mathbb{MTF}$ and, therefore, determines how the linear spring, represented by the $\mathbb{C}$-element with elastic constant k, is sensed by the load.

means of a Dirac structure, realized by the combination of a $\mathbb{MTF}$-element, i.e., a modulated transformer, and a 1-junction, a common flow connection.

The behavior of the $\mathbb{MTF}$-element is described by the relations

$$\begin{aligned} f_S &= n\,\bar{f}_I \\ \bar{e}_I &= n\,e_S \end{aligned} \tag{3.11}$$

where $n \in \mathbb{R}^+$ is the modulation variable. The $\mathbb{MTF}$-element is power continuous, i.e., $\langle \bar{e}_I | \bar{f}_I \rangle = \langle e_S | f_S \rangle$. The behavior of the 1-junction is given by

$$\begin{aligned} \bar{f}_I &= f_I \quad (= \dot{r}) \\ \bar{e}_I &= -e_I \quad (= -F) \end{aligned} \tag{3.12}$$

Combining (3.10), (3.11) and (3.12), we can write

$$\begin{aligned} \dot{s} &= f_S = n\,f_I && (= n\,\dot{r}) \\ e_I &= -n\,e_S = -n\,\frac{\partial H_s}{\partial s} = -n\,k\,s && (= F) \end{aligned} \tag{3.13}$$

By considering infinitesimal changes in the actuator output force and position, from (3.13), we obtain that

$$\delta F = n^2 k\,\delta r$$

Using the definition of the stiffness given in (3.1), we obtain that the apparent output stiffness, as it is sensed by the load, is given by

$$K = n^2 k$$

It is observed that the apparent output stiffness is the constant stiffness of the spring, modulated by the external variable n. Thus, the output behavior can be modulated by changing n appropriately. Moreover, since n is an external variable and not a power variable, the output stiffness is changed in an energy free way, i.e., the energy stored in the spring is not changed due to modulation of n. It is this kind of behavior we wish to achieve with a variable stiffness actuator. However, it should be noted that, in this model, the maximum energy flow through the interaction port is limited by the initial energy present in the storage element. Therefore, in order to derive a model for an actuator with variable stiffness port behavior, a model with an additional power port is needed, so that additional energy can be supplied to do work on the load.

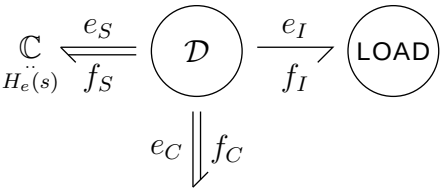

Figure 3.5: Generalized model of a variable stiffness actuator - The $\mathcal{D}$ is the Dirac structure, the internal elastic elements are represented by the multidimensional $\mathbb{C}$-element, described by the energy function $H_e(s)$. The internal degrees of freedom are actuated via the control port (f_C, e_C), while the interconnection with the load is via the output port (f_I, e_I).

3.3.2 Variable Stiffness Actuators

In deriving a generic model for variable stiffness actuators, without loss of generality, we consider that:

- the actuator has a number of internal elastic elements, described by state variables s and energy function $H_e(s)$, which describes the storage of elastic energy;
- internally, there are a number of actuated degrees of freedom, with configuration variables q;
- the stiffness K, sensed at the actuator output port, is determined by the intrinsic properties, the state of the elastic elements and by the configuration of the internal degrees of freedom.

Moreover, in our model, internal friction and inertia are neglected, since the focus of the analysis is on the working principles of variable stiffness actuators and not on the optimization of the implementation.

In Figure 3.5, a bond graph representation of a generic model of a variable stiffness actuator is shown. In comparison with the model shown in Figure 3.4, some differences can be observed. The $\mathbb{C}$-element is now multidimensional and its port behavior is characterized by power conjugate variables

$$f_S = \dot{s}, \quad e_S = \frac{\partial H_e}{\partial s}(s) \tag{3.14}$$

where $H_e(s)$ is the storage of the elastic energy due to the internal elastic elements. The $\mathbb{MTF}$-element and 1-junction have been replaced by a generic Dirac structure, which determines how the power is distributed between the $\mathbb{C}$-element, the *interaction* or *output port* (f_I, e_I), and the *control port* (f_C, e_C). In particular, the output port is characterized by two power conjugate variables, which correspond to $(\dot{r}, F)$, i.e., the rate of change of the actuator output position r and the force F that the actuator exerts on the load. The control port is characterized by two power conjugate variables, which correspond to $(\dot{q}, \tau)$, i.e., the rate of change of the configuration of the internal degrees of freedom q and the torque τ generated by them.

Note that, via the control port, the configuration of the internal degrees of freedom q is controlled, which, together with the actuator output position r, determine the behavior of the Dirac structure. Using the internal degrees of freedom, power can be used to do work at the output port, while at the same time the apparent output stiffness can be changed.

Since the Dirac structure realizes a power continuous interconnection of the ports, it defines a constraint relation between the power conjugate variables. This constrained relation can be represented in a matrix expression as

$$\begin{bmatrix} f_S \\ e_C \\ e_I \end{bmatrix} = \underbrace{\begin{bmatrix} 0 & A(q,r) & B(q,r) \\ -A^T(q,r) & 0 & C(q,r) \\ -B^T(q,r) & -C^T(q,r) & 0 \end{bmatrix}}_{D(q,r)} \begin{bmatrix} e_S \\ f_C \\ f_I \end{bmatrix} \tag{3.15}$$

where the skew-symmetric matrix $D(q,r)$ represents the Dirac structure $\mathcal{D}$. Note that the Dirac structure may depend on the configuration variables q and r, but this is not necessary.

The sub-matrix $A(q,r)$ defines the relation between the rate of change of the configuration of the internal degrees of freedom q and the rate of change of the state s of the elastic elements. Similarly, the sub-matrix $B(q,r)$ defines the relation between the rate of change of the output position r and the rate of change of the state s of the elastic elements. In particular, if the state s is determined by the configuration q of the internal degrees of freedom and the actuator output position r via the kinematic relation

$$\lambda : (q,r) \mapsto s \tag{3.16}$$

then, by using (3.10), it follows that

$$A(q,r) := \frac{\partial \lambda}{\partial q}(q,r), \quad B(q,r) := \frac{\partial \lambda}{\partial r}(q,r) \tag{3.17}$$

The sub-matrix $C(q,r)$ defines a gyration effect between forces and velocities. However, such a gyration effect does not exist in the mechanical domain and, without loss of generality, it is assumed $C(q,r) = 0$. This implies that the Dirac structure (3.15) becomes

$$\begin{bmatrix} f_S \\ e_C \\ e_I \end{bmatrix} = \underbrace{\begin{bmatrix} 0 & A(q,r) & B(q,r) \\ -A^T(q,r) & 0 & 0 \\ -B^T(q,r) & 0 & 0 \end{bmatrix}}_{D(q,r)} \begin{bmatrix} e_S \\ f_C \\ f_I \end{bmatrix} \tag{3.18}$$

Observe that the skew-symmetry of the matrix $D(q,r)$ is a necessary condition for power continuity, as stated in (3.2)

$$\begin{bmatrix} e_S & f_C & f_I \end{bmatrix} \begin{bmatrix} f_S \\ e_C \\ e_I \end{bmatrix} = 0 \quad \Leftrightarrow \quad D(q,r) = -D^T(q,r)$$

As a result, via the matrices $A(q,r)$ and $B(q,r)$ the dual relations between the forces exerted by the internal elastic elements and the forces acting on the internal degrees of freedom and the output are defined.

From (3.18), the rate of change of the energy is

$$\begin{aligned} \frac{\mathrm{d}H_e}{\mathrm{d}t}(s) &= \langle \frac{\partial H_e}{\partial s} | \dot{s} \rangle \\ &= \langle e_S | f_S \rangle \\ &= e_S^T \big(A(q,r) f_C + B(q,r) f_I \big) \\ &= -e_C^T f_C - e_I^T f_I \end{aligned}$$

Indeed, the rate of change of energy is determined by the power supplied via the control port and the output port, as stated in (3.6).

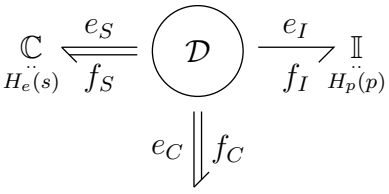

Figure 3.6: Generalized model of a variable stiffness actuator with a load - The internal elastic elements are represented by the multidimensional $\mathbb{C}$-element, described by the energy function $H_e(s)$. The internal degrees of freedom are actuated via the control port (f_C, e_C), while the interconnection with the load is via the output port (f_I, e_I). The $\mathbb{I}$-element represents the load with kinetic energy function $H_p(p)$, i.e., it models the inertial properties.

3.3.3 Variable stiffness actuator and a load

To investigate the behavior of a variable stiffness actuator connected to a load, we use the port-based model shown in Figure 3.6. The $\mathbb{C}$-element, together with its power conjugate variables, and the control port are defined as in Section 3.3.2. The $\mathbb{I}$-element models the inertial properties of the load. In particular, it represents a storage of kinetic energy, given by the energy function $H_p(p) = \frac{1}{2m}p^2$, where p is the momentum of the load and m its mass. By the interconnection of this element to the output port, the port behavior is now given by

$$\begin{aligned} f_I &= \frac{\partial H_p}{\partial p}(p) \quad (= \dot{r}) \\ e_I &= \dot{p} \qquad\qquad (= F) \end{aligned} \tag{3.19}$$

Note that, from (3.18),

$$\dot{p} = -B^T(q,r)e_S = -B^T(q,r)\frac{\partial H_e}{\partial s}(s) \tag{3.20}$$

In order to describe the Dirac structure of the variable stiffness actuator and the load in an input/output port-Hamiltonian system representation, as state of the system, we take

$$x = (s, p, q, r)$$

i.e., the state of the elastic elements, the momentum of the mass, the configuration of the internal degrees of freedom, and the actuator output position, respectively. If we consider the control port (f_C, e_C) as the input/output port of the system, i.e., $(u, -y)$, we can model this system in a input/output port-Hamiltonian form. We then obtain

$$\begin{aligned} \begin{bmatrix} \dot{s} \\ \dot{p} \\ \dot{q} \\ \dot{r} \end{bmatrix} &= \underbrace{\begin{bmatrix} 0 & B(q,r) & 0 & 0 \\ -B^T(q,r) & 0 & 0 & -1 \\ 0 & 0 & 0 & 0 \\ 0 & 1 & 0 & 0 \end{bmatrix}}_{J(x)} \begin{bmatrix} \frac{\partial H}{\partial s} \\ \frac{\partial H}{\partial p} \\ \frac{\partial H}{\partial q} \\ \frac{\partial H}{\partial r} \end{bmatrix} + \underbrace{\begin{bmatrix} A(q,r) \\ 0 \\ 1 \\ 0 \end{bmatrix}}_{g(x)} u \\ y &= \underbrace{\begin{bmatrix} A^T(q,r) & 0 & 1 & 0 \end{bmatrix}}_{g^T(x)} \begin{bmatrix} \frac{\partial H}{\partial s} \\ \frac{\partial H}{\partial p} \\ \frac{\partial H}{\partial q} \\ \frac{\partial H}{\partial r} \end{bmatrix} \end{aligned} \tag{3.21}$$

where $H(s,p) := H_e(s) + H_p(p)$, i.e., the sum of the energy stored in the elastic elements and the kinetic energy stored in the mass.

The rate of change of the energy is given by

$$\begin{aligned}\frac{\mathrm{d}}{\mathrm{d}t}H(x) &= \frac{\partial^T H}{\partial x^T}\frac{\mathrm{d}x}{\mathrm{d}t} \\ &= \frac{\partial^T H}{\partial x^T}J(x)\frac{\partial H}{\partial x} + \frac{\partial^T H}{\partial x^T}g(x)u \\ &= \frac{\partial^T H}{\partial s^T}A(q,r)u \\ &= y^T u = -e_C^T f_C\end{aligned} \tag{3.22}$$

where we used the skew-symmetry of $J(x)$ and that $\frac{\partial H}{\partial q} = 0$. It is observed that indeed energy can be added to the system only via the control port (f_C, e_C).

3.4 Kinematic Properties of Energy Efficient Variable Stiffness Actuators

In this Section, we analyze the port-Hamiltonian model of a variable stiffness actuator, as given in (3.21), with the aim of deriving the kinematic properties that the actuator should have to be energy efficient. In particular, we derive the kinematic properties that allow the apparent output stiffness to be changed without changing the stored elastic energy.

Since the stored energy is a function of the state s of the elastic elements, we investigate the properties of the kinematic map (3.16). In particular, from (3.17) we have:

$$\dot{s} = A(q,r)\dot{q} + B(q,r)\dot{r}$$

that shows how the inputs $\dot{q}$ and the motion of the load $\dot{r}$ affect the state s. Therefore, in the next subsections, we investigate the influences of the matrices $A(q,r)$ and $B(q,r)$ on the energy of the system and on the apparent output stiffness.

3.4.1 Properties and requirements for $A(q,r)$

When the variable stiffness actuator is connected to a load, the total energy of the system is determined by its initial energy and the energy supplied via the control port, as described by (3.22). From (3.22), if $\dim(\ker A(q,r)) \neq 0$, it follows that

$$\dot{H} = 0 \;\Leftarrow\; \dot{q} \in \ker A(q,r) \tag{3.23}$$

This condition states that, if the actuator has a mechanical structure such that the dimension of $\ker A(q,r)$ is not zero, some trajectories of the configuration variables q do not change the total energy of the system. In particular, these trajectories do not change the state s of the internal elastic elements. As shown in [29], if these trajectories of q do change the apparent output stiffness, then the actuator is energy efficient.

Mathematically, it is thus needed that the design of the actuator is such that there exist trajectories of q in the kernel of $A(q,r)$ that change the apparent output stiffness as desired.

This implies that the mechanical design should include a redundancy in the kinematic structure that links the internal degrees of freedom to the elastic elements.

Note that condition (3.23) does not mean that changing the configuration variable q requires no energy at all. It is possible that in the actuation of the internal degrees of freedom opposite work is done, e.g., a positive power flow for actuating one degree of freedom is exactly balanced by a negative power flow for actuating a second degree of freedom. Therefore, even if (3.23) is satisfied, the negative work is lost due to dissipation, but the variable stiffness actuator is still energy efficient, according to the definition given in Section 3.1.

3.4.2 Properties and requirements for $B(q,r)$

By using the kinematic map (3.16), the elastic energy $H_e(s)$ can be expressed in terms of the variables q and r, i.e.,

$$\bar{H}_e(q,r) := (H_e \circ \lambda)(q,r)$$

Using (3.20), the force F exerted on the load can therefore also be written in terms of q and r as

$$\begin{aligned}\bar{F}(q,r) &= -B^T(q,r)\frac{\partial \bar{H}_e}{\partial \lambda} \\ &= -\left(\frac{\partial \lambda}{\partial r}\right)^T \frac{\partial \bar{H}_e}{\partial \lambda}\end{aligned}$$

The apparent output stiffness (3.1) is a local property, i.e., it is defined only for a fixed $r = \bar{r}$ and, therefore, it is given by

$$\begin{aligned}K(q, r=\bar{r}) &= \left(\frac{\partial \bar{F}}{\partial \lambda}\frac{\partial \lambda}{\partial r}\right)\Big|_{r=\bar{r}} \\ &= B^T(q,\bar{r})\frac{\partial^2 \bar{H}_e}{\partial \lambda^2}B(q,\bar{r})\end{aligned} \tag{3.24}$$

where we used that $B(q,\bar{r})$ is not a function of r, and the minus sign is omitted by convention.

By inspecting (3.24), it can be seen that the apparent output stiffness can be varied by changing the configuration variables q if either $\frac{\partial^2 \bar{H}_e}{\partial \lambda^2}$ depends on q, or if $B(q,r)$ depends on q. However, the former option implies that the stored elastic energy changes to achieve a change of stiffness, which contradicts the requirements of energy efficiency. Hence, the latter option should be achieved [29].

From a mathematical point of view, the requirement on $B(q,r)$ is that it should depend on q for all configurations (q,r). This means that the mechanical design should be such that the internal degrees of freedom modulate the transmission between the internal elastic elements and the output.

3.5 Case Studies

In this Section, we model different designs of variable stiffness actuators. In particular, we illustrate how the Dirac structure of a variable stiffness actuator can be derived from the

kinematic analysis of the design. We show that, indeed, all the designs fit in the model described by (3.15) and represented in bond graphs in Figure 3.5.

3.5.1 Design I

The variable stiffness actuator vsaUT has been presented in [28, 30] and the conceptual design is depicted in Figure 3.7. The working principle is based on one zero free length linear spring, characterized by elastic constant k. The spring is connected to the output via a lever arm of variable length, controlled by the linear degree of freedom q_1, and thus q_1 determines how the spring is sensed at the output. The linear degree of freedom q_2 is used to control the actuator output position, i.e. the configuration variable r. The design is such that the maximum length ℓ of the lever arm is longer if compared to s, which means that it is allowed to take $\alpha = 0$.

In order to build the port-based model of this actuator design, we analyze its kinematics. We observe that the state s of the linear zero free length spring is given by

$$s = \ell \sin\phi = \ell \frac{r - q_2}{q_1} \tag{3.25}$$

By taking the total derivative of (3.25), it follows

$$\begin{aligned} \dot{s} &= -\frac{\ell}{q_1} \begin{bmatrix} \frac{r-q_2}{q_1} & 1 \end{bmatrix} \begin{bmatrix} \dot{q}_1 \\ \dot{q}_2 \end{bmatrix} + \frac{\ell}{q_1} \dot{r} \\ &= f_S \end{aligned}$$

From this equation, we can identify the matrices $A(q,r)$ and $B(q,r)$, by using (3.16), *i.e.*

$$\begin{aligned} A(q,r) &= -\frac{\ell}{q_1} \begin{bmatrix} \frac{r-q_2}{q_1} & 1 \end{bmatrix} \\ B(q,r) &= \frac{\ell}{q_1} \end{aligned} \tag{3.26}$$

with which it it possible to build the skew symmetric matrix $D(q,r)$ that represents the Dirac structure as defined in (3.15).

Due to the linearity of the spring, the energy stored in the spring is given by the function $H(s) = \frac{1}{2}ks^2$, i.e.

$$H(q,r) = \frac{1}{2}k \left(\ell \frac{r - q_2}{q_1} \right)^2$$

and the force exerted by the spring is given by

$$e_S = \frac{\partial H}{\partial s}(s) = k\, s = k\, \ell \frac{r - q_2}{q_1}$$

The output force $e_I = F$ of the actuator is then given by

$$e_I = -B^T(q,r) e_S = -\frac{\ell}{q_1} \frac{\partial H}{\partial s} = -k\, \ell^2 \frac{r - q_2}{q_1^2}$$

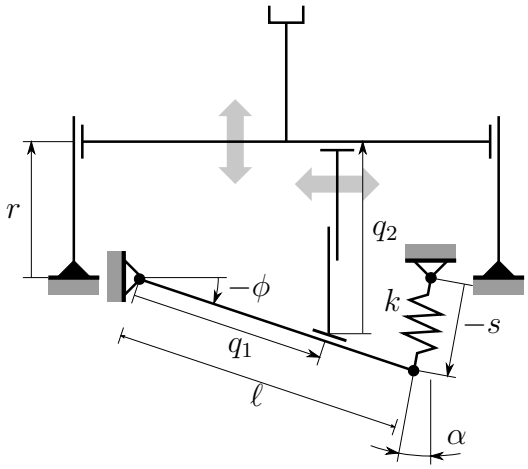

Figure 3.7: Concept design I - The functional principle of the concept is a lever arm of variable length q_1, which connects the zero free length linear spring, with elastic constant k, to the output. The effective length of the lever arm is determined by the linear degree of freedom q_1. The actuator output position r is controlled by the linear degree of freedom q_2 [28].

Using the definition of the actuator output stiffness (3.1), we find that for this design the output stiffness K is given by

$$K = \frac{\partial F}{\partial r} = \frac{\partial^2 H}{\partial r^2} = k\left(\frac{\ell}{q_1}\right)^2 \tag{3.27}$$

Equation (3.27) shows that the apparent output stiffness only depends on the degree of freedom q_1, i.e. the effective length of the lever arm.

3.5.2 Design II

The variable stiffness actuator AwAS has been presented in [31] and the conceptual design is depicted in Figure 3.8. The working principle is based on two linear springs, characterized by elastic constants k. The springs are connected to the output via a lever arm of variable length, controlled by the linear degree of freedom q_1, and thus q_1 determines how the springs are sensed at the output. The rotational degree of freedom q_2 is used to control the actuator output position, i.e. the configuration variable r.

In order to build the port-based model of this actuator design, we take the same approach and we analyze the kinematics of this design to derive the Dirac structure. We observe that the state s_i, with $i = 1, 2$, of each one of the linear springs is given by

$$s = \begin{bmatrix} s_1 \\ s_2 \end{bmatrix} = \begin{bmatrix} l_0 - q_1 \sin\alpha \\ l_0 + q_1 \sin\alpha \end{bmatrix} \tag{3.28}$$

where $\alpha = q_2 - r$ and l_0 denotes the spring lengths when $\alpha = 0$. The rate of change of the state s is obtained by taking the total derivative of (3.28) and is given by

$$\dot{s} = \begin{bmatrix} \dot{s}_1 \\ \dot{s}_2 \end{bmatrix} = \begin{bmatrix} -\sin\alpha\ \dot{q}_1 - q_1 \cos\alpha\ \dot{q}_2 + q_1 \cos\alpha\ \dot{r} \\ \sin\alpha\ \dot{q}_1 + q_1 \cos\alpha\ \dot{q}_2 - q_1 \cos\alpha\ \dot{r} \end{bmatrix} = \begin{bmatrix} f_{S_1} \\ f_{S_2} \end{bmatrix}$$

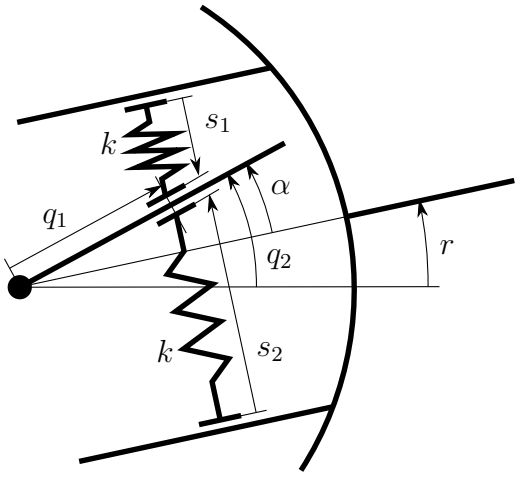

Figure 3.8: Concept design II - The functional principle of the concept is a lever arm of variable length q_1, which connects the two linear springs, with elastic constant k, to the output. The effective length of the lever arm is determined by the linear degree of freedom q_1. The actuator output position r is controlled by the rotational degree of freedom q_2 [31].

From this equation, we can identify the matrices $A(q,r)$ and $B(q,r)$, by using (3.16), *i.e.*

$$\begin{aligned} A(q,r) &= \begin{bmatrix} -\sin\alpha & -q_1\cos\alpha \\ \sin\alpha & q_1\cos\alpha \end{bmatrix} \\ B(q,r) &= \begin{bmatrix} q_1\cos\alpha \\ -q_1\cos\alpha \end{bmatrix} \end{aligned} \tag{3.29}$$

with which it is possible to build the skew-symmetric matrix $D(q,r)$ that represents the Dirac structure as defined in (3.15).

Due to the linearity of the springs, the energy stored in each spring is given by the function $H_i(s_i) = \frac{1}{2}ks_i^2$. The total energy stored in the springs is $H(s_1,s_2) = \frac{1}{2}ks_1^2 + \frac{1}{2}ks_2^2$, i.e.

$$H(q,r) = k\left(l_0^2 + q_1^2\sin^2\alpha\right)$$

and the forces exerted by the spring are given by

$$e_S = \begin{bmatrix} e_{S_1} \\ e_{S_2} \end{bmatrix} = \begin{bmatrix} \frac{\partial H}{\partial s_1} \\ \frac{\partial H}{\partial s_2} \end{bmatrix} = \begin{bmatrix} ks_1 \\ ks_2 \end{bmatrix} = \begin{bmatrix} k\left(l_0 - q_1\sin\alpha\right) \\ k\left(l_0 + q_1\sin\alpha\right) \end{bmatrix}$$

The output force $e_I = F$ of the actuator is given by

$$\begin{aligned} e_I &= -B^T(q,r)e_S \\ &= -q_1\cos\alpha\left(\frac{\partial H}{\partial s_1} - \frac{\partial H}{\partial s_2}\right) \\ &= -2kq_1^2\cos\alpha\sin\alpha \end{aligned}$$

Using the definition of the actuator output stiffness (3.1), we find that for this design the output stiffness K is given by

$$K = \frac{\partial F}{\partial r} = 2kq_1^2\cos(2\alpha) \tag{3.30}$$

Equation (3.30) shows that the apparent output stiffness depends on both the degrees of freedom q_1 and q_2.

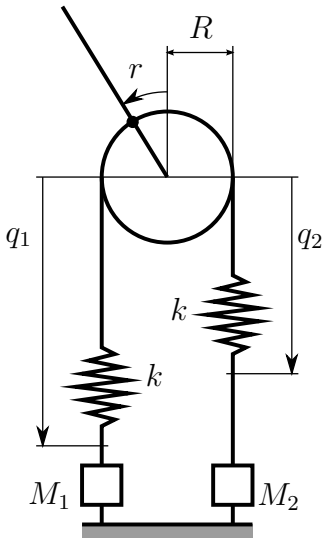

Figure 3.9: Concept design III - This design is based on two series elastic actuators in an antagonistic setup. The linear motors M_1 and M_2 generate linear displacements q_1 and q_2. The nonlinear quadratic springs have elastic constant k. By operating the motors in common mode, the apparent output stiffness of the actuator changes, while by operating the motors in differential mode the equilibrium of the actuator output position r changes [32].

3.5.3 Design III

The variable stiffness actuator VSA has been presented in [32] and the conceptual design is depicted in Figure 3.9. The working principle is based on two nonlinear quadratic springs, characterized by elastic constants k, in series with two linear motors M_1 and M_2, which generates the two linear displacements q_1 and q_2, respectively. When the motors are operated in common mode, the actuator output stiffness is changed. When the motors are operated in differential mode, the actuator output position r is changed.

In order to build the port-based model of this actuator design, we take the same approach and we analyze the kinematics of this design to derive the Dirac structure. We observe that the state s_i, with $i = 1, 2$, of each one of the nonlinear springs is given by

$$s = \begin{bmatrix} s_1 \\ s_2 \end{bmatrix} = \begin{bmatrix} q_1 - Rr \\ q_2 + Rr \end{bmatrix} \tag{3.31}$$

where R is the radius of the pulley. By taking the total derivative of (3.31), we obtain

$$\dot{s} = \begin{bmatrix} \dot{s}_1 \\ \dot{s}_2 \end{bmatrix} = \begin{bmatrix} \dot{q}_1 - R\dot{r} \\ \dot{q}_2 + R\dot{r} \end{bmatrix} = \begin{bmatrix} f_{S_1} \\ f_{S_2} \end{bmatrix}$$

From this equations, we can identify the matrices $A(q, r)$ and $B(q, r)$, by using (3.16), i.e.

$$A(q, r) = \begin{bmatrix} 1 & 0 \\ 0 & 1 \end{bmatrix}, \quad B(q, r) = \begin{bmatrix} -R \\ R \end{bmatrix}$$

Due to the nonlinearity of the the springs, which are quadratic, the energy stored in the springs is given by the function $H_i(s_i) = \frac{1}{3}ks_i^3$. The total energy stored in the springs is $H(s_1, s_2) = \frac{1}{3}ks_1^3 + \frac{1}{3}ks_2^3$, i.e.

$$H(q, r) = \frac{1}{3}k\left(q_1 - Rr\right)^3 + \frac{1}{3}k\left(q_2 + Rr\right)^3$$

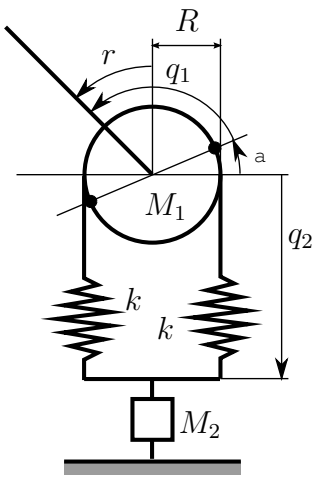

Figure 3.10: Concept design IV - In this design, the change of the stiffness and the actuator output position r is decoupled. The linear motor M_2 generates a linear displacement q_2 and is used for changing the apparent output stiffness of the actuator. The equilibrium of the output joint position r is determined by q_1 [33].

and the forces exerted by the spring are given by

$$e_S = \begin{bmatrix} e_{S_1} \\ e_{S_2} \end{bmatrix} = \begin{bmatrix} \frac{\partial H}{\partial s_1} \\ \frac{\partial H}{\partial s_2} \end{bmatrix} = \begin{bmatrix} k s_1^2 \\ k s_2^2 \end{bmatrix} = \begin{bmatrix} k\left(q_1 - Rr\right)^2 \\ k\left(q_2 + Rr\right)^2 \end{bmatrix}$$

The output force $e_I = F$ of the actuator is given by

$$\begin{aligned} e_I &= -B^T(q, r)\, e_S \\ &= -R\left(-\frac{\partial H}{\partial s_1} + \frac{\partial H}{\partial s_2}\right) \\ &= -kR\left(-\left(q_1 - Rr\right)^2 + \left(q_2 + Rr\right)^2\right) \end{aligned}$$

Using the definition of the actuator output stiffness (3.1), we find that for this design the output stiffness K is given by

$$K = \frac{\partial F}{\partial r} = -2kR^2(q_1 + q_2) \tag{3.32}$$

Equation (3.32) shows that the apparent output stiffness depends on both the degrees of freedom q_1 and q_2.

3.5.4 Design IV

The variable stiffness actuator VSJ has been presented in [33] and the conceptual design is depicted in Figure 3.10. The working principle is based on two nonlinear quadratic springs, characterized by elastic constants k. In this design, the change of the stiffness and the output joint position is decoupled. The linear motor M_2 generates a linear displacement q_2 and is used for changing the apparent output stiffness of the actuator. The output position r is determined by q_1. Note that the end effector can rotate independently from the pulley.

In order to build the port-based model of this actuator design, we take the same approach and we analyze the kinematics of this design to derive the Dirac structure. We observe that the states s_i, with $i = 1, 2$, of each nonlinear spring is given by

$$s = \begin{bmatrix} s_1 \\ s_2 \end{bmatrix} = \begin{bmatrix} q_2 - R\alpha \\ q_2 + R\alpha \end{bmatrix} \tag{3.33}$$

where R is the radius of the pulley and $\alpha = -q_1 + r + \frac{\pi}{2}$. By taking the total derivative of (3.33), we obtain

$$\dot{s} = \begin{bmatrix} \dot{s}_1 \\ \dot{s}_2 \end{bmatrix} = \begin{bmatrix} \dot{q}_2 + R\dot{q}_1 - R\dot{r} \\ \dot{q}_2 - R\dot{q}_1 + R\dot{r} \end{bmatrix} = \begin{bmatrix} f_{S_1} \\ f_{S_2} \end{bmatrix}$$

From this equations, we can identify the matrices $A(q, r)$ and $B(q, r)$, by using (3.16), i.e.

$$A(q, r) = \begin{bmatrix} R & 1 \\ -R & 1 \end{bmatrix}, \quad B(q, r) = \begin{bmatrix} -R \\ R \end{bmatrix}$$

Due to the nonlinearity of the springs, which are quadratic, the energy stored in the springs is given by the function $H_i(s_i) = \frac{1}{3}ks_i^3$. The total energy stored in the springs is $H(s_1, s_2) = \frac{1}{3}ks_1^3 + \frac{1}{3}ks_2^3$, i.e.

$$H(q, r) = \frac{1}{3}k\left(q_2 - R\alpha\right)^3 + \frac{1}{3}k\left(q_2 + R\alpha\right)^3$$

and the forces exerted by the spring are given by

$$e_S = \begin{bmatrix} e_{S_1} \\ e_{S_2} \end{bmatrix} = \begin{bmatrix} \frac{\partial H}{\partial s_1} \\ \frac{\partial H}{\partial s_2} \end{bmatrix} = \begin{bmatrix} ks_1^2 \\ ks_2^2 \end{bmatrix} = \begin{bmatrix} k\left(q_2 - R\alpha\right)^2 \\ k\left(q_2 + R\alpha\right)^2 \end{bmatrix}$$

The output force $e_I = F$ of the actuator is given by

$$\begin{aligned} e_I &= -B^T(q, r)\, e_S \\ &= -R\left(-\frac{\partial H}{\partial s_1} + \frac{\partial H}{\partial s_2}\right) \\ &= -kR\left(-\left(q_2 - R\alpha\right)^2 + \left(q_2 + R\alpha\right)^2\right) \end{aligned}$$

Using the definition of the actuator output stiffness (3.1), we find that for this design the output stiffness K is given by

$$K = \frac{\partial F}{\partial r} = -4kR^2 q_2 \tag{3.34}$$

Equation (3.34) shows that the apparent output stiffness depends only on the degrees of freedom q_2.

3.6 Conclusions

In this Chapter, we presented a generalized model for variable stiffness actuators. The model finds its fundamentals in port-based thinking, according which every dynamical system can be seen as a network structure, i.e. a Dirac structure. With respect to that, any variable stiffness actuator is a network of elements, which are commonly used in this class of actuators such as internal elastic elements and internal actuated degrees of freedom. However, the network describes also how this basic elements are interconnected to each other in the specific mechanical design. By deriving the Dirac structure for some variable stiffness actuators presented in the literature, we could make explicit the different mechanisms in an unified model.

Chapter 4

Port-based performance analysis of variable stiffness actuators

In this Chapter, we define a performance metric for variable stiffness actuators, that measures in dynamic conditions how efficient the design is in transferring the power from the internal degrees of freedom to the output, irrespective of the dynamic behavior of the load. We show that, for different principle designs, the performance measure is strictly related to the kinematic properties of the actuator and it is totally independent of the task realized by the load. The performance metric is derived from the analysis of a port-based model of variable stiffness actuators, introduced in [28], which highlights the power flow inside the actuator structure and of the actuator towards the external environment.

4.1 Port-based Modeling Framework

Throughout this Chapter, some fundamental interconnection elements are used to make explicit the Dirac structure that models the variable stiffness actuators. Essentially, these elements are examples of Dirac structures and, since a composition of Dirac structures is again a Dirac structure, these basic elements can give more insights when modeling the behavior of a complex system. Specifically,

- a 1-*junction* defines a common flow interconnection, e.g. a rigid connection between two masses such as the actuator output port and a load. In order to satisfy (3.2), the behavior of a 1-junction, with N connected bonds, satisfies

$$f_1 = \cdots = f_N, \quad \sum_{i=1}^{N} e_i = 0 \tag{4.1}$$

- the dual of a 1-junction is a 0-*junction*, which defines a common effort interconnection. The behavior of a 0-junction, for N connected bonds, is given by

$$\sum_{i=1}^{N} f_i = 0, \quad e_1 = \cdots = e_N \tag{4.2}$$

- a $\mathbb{MTF}$-element (Modulated TransFormation) defines a power continuous transformation between two ports. An example is an ideal gearbox: if the input and

the output of the gearbox are characterized by power conjugate variables $(f_{\text{in}}, e_{\text{in}})$ and $(f_{\text{out}}, e_{\text{out}})$ and α is the transformation ratio (either a scalar or a matrix), the behavior for the two ports is described by

$$f_{\text{in}} = \alpha\, f_{\text{out}}, \quad e_{\text{out}} = \alpha^T\, e_{\text{in}}$$

It is readily verified that any combination of these elements again yields a power continuous interconnection structure.

4.2 Port-based Model of Variable Stiffness Actuators

In this Section, we describe a generic port-based model of variable stiffness actuators. This is possible by identifying common components for all actuators, and describing the interconnection of these components in a generic way by means of a Dirac structure. For any specific actuator, an explicit representation of the Dirac structure can be found by analyzing the kinematics of the design. Kinematic and dynamic properties of different designs can then be compared by analyzing the respective Dirac structure representations.

The generic port-based model has been introduced in [28, 29], and here we intend to revisit the most important aspects relevant for the remainder of this Chapter.

4.2.1 Variable stiffness actuators as Dirac structures

In deriving a generic model for variable stiffness actuators, we assume that:

- the actuator output is one dimensional, and is characterized by the generalized configuration variable $r \in \mathcal{R}$;
- the actuator has a number m of internal elastic elements, e.g. springs, which can be either linear or nonlinear. The elastic elements are characterized by state $s \in \mathcal{S}$, and by the positive semidefinite energy function $H(s) : \mathcal{S} \to \mathbb{R}$ that describes the amount of stored elastic energy;
- internally, there are $n \geq m$ actuated degrees of freedom, characterized by the generalized configuration variables $q \in \mathcal{Q}$. These degrees of freedom determine how the elastic elements are sensed at the output and, in particular, they determine the apparent output stiffness K of the actuator, defined as

$$K := \frac{\delta F}{\delta r} \tag{4.3}$$

i.e., the ratio of the infinitesimal change of the actuator generalized output force δF as a result of an infinitesimal displacement of the actuator output position δr.

Moreover, in our model, we assume that internal friction and inertias can be neglected, since we focus on the working principles and the kinematics of the actuator design, rather than on the details of the implementation.

By these assumptions, we identify the common components of variable stiffness actuator designs, i.e. the elastic elements, the internal degrees of freedom, and the interaction port,

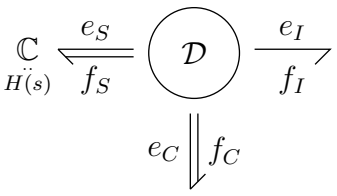

Figure 4.1: Port-based representation of variable stiffness actuators - The $\mathcal{D}$-element represents the Dirac structure. The internal elastic elements are represented by the multidimensional $\mathbb{C}$-element, with state s and elastic energy function $H(s)$. The internal degrees of freedom are actuated via the control port (f_C, e_C), while the interconnection with the load is via the output port (f_I, e_I).

and we derive how these components are connected to each other by an analysis of the kinematics. From this analysis, the mathematical representation of the Dirac structure can then be derived.

The generic model of a variable stiffness actuator is depicted, using bond graphs, in Figure 4.1. The $\mathbb{C}$-element represents the storage of elastic energy, due to the internal elastic elements. The power conjugate variables (f_S, e_S) satisfy

$$\dot{s} = f_S, \quad e_S = \frac{\partial H}{\partial s}(s)$$

The control port is characterized by the power conjugate variables (f_C, e_C), which correspond to $(\dot{q}, \tau)$, i.e. the rate of change of the configuration variable q of the internal degrees of freedom and the collocated generalized forces τ, respectively. The interaction port is characterized by the power conjugate variables (f_I, e_I), which correspond to $(\dot{r}, F)$, i.e. the rate of change of the actuator output position r and the generalized output force F. The Dirac structure $\mathcal{D}(q, r)$ defines the interconnection and it is explicitly allowed to depend on the configuration variables q and r. The requirement of power continuity imposes a constraint relation between the power conjugate variables, that can be expressed in a matrix form as

$$\begin{bmatrix} f_S \\ e_C \\ e_I \end{bmatrix} = \underbrace{\begin{bmatrix} 0 & A(q,r) & B(q,r) \\ -A^T(q,r) & 0 & 0 \\ -B^T(q,r) & 0 & 0 \end{bmatrix}}_{D(q,r)} \begin{bmatrix} e_S \\ f_C \\ f_I \end{bmatrix} \tag{4.4}$$

in which the matrix $D(q, r)$ represents the Dirac structure. The skew-symmetry of $D(q, r)$ establishes the power continuity of the interconnection, as stated in (3.2).

The Dirac structure of Figure 4.1 is made explicit in Figure 4.2. The $\mathbb{MTF}$-elements implement the maps $A(q, r)$ and $B(q, r)$, such that

$$\bar{f}_C = A(q,r)\, f_C \qquad \bar{f}_I = B(q,r)\, f_I$$
$$e_C = A^T(q,r)\, \bar{e}_C \qquad e_I = B^T(q,r)\, \bar{e}_I$$

The 0-junction represents a power continuous common effort connection, defined in (4.2), such that

$$\bar{f}_S = \bar{f}_I + \bar{f}_C, \quad \bar{e}_S = \bar{e}_I = \bar{e}_C$$

The Dirac structure representation is completed with the 1-junction, which realizes a power continuous common flow connection as defined in (4.1), such that

$$f_S = \bar{f}_S, \quad \bar{e}_S = -e_S$$

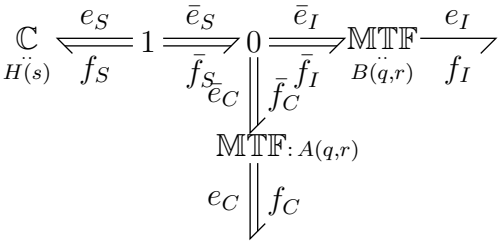

Figure 4.2: Variable stiffness actuators - The Dirac structure expressed in (4.4) can be detailed by using two $\mathbb{MTF}$-elements, which implement the maps defined by $A(q,r)$ and $B(q,r)$. The 1- and 0-junctions implement power continuous connections, with common flow and common effort, respectively.

The sub-matrix $A(q,r)$ defines the relation between the rate of change of the state s of the elastic elements and the rate of change of the configuration of the internal degrees of freedom q. Similarly, the sub-matrix $B(q,r)$ defines the relation between the rate of change of the state s of the springs and the rate of change of the output position r. Hence, the particular structure of $A(q,r)$ and $B(q,r)$ can be derived from a kinematic analysis of the actuator design.

4.2.2 Kinematic Structure of Variable Stiffness Actuators

It is assumed that the state s of the internal elastic elements is determined by the configuration q of the internal degrees of freedom and the output position r via the kinematic relation

$$\begin{array}{rccc} \lambda: & \mathcal{Q}\times\mathcal{R} & \to & \mathcal{S} \\ & (q,r) & \mapsto & s \end{array}$$

Therefore, the tangent map $\lambda_* : T_q\mathcal{Q} \times T_r\mathcal{R} \to T_s\mathcal{S}$ and the cotangent map $\lambda^* : T_s^*\mathcal{S} \to T_q^*\mathcal{Q} \times T_r^*\mathcal{R}$ are naturally defined [34], where $T_q\mathcal{Q}$ ($T_q^*\mathcal{Q}$), $T_r\mathcal{R}$ ($T_r^*\mathcal{R}$) and $T_s\mathcal{S}$ ($T_s^*\mathcal{S}$) are the tangent (cotangent) spaces to the manifolds $\mathcal{Q}$, $\mathcal{R}$ and $\mathcal{S}$ at q, r and s, respectively.

The tangent maps can be expressed in the natural coordinates on the tangent space as

$$\lambda_* = \left(\frac{\partial\lambda}{\partial q}(q,r), \frac{\partial\lambda}{\partial r}(q,r)\right) =: (A(q,r), B(q,r))$$

Dually, the cotangent map can be expressed in the natural coordinates as

$$\lambda^* = \left(\frac{\partial^T\lambda}{\partial q^T}(q,r), \frac{\partial^T\lambda}{\partial r^T}(q,r)\right) =: \left(A^T(q,r), B^T(q,r)\right)$$

which completes the mathematical representation of the Dirac structure (4.4).

As observed already from (4.4), the tangent maps define the rate of change of the state s of the elastic elements as a result of the flows f_C and f_I. In particular, considering the natural coordinates on the tangent spaces, we have

$$\dot{s} = A(q,r)\dot{q} + B(q,r)\dot{r} \tag{4.5}$$

In Figure 4.3, the tangent map λ_* is visualized. More specifically, note that each one of the maps defined by $A(q,r)$ and $B(q,r)$ have an image space, which is a subspace of the

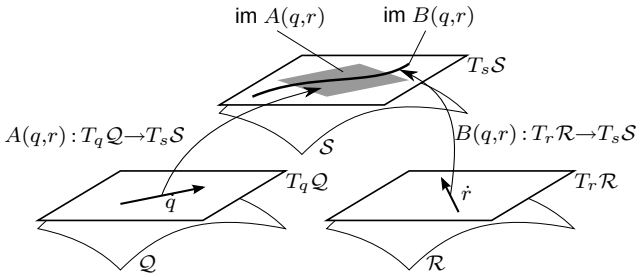

Figure 4.3: Maps between the tangent spaces $T_q\mathcal{Q}$, $T_r\mathcal{R}$ and $T_s\mathcal{S}$ - The image spaces of the maps $A(q,r)$ and $B(q,r)$ are a subspace of $T_s\mathcal{S}$.

tangent space $T_s\mathcal{S}$. The dimensions of the image of $A(q,r)$ depend on the number of internal elastic elements and the number of internal degrees of freedom, while the image of $B(q,r)$ is always one-dimensional, since the actuator output port is assumed to have only one degree of freedom.

Under the map λ^*, it follows that $e_C = -A^T(q,r)e_S$ and $e_I = -B^T(q,r)e_S$, which state that the efforts τ and F depend on the effort e_S generated by the elastic elements. In particular, considering the natural coordinates on the cotangent space, through the map $A^T(q,r)$ and the map $B^T(q,r)$ respectively, we obtain

$$\tau = -A^T(q,r)\mathrm{d}H, \quad F = -B^T(q,r)\mathrm{d}H$$

where $\mathrm{d}H$ is the exact one-form on the cotangent space $T_s^*\mathcal{S}$ representing the effort e_S. In natural coordinates, we have

$$\mathrm{d}H = \frac{\partial H}{\partial s} \tag{4.6}$$

We use this kinematic analysis to compute the power flows in variable stiffness actuators and, more specifically, in the various bonds of the model depicted in Figure 4.2.

4.3 Power Flow Analysis

In this Section, we provide a detailed analysis of the power flows in variable stiffness actuators using the port-based model. By identifying the kinematic structure of the actuators, we highlight the power transferred from the control port, i.e. the internal degrees of freedom, to the internal elastic elements and to the output port. This analysis is facilitated by a change of coordinates on $T_s\mathcal{S}$ and $T_s^*\mathcal{S}$ that makes these power flows explicit.

4.3.1 Change of Coordinates

The power balance between the internal elastic elements, the control and the interaction ports is given in natural coordinates by

$$\langle \mathrm{d}H | \dot{s} \rangle = \langle \mathrm{d}H | A(q,r)\dot{q} \rangle + \langle \mathrm{d}H | B(q,r)\dot{r} \rangle$$

and, therefore, the power flows are determined by the tangent maps $A(q,r)$ and $B(q,r)$. To further investigate the power flows, we define a new set of coordinates on $T_s\mathcal{S}$ and $T_s^*\mathcal{S}$ by using the image of the map $B(q,r)$.

Since the actuator output has only one degree of freedom, i.e., r is a scalar, the image of the tangent map $B(q,r)$ defines a line on $T_s\mathcal{S}$. Let $b^{\|}$ be a unit vector such that

$$\text{im } B(q,r) = \text{span } \{b^{\|}\}$$

Then, a set of $m-1$ unit vectors $b^{\perp}$ exists, such that

$$\text{span } \{b^{\perp}\} =: \text{im } B^{\perp}(q,r)$$

The subspace im $B^{\perp}(q,r)$ is the orthogonal complement to im $B(q,r)$, and it thus means that $\{b^{\|}, b^{\perp}\}$ forms a set of coordinate vectors that spans the tangent space $T_s\mathcal{S}$, i.e., $T_s\mathcal{S} = \text{im } B(q,r) \oplus \text{im } B^{\perp}(q,r)$.

Orthogonality on the tangent space $T_s\mathcal{S}$ is only defined if a proper metric is defined on it. Elements from $T_s\mathcal{S}$ represent the rate of change of the state s of the elastic elements, which may be equivalently considered as infinitesimal displacements δs. A physically meaningful metric to measure δs is the stiffness matrix [35]. Considering the natural coordinates on $T_s\mathcal{S}$, the stiffness matrix M is, therefore, given by

$$M = \frac{\partial^2 H}{\partial s^2}$$

where $H(s)$ describes the amount of elastic energy stored in the elastic elements. Note that the norm $\|\delta s\|_M^2 = \delta s^T M \delta s$ induced by the metric M has the units of energy.

As the metric M defines the inner product on $T_s\mathcal{S}$, the set $b^{\perp}$ is found by requiring

$$\langle b^{\|}, b_i^{\perp} \rangle_M = 0, \qquad i = 1, \ldots, m-1$$

where $\langle \cdot, \cdot \rangle_M$ denotes the inner product with respect to the metric M.

We can now define a change of coordinates from the natural coordinates on $T_s\mathcal{S}$ to the new defined coordinates. Let S_b be a matrix describing the change of coordinates as

$$S_b = \begin{bmatrix} b^{\|} & b^{\perp} \end{bmatrix} \tag{4.7}$$

If $\dot{s}$ is an element of $T_s\mathcal{S}$, expressed in the natural coordinates, and $\dot{s}^b$ the same element, expressed in the coordinates $\{b^{\|}, b^{\perp}\}$, it follows that

$$\dot{s} = S_b \dot{s}^b \tag{4.8}$$

and, since the change of coordinates is by construction invertible, $\dot{s}^b = S_b^{-1}\dot{s}$.

The elements on $T_s\mathcal{S}$ defined in (4.5) can be expressed in the new coordinates. In particular, we have

$$\begin{aligned} \dot{s}^b &= S_b^{-1}\dot{s} \\ &= S_b^{-1}\left(A(q,r)\dot{q} + B(q,r)\dot{r}\right) \\ &=: S_b^{-1}\left(\dot{s}_q + \dot{s}_r\right) \\ &=: \begin{pmatrix} \dot{s}_q^{\|} \\ \dot{s}_q^{\perp} \end{pmatrix} + \begin{pmatrix} \dot{s}_r^{\|} \\ \dot{s}_r^{\perp} \end{pmatrix} =: \begin{pmatrix} \dot{s}^{\|} \\ \dot{s}^{\perp} \end{pmatrix} \end{aligned} \tag{4.9}$$

The element $\dot{s}_r^{\perp}$ is zero by construction of the coordinate set.

Essentially, with this change of coordinates, from the real elastic element $\mathbb{C}$ with state s, we create two virtual storage elements $\mathbb{C}^{\|}$ and $\mathbb{C}^{\perp}$, with states $s^{\|}$ and $s^{\perp}$, respectively. By construction, the state $s^{\|}$ is one-dimensional, and the state $s^{\perp}$ has dimension $m-1$. This scenario is depicted in Figure 4.4. From (4.9), it can be noted that the storage elements $\mathbb{C}^{\perp}$ is not connected to the output, i.e., it captures the energy supplied via the control port without redistributing it to the output.

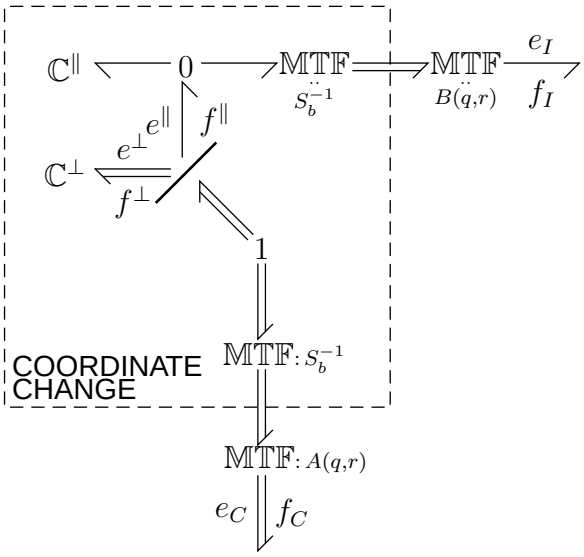

Figure 4.4: Visualization of the storage elements - The change of coordinates can be realized by two $\mathbb{MTF}$-elements and a power splitter (the diagonally oriented solid line). The two $\mathbb{C}$-elements represent the virtual storage elements.

4.3.2 Power Flows

Only when the change of coordinates (4.8) is also applied to elements of the cotangent space $T_s^*\mathcal{S}$, the power flows to $\mathbb{C}^{\|}$ and $\mathbb{C}^{\perp}$ can be analyzed. One-forms on $T_s^*\mathcal{S}$ transform under the change of coordinates as [34]

$$\mathrm{d}H^b = \mathrm{d}H\, S_b =: \begin{pmatrix} \mathrm{d}H^{\|} & \mathrm{d}H^{\perp} \end{pmatrix} \tag{4.10}$$

The port behavior of the two virtual storage elements $\mathbb{C}^{\|}$ and $\mathbb{C}^{\perp}$ can now be properly defined by using (4.6), (4.9), (4.10), i.e.,

$$\begin{aligned} \dot{s}^{\|} &= \dot{s}_q^{\|} + \dot{s}_r^{\|}, & e_S^{\|} &= \mathrm{d}H^{\|} \\ \dot{s}^{\perp} &= \dot{s}_q^{\perp}, & e_S^{\perp} &= \mathrm{d}H^{\perp} \end{aligned}$$

The power supplied via the control port is given by

$$P_C = \langle e_C | f_C \rangle = -\langle A^T(q,r)\, e_S | \dot{q} \rangle = -\langle \mathrm{d}H | \dot{s}_q \rangle$$

and expressions for the power flows from the control port toward the two virtual storage elements are

$$P_C^{\|} = -\langle \mathrm{d}H^{\|} | \dot{s}_q^{\|} \rangle \tag{4.11}$$

$$P_C^{\perp} = -\langle \mathrm{d}H^{\perp} | \dot{s}_q^{\perp} \rangle \tag{4.12}$$

It is readily verified that the change of coordinates is power continuous, i.e.,

$$P_C^{\|} + P_C^{\perp} = P_C$$

Remark 4.3.1 Note that we cannot exactly know how much power goes to the output port, since the dynamic behavior of the load has not been modeled. This implies that we cannot

find the total power flow to $\mathbb{C}^{\|}$. However, since there is a direct connection between the $\mathbb{C}^{\|}$ and the output, realized by the 0-junction, the power flow $P^{\|}$ is, in any case, used to do work on the output. On the other hand, the power flow $P^{\perp}$ is totally captured by $\mathbb{C}^{\perp}$. It represents the power supplied by the control port, which cannot be used to do any work on the output, but is instead stored internally due to the kinematics of the actuator.

The image of the map $B(q,r)$ defines an involutive distribution on $\mathcal{S}$ with dimension one, since the output has only one degree of freedom. If the set $b^{\perp}$ is not empty, then the manifold $\mathcal{S}$ is of dimension $m > 1$, and hence for any configuration (q,r), there exists a foliation $\mathcal{S}_r$ that is the integral manifold of this distribution [34]. This integral manifold is also one-dimensional. Since the energy function $H(s)$ is positive semidefinite by definition, it has a minimum on $\mathcal{S}_r$, which defines how much energy can go out from the elastic elements via the output port. This minimum is however, in general, not the same as the global minimum of $H(s)$ on $\mathcal{S}$. Hence, there is energy stored in the elastic elements that cannot be used to do work on the output. ◁

4.4 Performance Measure

The change of coordinates and the subsequent definition of power flows in (4.11) and (4.12), as visualized in Figure 4.4, give rises to the definition of a measure of performance. As already observed, the virtual power flow $P_C^{\perp}$ is disconnected from the output, and thus it cannot be used to do work at the output. Intuitively, the measure

$$\mu = \frac{P_C^{\perp}}{P_C} \tag{4.13}$$

is an indicator for the performance of the actuator design, since it tells how much of the power supplied via the control port is, in fact, lost: the lower this measure, the higher the performance.

Note that μ is a dynamic measure of power flows. This means that the measure does not say anything about the energy balance of the actuator. In particular, since the decomposition of the virtual storage elements can be configuration dependent, it is possible that a power flow to $\mathbb{C}^{\perp}$ is stored, and, in a different configuration, used to do work at the output. However, the rationale in this analysis is that instantaneous power provided by the controller should provide an instantaneous power flow to the output, in order to achieve efficient actuation of the load.

4.5 Analysis of Variable Stiffness Actuator Designs

In this Section, we analyze the working principles of three designs of variable stiffness actuators, which realize a variable output stiffness by means of different kinematic structures. As follows from the previous Sections, the power flows to the virtual storage elements are defined by the maps $A(q,r)$ and $B(q,r)$, i.e., by the kinematic properties of the actuator design. First, we present the model of the designs in a port-based formalism, and, then, we proceed by evaluating the performance measure μ, as defined in (4.13).

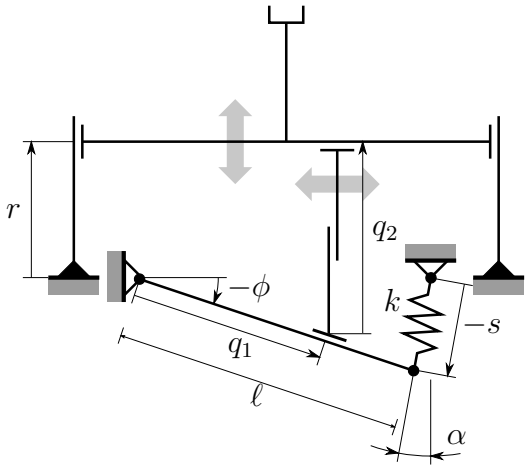

Figure 4.5: Variable stiffness actuator using a lever arm of variable length - The functional principle of the concept is a lever arm of variable length q_1, which connects the zero free length linear spring, with elastic constant k, to the output. The effective length of the lever arm is determined by the linear degree of freedom q_1. The actuator output position r is controlled by the linear degree of freedom q_2 [28].

4.5.1 Design Based on a Lever Arm of Variable Length

In some designs, such as the vsaUT [28], AwAS [36], and HDAU [37], the change of the output stiffness is mechanically decoupled from the change of the output position. In particular, the change of the output stiffness is realized through a change of the transmission ratio between the internal springs and the actuator output by means of a lever arm of variable length.

As an example of this category of variable stiffness actuators, we analyze the vsaUT, which is conceptually depicted in Figure 4.5. The working principle is based on one zero free length linear spring, characterized by elastic constant k. The spring is connected to the output via a lever arm of variable length, controlled by the linear degree of freedom q_1, and thus q_1 determines how the spring is sensed at the output. The linear degree of freedom q_2 is used to control the actuator output position, i.e. the configuration variable r. The design is such that the maximum length ℓ of the lever arm is sufficiently large compared to the maximum elongation of the spring, so that we can assume $\alpha \approx 0$.

In order to build the port-based model of this actuator design, we analyze its kinematics. We observe that the state s of the linear zero free length spring is given by

$$s = \ell \sin\phi = \ell \frac{r - q_2}{q_1} \tag{4.14}$$

By taking the total derivative of (4.14), it follows

$$\dot{s} = -\frac{\ell}{q_1}\begin{bmatrix}\frac{r-q_2}{q_1} & 1\end{bmatrix}\begin{bmatrix}\dot{q}_1 \\ \dot{q}_2\end{bmatrix} + \frac{\ell}{q_1}\dot{r} =: f_S$$

From this equation, we can identify the matrices $A(q,r)$ and $B(q,r)$, i.e.,

$$A(q,r) = -\frac{\ell}{q_1}\begin{bmatrix}\frac{r-q_2}{q_1} & 1\end{bmatrix}, \quad B(q) = \frac{\ell}{q_1}$$

with which it is possible to build the skew-symmetric matrix $D(q,r)$ that represents the Dirac structure, as defined in (4.4).

The energy stored in the spring is given by the function $H(s) = \frac{1}{2}ks^2$, which, under the kinematic map $\lambda : (q,r) \mapsto s$ as given in (4.14), is equivalently given by

$$\bar{H}(q,r) = (H \circ \lambda)(q,r) = \frac{1}{2}k\left(\ell\,\frac{r-q_2}{q_1}\right)^2$$

The output force $e_I = F$ of the actuator is then given by

$$\begin{aligned} e_I = -B^T(q,r)\,e_S &= -\frac{\partial\lambda}{\partial r}\frac{\partial H}{\partial s} \\ &= -\frac{\partial\bar{H}}{\partial r} = -k\ell^2\frac{r-q_2}{q_1^2} \end{aligned}$$

Using the definition of the actuator output stiffness (4.3), we find that for this design the output stiffness K is given by

$$K = \frac{\partial F}{\partial r} = k\left(\frac{\ell}{q_1}\right)^2$$

Since only one spring is present, the tangent space $T_s\mathcal{S}$ is one-dimension. The image of $B(q,r)$ is given by

$$\text{im } B(q,r) = \text{span}\left\{\frac{1}{q_1}\right\}, \qquad \forall (q,r) \in \mathcal{Q}\times\mathcal{R}$$

and, therefore, it spans the complete tangent space $T_s\mathcal{S}$. It follows that the virtual storage element $\mathbb{C}^\perp$ has zero dimension, i.e., it does not appear in the diagram of Figure 4.4. Therefore, all the power P_C, supplied via the control port during any nominal behavior of the actuator, goes either to $\mathbb{C}^\parallel$ or to the output. This means that no power is lost, i.e., no energy is captured by the internal springs. This means that, for this principle design, the performance metric μ, as defined in (4.13), is

$$\mu = 0$$

This observation is in accordance with the static analysis presented in [29], where it was shown that the designs based on a lever arm are energy efficient in terms of changing the apparent output stiffness.

4.5.2 Design Based on an Antagonistic Spring Setup

Variable stiffness actuators, based on an antagonistic spring setup, have been proposed in different realizations, such as the AMASC [38], VSA [32], VSA-II [39]. In general, the designs use nonlinear springs, that act in opposite directions on the output. The internal degrees of freedom change the elongation of the springs, and, in this way, they indirectly change the actuator output position and the apparent output stiffness.

The conceptual design of an antagonistic variable stiffness actuator is depicted in Figure 4.6. The working principle is based on two identical nonlinear quadratic springs, characterized by elastic constant k. The springs are in series with two linear motors M_1 and M_2, which generate the two linear displacements q_1 and q_2, respectively. When the motors

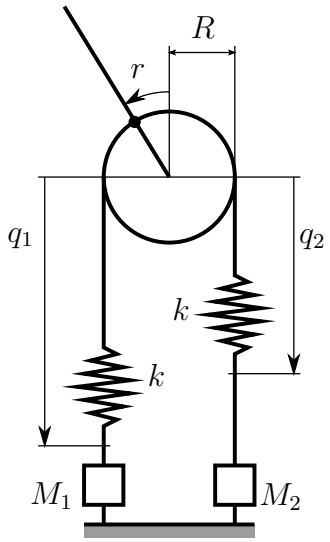

Figure 4.6: Variable stiffness actuator using an antagonistic spring setup - This design is based on two series elastic actuators in an antagonistic setup. The linear motors M_1 and M_2 generate linear displacements q_1 and q_2. The nonlinear quadratic springs have elastic constant k. By operating the motors in common mode, the apparent output stiffness of the actuator changes, while by operating the motors in differential mode the equilibrium of the actuator output position r changes [32].

are operated in common mode, the actuator output stiffness is changed. When the motors are operated in differential mode, the actuator output position r is changed.

In order to build the port-based model of this actuator design, we observe that the states $s_i > 0$, with $i = 1, 2$, of the nonlinear springs are given by

$$s = \begin{bmatrix} s_1 \\ s_2 \end{bmatrix} = \begin{bmatrix} q_1 - Rr \\ q_2 + Rr \end{bmatrix} \tag{4.15}$$

where R is the radius of the pulley and the restriction $s_i > 0$ is assumed to simplify the equations involving the force generated by the quadratic springs. By taking the total derivative of (4.15), we obtain

$$\dot{s} = \begin{bmatrix} \dot{s}_1 \\ \dot{s}_2 \end{bmatrix} = \begin{bmatrix} \dot{q}_1 - R\dot{r} \\ \dot{q}_2 + R\dot{r} \end{bmatrix} =: \begin{bmatrix} f_{S_1} \\ f_{S_2} \end{bmatrix}$$

From this, we can identify the matrices $A(q, r)$ and $B(q, r)$, i.e.,

$$A(q, r) = \begin{bmatrix} 1 & 0 \\ 0 & 1 \end{bmatrix}, \quad B(q, r) = \begin{bmatrix} -R \\ R \end{bmatrix}$$

with which it is possible to build the skew-symmetric matrix $D(q, r)$ that represents the Dirac structure, as defined in (4.4).

The total energy stored in the quadratic springs is $H(s_1, s_2) = \frac{1}{3}ks_1^3 + \frac{1}{3}ks_2^3$, which, under the kinematic map $\lambda : (q, r) \mapsto s$ as given in (4.15), is equivalently given by

$$\bar{H}(q, r) = (H \circ \lambda)(q, r) = \frac{1}{3}k\,(q_1 - Rr)^3 + \frac{1}{3}k\,(q_2 + Rr)^3$$

The output force $e_I = F$ of the actuator is given by

$$\begin{aligned} e_I &= -B^T(q,r)\, e_S = -\frac{\partial \lambda}{\partial r}\frac{\partial H}{\partial s} \\ &= -\frac{\partial \bar{H}}{\partial r} = kR\left(-(q_1 - Rr)^2 + (q_2 + Rr)^2\right) \end{aligned}$$

Using the definition of the actuator output stiffness (4.3), we find that the output stiffness K is given by

$$K = \frac{\partial F}{\partial r} = -2kR^2(q_1 + q_2)$$

As this design presents two springs, the tangent space $T_s\mathcal{S}$ is two-dimensional. Let the metric M be

$$M = \frac{\partial^2 H}{\partial s^2} = \begin{bmatrix} 2ks_1 & 0 \\ 0 & 2ks_2 \end{bmatrix}$$

The unit vector $b^{\|}$, computed with respect to the metric M such that $\|b^{\|}\|_M = 1$, is

$$b^{\|} = \frac{1}{\sqrt{2k(s_1 + s_2)}} \begin{bmatrix} -1 \\ 1 \end{bmatrix}$$

Using the constraints on the orthogonality, i.e. $\langle b^{\|}, b^{\perp} \rangle_M = 0$, the unit vector $b^{\perp}$, computed with respect to the metric M such that $\|b^{\perp}\|_M = 1$, is

$$b^{\perp} = \frac{1}{\sqrt{2k(s_1 + s_2)}} \begin{bmatrix} \sqrt{\frac{s_2}{s_1}} \\ \sqrt{\frac{s_1}{s_2}} \end{bmatrix}$$

The change of coordinates, as defined in (4.7), follows

$$S_b = \begin{bmatrix} b^{\|} & b^{\perp} \end{bmatrix} = \frac{1}{\sqrt{2k(s_1 + s_2)}} \begin{bmatrix} -1 & \sqrt{\frac{s_2}{s_1}} \\ 1 & \sqrt{\frac{s_1}{s_2}} \end{bmatrix}$$

In order to continue the power analysis presented in Section 4.3, we calculate

$$\begin{aligned} \begin{pmatrix} \dot{s}_q^{\|} \\ \dot{s}_q^{\perp} \end{pmatrix} &= S_b^{-1} A(q,r)\dot{q} \\ &= \frac{\sqrt{2k(s_1 + s_2)}}{s_1 + s_2} \begin{bmatrix} -s_1 & s_2 \\ \sqrt{s_1 s_2} & \sqrt{s_1 s_2} \end{bmatrix} \begin{bmatrix} 1 & 0 \\ 0 & 1 \end{bmatrix} \begin{bmatrix} \dot{q}_1 \\ \dot{q}_2 \end{bmatrix} \\ &= \frac{\sqrt{2k(s_1 + s_2)}}{s_1 + s_2} \begin{bmatrix} -s_1\dot{q}_1 + s_2\dot{q}_2 \\ \sqrt{s_1 s_2}(\dot{q}_1 + \dot{q}_2) \end{bmatrix} \end{aligned}$$

The quadratic spring generate forces $e_S = \mathrm{d}H = \frac{\partial H}{\partial s} = \begin{bmatrix} ks_1^2 & ks_2^2 \end{bmatrix}$, from which we obtain

$$\begin{aligned} \begin{pmatrix} \mathrm{d}H^{\|} & \mathrm{d}H^{\perp} \end{pmatrix} &= \mathrm{d}H\, S_b \\ &= \begin{bmatrix} ks_1^2 & ks_2^2 \end{bmatrix} \frac{1}{\sqrt{2k(s_1 + s_2)}} \begin{bmatrix} -1 & \sqrt{\frac{s_2}{s_1}} \\ 1 & \sqrt{\frac{s_1}{s_2}} \end{bmatrix} \\ &= \frac{1}{\sqrt{2k(s_1 + s_2)}} \begin{bmatrix} k\left(-s_1^2 + s_2^2\right) & k\left(\sqrt{s_1^3 s_2} + \sqrt{s_1 s_2^3}\right) \end{bmatrix} \end{aligned} \tag{4.16}$$

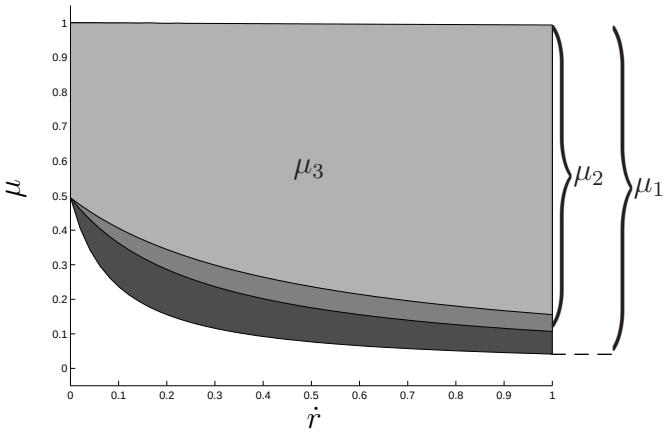

Figure 4.7: Performance metric for the design based on an antagonistic spring setup - The indicated areas μ_1, μ_2, μ_3 correspond to $\dot{K} = 0.2$, $\dot{K} = 0.6$ and $\dot{K} = 1.0$, respectively.

The performance metric μ, as defined in (4.13), is given by

$$\mu = \frac{P_C^{\perp}}{P_C} = \frac{\langle \mathrm{d}H^{\perp} | \dot{s}_q^{\perp} \rangle}{\langle \mathrm{d}H | A(q,r)\dot{q} \rangle}$$

The measure is visualized in Figure 4.7, where $\dot{q}$ has been chosen such to achieve the desired changes in position ($\dot{r}$) and stiffness ($\dot{K}$), as depicted in the figure. The areas indicate that, for a particular $(\dot{r}, \dot{K})$, the value of μ will be in the corresponding area. The actual value of μ depends on the load of the springs, i.e., (s_1, s_2), and it is negatively affected by higher preloads, which is in agreement with [29]. As an example, from (4.16), it can be seen that $P^{\parallel} = \langle \mathrm{d}H^{\parallel} | \dot{s}_q^{\parallel} \rangle = 0$ if $s_1 = s_2$, and hence, due to power continuity, $\mu = 1$. Finally, it can be noted that the performance deteriorates when the stiffness change is faster.

For this particular design principle, Remark 4.3.1 can be illustrated visually. In Figure 4.8, the surface represents the energy function $H(s) = \frac{1}{3}ks_1^3 + \frac{1}{3}ks_2^3$. The black curves represent the integral manifolds $\mathcal{S}_r$ of $B(q,r)\dot{r}$. Restricted to these foliations, $H(s)$ has a minimum indicated by the dashed line. Since the matrix $A(q,r)$ is full rank for this design, the integral manifold of $A(q,r)\dot{q}$ is in fact equal to $\mathcal{S}$. This means that, using the control input $\dot{q}$ with its corresponding control energy, it is possible to go from any configuration on $\mathcal{S}$ to any other configuration. However, through the output port, the configuration change is restricted to lie on the foliation $\mathcal{S}_r$ that has been reached. Therefore, the minimum energy level, that the system can reach, is in a local minimum of $H(s)$. This is illustrated via the solid black curve, which represents a generic change of configuration of the actuator. It can be seen that in general the energy, which has been supplied via the control port, cannot be provided completely to the output port. The actual amount of energy that is internally stored is equal to the difference in energy levels at the end points of the solid curve.

4.5.3 Design based on a Mechanical Decoupling

The variable stiffness actuator VSJ has been presented in [33], and the conceptual design is depicted in Figure 4.9. The working principle is based on two identical nonlinear quadratic springs, characterized by elastic constant k. In this design, the change of the

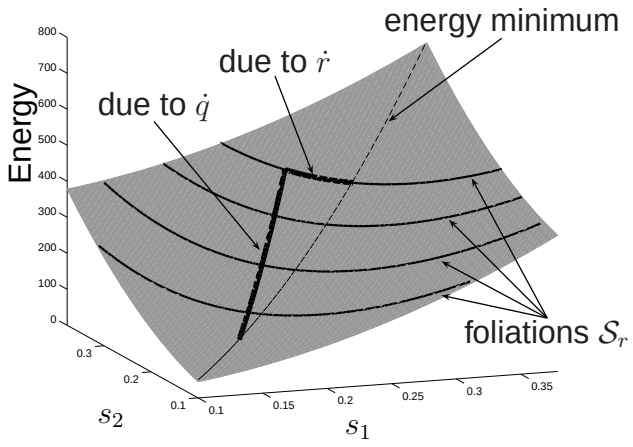

Figure 4.8: Energy function on $\mathcal{S}$ - Since the image of $A(q,r)$ spans the entire tangent space $T_s\mathcal{S}$, any arbitrary point $s \in \mathcal{S}$ can be reached by a proper $\dot{q}$. However, restricted to the foliations $\mathcal{S}_r$ (indicated by the black lines), only a local minimum of $H(s)$ can be reached (indicated by the dashed line). The difference in energy levels between the end points of the thick black curve indicates how much energy cannot be used to do work on the output.

stiffness and the output joint position is decoupled. The linear motor M_2 generates a linear displacement q_2 and is used for changing the apparent output stiffness of the actuator. The output position r is determined by the rotational motor M_1, which directly controls the degree of freedom q_1. Note that thus the end effector can rotate independently from the pulley. Compared with the antagonistic design presented in Section 4.5.2, the degree of freedom q_1 realizes the differential mode of operation of the motors M_1 and M_2 in the antagonistic design, and the degree of freedom q_2 the common mode operation.

In order to build the port-based model of this actuator design, we observe that the states $s_i > 0$, with $i = 1, 2$, of the nonlinear spring are given by

$$s = \begin{bmatrix} s_1 \\ s_2 \end{bmatrix} = \begin{bmatrix} q_2 - R\alpha \\ q_2 + R\alpha \end{bmatrix} \tag{4.17}$$

where R is the radius of the pulley, $\alpha = -q_1 + r + \frac{\pi}{2}$ and the restriction $s_i > 0$ is assumed to simplify the equations involving the force generated by the quadratic springs. By taking the total derivative of (4.17), we obtain

$$\dot{s} = \begin{bmatrix} \dot{s}_1 \\ \dot{s}_2 \end{bmatrix} = \begin{bmatrix} \dot{q}_2 + R\dot{q}_1 - R\dot{r} \\ \dot{q}_2 - R\dot{q}_1 + R\dot{r} \end{bmatrix} =: \begin{bmatrix} f_{S_1} \\ f_{S_2} \end{bmatrix}$$

From this, we identify the matrices $A(q,r)$ and $B(q,r)$, i.e.,

$$A(q,r) = \begin{bmatrix} R & 1 \\ -R & 1 \end{bmatrix}, \quad B(q,r) = \begin{bmatrix} -R \\ R \end{bmatrix}$$

with which the Dirac structure, as defined in (4.4), can be represented.

The total energy stored in the quadratic springs is $H(s_1, s_2) = \frac{1}{3}ks_1^3 + \frac{1}{3}ks_2^3$, which, under the kinematic map $\lambda : (q,r) \mapsto s$ as given in (4.17), is equivalently given by

$$\bar{H}(q,r) = (H \circ \lambda)(q,r) = \frac{1}{3}k\left(q_2 - R\alpha\right)^3 + \frac{1}{3}k\left(q_2 + R\alpha\right)^3$$

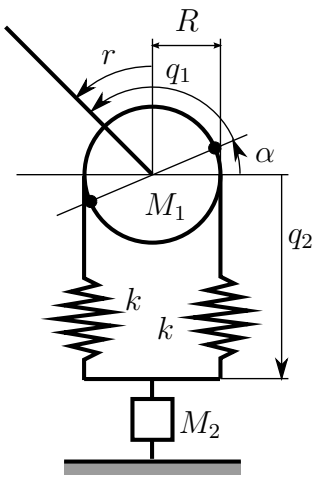

Figure 4.9: Variable stiffness actuator using an antagonistic spring configuration and based on mechanical decoupling - In this design, the change of the stiffness and the actuator output position r is decoupled. The linear motor M_2 generates a linear displacement q_2 and is used for changing the apparent output stiffness of the actuator. The output joint position r is determined by the rotational motor M_1 [33].

The output force $e_I = F$ of the actuator is given by

$$\begin{aligned} e_I &= -B^T(q,r)\, e_S = -\frac{\partial \lambda}{\partial r}\frac{\partial H}{\partial s} \\ &= -\frac{\partial \bar{H}}{\partial r} = kR\left(-\left(q_1 - R\alpha\right)^2 + \left(q_2 + R\alpha\right)^2\right) \end{aligned}$$

Using (4.3), we find for the actuator output stiffness

$$K = \frac{\partial F}{\partial r} = -4kR^2 q_2$$

The matrix $B(q,r)$ for this design is the same as for the previous design. Hence, the image is exactly the same, and the same change of coordinates S_b is obtained. We then have

$$\begin{aligned} \begin{pmatrix} \dot{s}_q^{\parallel} \\ \dot{s}_q^{\perp} \end{pmatrix} &= S_b^{-1} A(q,r)\dot{q} \\ &= \frac{\sqrt{2k(s_1+s_2)}}{s_1+s_2} \begin{bmatrix} -s_1 & s_2 \\ \sqrt{s_1 s_2} & \sqrt{s_1 s_2} \end{bmatrix} \begin{bmatrix} R & 1 \\ -R & 1 \end{bmatrix} \begin{bmatrix} \dot{q}_1 \\ \dot{q}_2 \end{bmatrix} \\ &= \frac{\sqrt{2k(s_1+s_2)}}{s_1+s_2} \begin{bmatrix} -R\dot{q}_1(s_1+s_2) - \dot{q}_2(s_1-s_2) \\ 2\sqrt{s_1 s_2}\dot{q}_2 \end{bmatrix} \end{aligned}$$

The forces $e_S = \mathrm{d}H = \frac{\partial H}{\partial s}$ is the same as in the antagonistic design, and hence we can compute μ according to (4.13)

$$\mu = \frac{P_C^{\perp}}{P_C} = \frac{\langle \mathrm{d}H^{\perp} | \dot{s}_q^{\perp} \rangle}{\langle \mathrm{d}H | A(q,r)\dot{q} \rangle}$$

Figure 4.10 presents a visualization of the metric, where $\dot{q}_1$ has been used to achieve the indicated $\dot{r}$, and $\dot{q}_2$ to achieve $\dot{K}$. The areas indicate that, for a particular $(\dot{r}, \dot{K})$, the value of

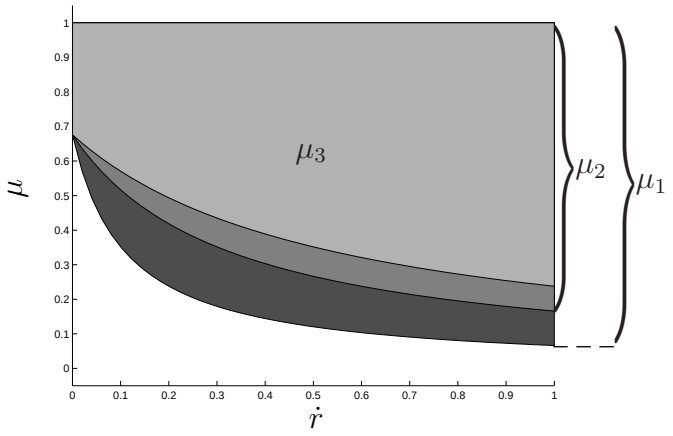

Figure 4.10: Performance metric for the design based on mechanical decoupling - The indicated areas μ_1, μ_2, μ_3 correspond to $\dot{K} = 0.2$, $\dot{K} = 0.6$ and $\dot{K} = 1.0$, respectively.

μ will be in the corresponding area. Also for this design, the actual value of μ depends on the load of the springs, i.e., (s_1, s_2), and it is negatively affected by higher preloads. As in the previous design, it can be noted that the performance deteriorates when the stiffness change is faster. However, because of the mechanical decoupling of the position and stiffness change, this influence is bigger than in the previous design.

4.6 Conclusions

In this Chapter, we defined a performance metric for variable stiffness actuators, derived using a port-based modeling framework. The performance metric is computed in dynamic conditions and determines how efficient the design is in transferring the power from the internal degrees of freedom to the output, irrespectively of the dynamic behavior of the load. We showed in three different principle designs that the performance measure is strictly related to the kinematic properties of the actuator.

It was observed that pretension of internal springs has a negative influence on the performance measure. This can be explained by observing the relation between the output motion and the state of the internal springs. We have shown that this effect becomes more prominent when the rate of change of the stiffness increases.

It can be concluded that a good design of variable stiffness actuators, in terms of energy efficiency, should incorporate a variable transmission ratio between the output and the internal springs. If such a design is not available, a proper control of $\dot{r}$ and $\dot{K}$ should be designed in order to achieve a certain behavior and to realize energy efficiency.

Chapter 5

Energy Efficient Control of Oscillatory Motions

The goal of this Chapter is to show how variable stiffness actuators can be used to achieve energy efficient control of locomotion systems. Two approaches are given. In the first approach, presented in Section 5.1, the analysis results of the port-based model are used to allow a variable stiffness actuator to store and reuse disturbance energy. In the second approach, discussed in Section 5.2, the stiffness of the variable stiffness actuator is dynamically tuned with the aim of matching the natural frequency of the actuated system to the desired motion.

5.1 Energy Efficient Control by Storing Disturbance Energy

In this Section, we give an approach for energy efficient control of robotic systems under the influence of disturbances [40].

5.1.1 Introduction

The port-based framework not only provides valuable insights on energy flows between the internal actuators, the springs and the robot, but it is also a solid foundation for research on innovative control methods. With the aim of achieving energy efficiency, we derive a control architecture that uses the potential energy stored in the springs to actuate the robot, instead of supplying this energy by controlling the internal degrees of freedom. We demonstrate the effectiveness of the proposed controller for a one degree of freedom system, under influence of a disturbance. In particular, if a disturbance occurs, the corresponding energy is stored in the internal springs and used for actuation. The insights gained will form a basis for future work, in which we aim to develop energy efficient coordinated control methods for a robot with multiple degrees of freedom [40].

In this Section, we provide a generalization of the explicit formulation of the previous Section. By this, we mean that we analyze the behavior of variable stiffness actuators on an abstract geometric level. As explained in the previous Section, there exists a map:

$$\Lambda_{(q,r)} : \mathcal{Q} \times \mathcal{R} \rightarrow \mathcal{S}$$

that defines how the configuration of the internal degrees of freedom $q \in \mathcal{Q}$ and the output position $r \in \mathcal{R}$ determine the states $s \in \mathcal{S}$ of the springs. The tangent map $\Lambda_{(q,r)*} : T\mathcal{Q} \times T\mathcal{R} \to T\mathcal{S}$ and cotangent map $\Lambda^*_{(q,r)} : T^*\mathcal{S} \to T^*\mathcal{Q} \times T^*\mathcal{R}$ are naturally defined [34]. The fiber bundle $\pi_u : \mathcal{U}_q \times \mathcal{U}_r \to \mathcal{Q} \times \mathcal{R}$ has fibers $\pi_u^{-1}(q, r)$ that denote the input spaces $U_q \times U_r$. Given an input $(u_q, u_r) \in U_q \times U_r$, the internal configuration q and the output position r are subject to the dynamics $G : \mathcal{U}_q \times \mathcal{U}_r \to T\mathcal{Q} \times T\mathcal{R}$ given by

$$\dot{q} = u_q, \quad \dot{r} = u_r \tag{5.1}$$

Equation (5.1) can be written as

$$\dot{q} = \sum_{i=1}^{n} v_{q,i} u_{q,i}, \quad \dot{r} = v_r u_r \tag{5.2}$$

where

$$\begin{aligned} v_{q,i} &= (\underbrace{0 \ \cdots \ 0}_{i-1 \text{ elements}} \ 1 \ \underbrace{0 \ \cdots \ 0}_{n-i \text{ elements}})^T \\ v_r &= 1 \end{aligned} \tag{5.3}$$

define constant input vector fields on $T\mathcal{Q} \times T\mathcal{R}$, i.e. the canonical basis for the tangent space. Since these dynamics are trivial, we allow abuse of notation and consider $\dot{q}$ and $\dot{r}$ as inputs to the system. These relations are summarized in the commutative diagram in Figure 5.1.

The dynamics of the variable stiffness actuator are

$$\begin{aligned} \dot{s} &= \Lambda_{(q,r)*} \ (\dot{q}, \dot{r}) \\ (\tau, F) &= \Lambda^*_{(q,r)} \ (\mathbf{d}H) \end{aligned} \tag{5.4}$$

where $\mathbf{d}H$ denotes the differential of the energy function H. We can see that flows are elements of the tangent spaces and efforts elements of the cotangent spaces. The Dirac structure, which is explicitly given in (3.15), is in the tangent maps $\Lambda_{q*} : T\mathcal{Q} \to T\mathcal{S}$, $\Lambda_{r*} : T\mathcal{R} \to T\mathcal{S}$ and the corresponding cotangent maps Λ^*_q, Λ^*_r. Via these maps, the velocities on $T_s\mathcal{S}$ at $s \in \mathcal{S}$ are defined by the velocities on $T_q\mathcal{Q} \times T_r\mathcal{R}$ at $(q, r) \in \mathcal{Q} \times \mathcal{R}$, and correspondingly the forces on $T^*_q\mathcal{Q} \times T^*_r\mathcal{R}$ by the forces on $T^*_s\mathcal{S}$, such that power continuity is preserved.

The rate of change of the energy stored in the springs is given by [41]:

$$\dot{H} = \mathbf{d}H \ \dot{s} = \mathbf{d}H \ \Lambda_{(q,r)*}(\dot{q}, \dot{r}) \tag{5.5}$$

From (5.4) and (5.5), it can be immediately observed how the output force and the energy stored in the mechanism are related to each other, and how the rate of change of the stored energy depends on the output ports. In particular, from (5.5) it follows that the energy stored in the springs does not change due to the control input if

$$\dot{q} \in \ker \Lambda_{q*} \tag{5.6}$$

where $\ker \Lambda_{q*}$ denotes the kernel of the map Λ_{q*}. Note that the existence of this kernel depends on the mechanical design of the variable stiffness actuator [28].

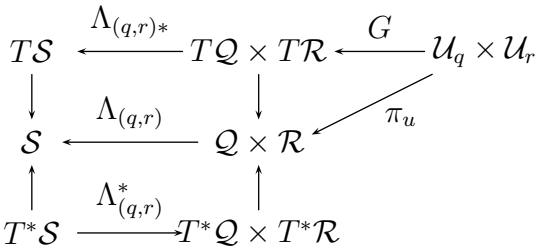

Figure 5.1: Commutative diagram for a variable stiffness actuator. $\mathcal{Q}$ is the configuration manifold of the internal degrees of freedom, $\mathcal{S}$ of the state of the internal springs, and $\mathcal{R}$ of the output position.

5.1.2 Energy Efficient Control

In this Section, an energy efficient control law for variable stiffness actuators is derived. This means that, in order to achieve the energy efficiency of the controller, we intend to use the energy stored in the internal springs, if present, for the actuation of the robotic joint. First, we formulate the problem statements and, then, derive a solution that accomplishes the energy efficiency requirements. Moreover, since the fundamental demand of variable stiffness actuators is the capability of changing the output stiffness, we extend the control law with stiffness regulation.

Problem Statement

As depicted in Figure 3.5, the variable stiffness actuator is connected to a robotic joint with one degree of freedom. This connection is explicitly shown in Figure 5.2 by a 1-junction representing the power continuous connection

$$\dot{r} = y, \quad u = -F$$

where (u, y) is the *interaction port* of the joint. In particular, u denotes the input force (or torque) applied to the joint, and y its velocity. We assume that full state measurement is available, i.e. for both joint and variable stiffness actuator all positions and velocities can be measured.

We now design an energetically efficient control architecture for the variable stiffness actuator, by using both the internal springs and internal actuated degrees of freedom, so that the actuator is able to apply a desired force (or torque) u_d to the joint and so that the output stiffness is regulated at a desired value. These goals are formally contained in the following problem statements.

Problem 5.1.1 *Consider a variable stiffness actuator, described by an energy function H and the dynamics (5.4), connected to a robotic joint by a power continuous connection. Assume that full state measurement is available. How can the control inputs $\dot{q}$ to the variable stiffness actuator be designed such that the desired joint input u_d is achieved in an energy efficient way?*

Problem 5.1.2 *How can the control inputs $\dot{q}$ to the variable stiffness actuator be designed such that a desired joint input u_d is achieved in an energy efficient way, while at the same time the output stiffness is controlled?*

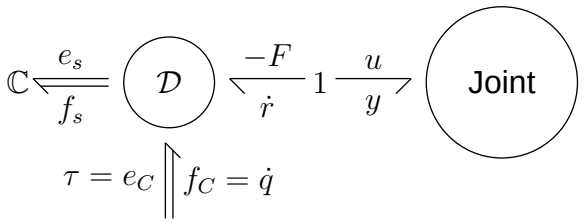

Figure 5.2: Generalized representation of a variable stiffness actuator interconnected with a robotic joint.

In the solutions of these two problems, we aim to exploit the internal springs of the variable stiffness actuator as buffers for storing potential energy and to use this energy to actuate the joint. In the remainder of the Section, we first derive a control law that solves Problem 5.1.1 in a nominal case, i.e., without considering energy efficiency. Then, we focus on refining the control law by efficiently using any potential energy stored in the springs to reduce the energy supply via the control port. Finally, we derive the stiffness control law for Problem 5.1.2.

Output Force Control

Before proceeding with the formulation of the control law, it is necessary to highlight that, if a desired input force (torque) u_d is required at the robotic joint, also the desired output force F_d of the actuator is known due to the power continuous connection. Moreover, from (5.4), the output force F, generated by the variable stiffness actuator, can be determined once the current values for q and x are given. This means that it is possible to find a control law $g_F(\cdot)$ such that the evolution in time of the force F is given by

$$\dot{F} = g_F(F_d, F)$$

as a function of the actual and the desired output force. We can then formulate a nominal control law as follows.

Lemma 5.1.3 (Nominal control) *Consider a variable stiffness actuator described by an energy function H and the dynamics (5.4), connected to the joint of a robot through a power continuous connection. Let the vector valued function $V(q, r)$ be:*

$$V(q, r) := (L_{v_{q,1}} F, \ldots, L_{v_{q,n}} F) \tag{5.7}$$

where $L_{v_{q,i}} F$ denotes the Lie-derivative of F along the vector field $v_{q,i}$. Define a subset $\mathcal{M}$ of $\mathcal{Q} \times \mathcal{R}$ as:

$$\mathcal{M} = \{(q, r) \in \mathcal{Q} \times \mathcal{R} \mid V(q, r) \neq 0\}$$

By using the control law $\dot{F} = g_F(F_d, F)$, the nominal control input

$$\dot{q}_n = V^+ \left(\dot{F} - (L_{v_r} F)\, \dot{r} \right) \tag{5.8}$$

where $^+$ denotes the Moore-Penrose pseudo inverse, solves Problem 5.1.1 for (q, r) in $\mathcal{M}$. $\diamond$

Proof: Since we defined the exact one-form $\mathrm{d}H$ on $T_s^*\mathcal{S}$, we have that (τ, F) is an exact one-form on $T_q^*\mathcal{Q} \times T_x^*\mathcal{R}$, defined by the map $\Lambda_{(q,r)}^*$ [34]. Moreover, since the input vector fields, as defined in (5.2) and (5.3) are constant, the rate of change of the one-form (τ, F) is given by

$$\frac{\mathrm{d}}{\mathrm{d}t}(\tau, F) = \begin{pmatrix} \dot{q}_1 & \cdots & \dot{q}_n & \dot{r} \end{pmatrix} \begin{pmatrix} L_{v_{q,1}}(\tau, F) \\ \vdots \\ L_{v_{q,n}}(\tau, F) \\ L_{v_r}(\tau, F) \end{pmatrix} \tag{5.9}$$

where we allowed some abuse of notation, as in (5.1). Since dim $\mathcal{X} = 1$, from (5.9) it follows that:

$$\dot{F} = V\dot{q} + (L_{v_r}F)\,\dot{r} \tag{5.10}$$

with V given in (5.7). Finally, from (5.10), the nominal controller $\dot{q}_n$ in (5.8) follows.

Note that the restriction of the solution to $\mathcal{M}$ follows from the Moore-Penrose pseudo inverse for the full row-rank matrix V [42]:

$$V^+ = V^T \left(VV^T\right)^{-1}$$

i.e., the pseudo inverse is only defined for (q, r) in $\mathcal{M}$. □

Energy Efficient Control

The solution derived in Lemma 5.1.3 is not energy efficient, since the energy stored in the springs is not taken into account. If a disturbance is present on the output port, we intend to direct the corresponding energy to the springs so to use them as energy buffer. Since our goal is to obtain solutions that efficiently use energy stored in the springs, if there is energy stored in the springs, there is, in general, no need to supply more energy via the control port.

For a particular class of variable stiffness actuators, the solution (5.8) can be modified such that any potential energy stored in the springs is efficiently used to actuate the robot. This class of actuators has the property that output position and output stiffness are decoupled on a mechanical level and, therefore, the kernel in (5.6) exists. This means that the map Λ_{q*} is surjective onto $T_s\mathcal{S}$:

$$\text{rank } \Lambda_{q*} < n, \quad \forall (q, r) \in \mathcal{Q} \times \mathcal{R}$$

This property allows for a partitioning of the tangent space $T_q\mathcal{Q}$, i.e. the tangent space to $\mathcal{Q}$ at q, as:

$$T_q\mathcal{Q} = \ker \Lambda_{q*} \oplus D$$

where $\oplus$ is the direct sum and D is such that the tangent space $T_q\mathcal{Q}$ is complete. In particular, since $T_q\mathcal{Q}$ is a $\mathbb{R}$-vector space [41], we require D to be orthogonal to $\ker \Lambda_{q*}$ in the Euclidean sense. If we denote by k the dimension of $\ker \Lambda_{q*}$, i.e.
dim $\ker T_q\mathcal{Q} = k$, $1 \leq k < n$, and since dim $T_q\mathcal{Q} = n$, it follows that dim $D = n - k$.

From (5.6) it was observed that, if the control input $\dot{q} \in \ker \Lambda_{q*}$, then the energy stored in the springs does not change due to the control input. Hence, the solutions to Problem 5.1.1 given by (5.8) should be in $\ker \Lambda_{q*}$ or close to it when energy is stored in the springs. This can be achieved by defining on $T_q\mathcal{Q}$ an appropriate metric that weights the solutions given by the Moore-Penrose pseudo inverse [42]. This argument is formalized in the following Lemma.

Lemma 5.1.4 (Energy efficient control) *Consider a variable stiffness actuator described by an energy function H and the dynamics (5.4) and connected to the joint of a robot by a power continuous connection. Assume that the variable stiffness actuator satisfies the property*

$$\textit{dim } \ker \Lambda_{q*} = k, \quad 1 \leq k < n, \quad \forall (q, r) \in \mathcal{Q} \times \mathcal{R}$$

Take on $T_q\mathcal{Q}$ two sets of local coordinates, orthogonal in the Euclidean sense, denoted by $a^1 = (a^1_1, \ldots, a^1_k)$ and $a^2 = (a^2_1, \ldots, a^2_{n-k})$, satisfying

$$\begin{aligned} \ker \Lambda_{q*} &= \textit{span}\left\{a^1\right\} \\ D &= \textit{span}\left\{a^2\right\} \end{aligned} \tag{5.11}$$

On $T_q\mathcal{Q}$, define a metric $\mathfrak{g}$, such that in the local coordinates (a^1, a^2) its components $[\mathfrak{g}]$ are given by

$$[\mathfrak{g}] = \begin{bmatrix} I_k & 0 \\ 0 & \alpha\, I_{n-k} \end{bmatrix} \tag{5.12}$$

with I_k and I_{n-k} the identity matrix of dimension k and $n-k$ respectively, and $\alpha : \mathcal{S} \to \mathbb{R}^+$ a positive definite function realizing a measure for the amount of energy stored in the springs.

Then, for (q, r) in the subset $\mathcal{M}$, the control input

$$\dot{q}_e = V^\sharp \left(\dot{F} - (L_{v_r} F)\, \dot{r} \right) \tag{5.13}$$

where $^\sharp$ denotes the Moore-Penrose pseudo inverse with respect to the metric $\mathfrak{g}$ defined in (5.12), solves Problem 5.1.1 in an energy efficient way by exploiting the energy stored in the springs. ◇

Proof: Using the partitioning (5.11), the solution (5.8) can be expressed into components that are either in $\ker \Lambda_{q*}$ or outside, i.e. in D. Figure 5.3 depicts a two dimensional example, in which $\left(\frac{\partial}{\partial q_1}, \frac{\partial}{\partial q_2}\right)$ denotes the canonical basis for $T_q\mathcal{Q}$, the one-dimensional spaces $\ker \Lambda_{q*}$ and D are spanned by the vectors a^1 and a^2, respectively. By choosing the metric $\mathfrak{g}$ as proposed in (5.12), the components of the solution $\dot{q}_e$ in D are weighted by α. In particular, since α is chosen such that it is proportional to the energy stored in the springs, the component in D is smaller when there is more energy available in the springs. Hence, from (5.5) it follows that, when there is more energy available in the springs, less energy is supplied via the control port. □

Stiffness Control

The control law derived in Lemma 5.1.4 achieves control of the joint position, but does not control the apparent stiffness of the joint. However, in many applications it is desired that the apparent joint stiffness attains some specific value. Therefore, we extend the control law with stiffness control. In particular, because of the redundancy in the internal degrees of freedom, we can define a control input, to add to any solution of Problem 5.1.1, so that the stiffness is controlled independently from the generated output force. This requires that the additional stiffness control $\dot{q}_{kV} \in \ker V$, so to not affect the control $\dot{q}_e$ in (5.13).

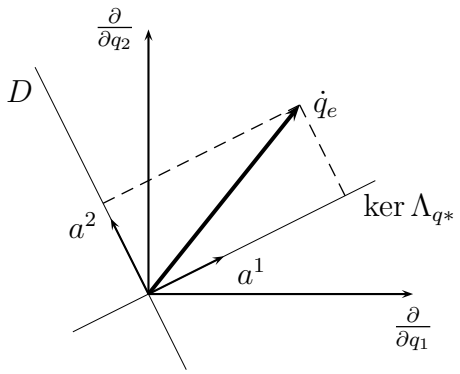

Figure 5.3: Decomposition of the energy efficient control law $\dot{q}_e$ in (5.13) into components in $\ker \Lambda_{q*}$ and in D.

Under the assumption of full state measurement, the apparent output stiffness K of the actuator may be estimated. Given a desired output stiffness K_d, we can design a control law $g_K(\cdot)$ such that the desired rate of change of the stiffness is given by

$$\dot{K} = g_K(K_d, K)$$

If we model the stiffness K as a function on the configuration manifold, i.e. $K : \mathcal{Q} \times \mathcal{X} \to \mathbb{R}$, we can formulate a control law for the stiffness as follows.

Lemma 5.1.5 (Stiffness control) *Define on $T_q\mathcal{Q}$ two sets of coordinates, denoted by b^1 and b^2, satisfying:*

$$\ker V = \textit{span}\left\{b^1\right\}$$
$$T_q\mathcal{Q} = \textit{span}\left\{b^1, b^2\right\}$$

Determine a solution $\dot{q}_k$ that achieves the desired rate of change of the stiffness, i.e. a solution satisfying

$$\begin{pmatrix} L_{v_{q,1}}K & \cdots & L_{v_{q,n}}K \end{pmatrix} \dot{q}_k = g_K(K_d, K)$$

where $L_{v_{q,i}}K$ denotes the Lie-derivative of K along $v_{q,i}$. Denote by $\dot{q}_{kV}$ the projection of $\dot{q}_k$ onto b^1. Then, the solution to Problem 5.1.2 is given by the control input

$$\dot{q}_k = \dot{q}_e + \dot{q}_{kV} \tag{5.14}$$

◇

Proof: The control input $\dot{q}_k$ is chosen such that the stiffness changes as desired, and by taking the projection onto $\ker V$, the stiffness is changed while Problem 5.1.1 is still solved. □

Remark 5.1.6 By taking the projection onto $\ker V$, it is ensured that at all times Problem 5.1.1 is solved. However, it follows that, in general, $\dot{q}_{kV} \neq \dot{q}_k$, and thus that the stiffness does not change exactly as desired, but as close to desired as possible. ◁

Remark 5.1.7 Since $\dot{q}_{kV}$ was not obtained with respect to the metric $\mathfrak{g}$ as defined in Lemma 5.1.4, the solution (5.14) is not necessarily energy efficient. In particular, the choice of $g_K(\cdot)$ determines the component outside $\ker \Lambda_{q*}$. ◁

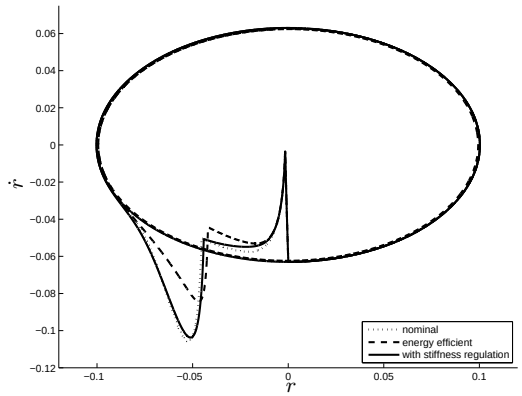

Figure 5.4: Joint phase diagram - In a periodic motion, the disturbance is similarly corrected by each control law.

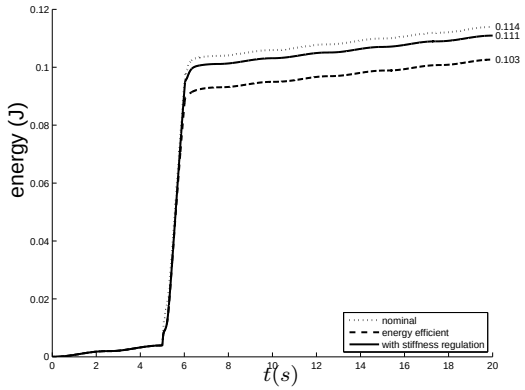

Figure 5.5: Energy supplied via the control port - The energy efficient control law clearly achieves a reduction in supplied energy. However, when stiffness regulation is added, some of the gain in efficiency is lost.

5.1.3 Simulation Results

In this Section, we show the effectiveness of the control law derived in Section 5.1.2. This will be done by using a linear variable stiffness actuator design, presented in earlier work [28], which satisfies the condition stated in Lemma 5.1.4, to actuate a joint. The experiment is as follows. The actuator moves a linear joint on a periodic motion following a sinusoidal trajectory with an amplitude of 10 cm at a frequency of 0.1 Hz. The force u_d needed to make the joint follow the trajectory is calculated using a PD-control law using the current and desired position and velocity. In the time interval $5 \leq t \leq 6$ s, the joint is subjected to a 2 N constant disturbance force. The same experiment is performed with each of the three presented control laws (5.8), (5.13), (5.14), and their performance is compared. In particular, it is investigated how each of the controllers handles the disturbance energy. The results are presented in Figures 5.4-5.6.

Figure 5.4 shows the phase space trajectory of the joint. It can be seen that the response to the disturbance is similar for each of the controllers. Note that each controller required approximately the same amount of time to return to the desired trajectory. In Figure 5.5, the energy supplied via the control port of the variable stiffness actuator is plotted. In particular, the absolute power flow through the control port is integrated, to make explicit that negative

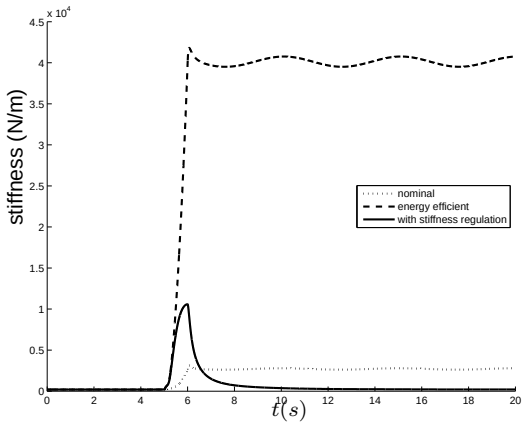

Figure 5.6: Output stiffness - Adding stiffness regulation to the control law ensures that the stiffness of the joint is kept close to a desired value of 200 N/m.

work is lost. From the numerical values, it can be seen that the energy efficient control law indeed achieves a significant reduction in energy consumption (approximately 9.6% with respect to the nominal control law). When stiffness regulation is added, the reduction in energy consumption is less (approximately 2.6%), as was expected. From Figure 5.6, the added benefit of stiffness regulation can be seen. Initially, the output stiffness is kept to a desired value of 200 N/m. When the disturbance occurs, the output stiffness increases, because the internal springs store the disturbance energy. The increase in stiffness might be an undesirable side effect in some applications, e.g. in human-robot interaction, and thus the potential benefit of adding stiffness regulation is illustrated. However, at the same time, it is illustrated that energy efficient control and regulating stiffness are contradicting goals.

5.1.4 Conclusions and Future Work

In this Chapter, we presented an energy efficient control method for variable stiffness actuators. In addition, a stiffness regulation control was implemented, with the aim of maintaining a desired output stiffness. Simulation results illustrate the effectiveness of the proposed method. In particular, it was shown that the energy efficient control law indeed achieves a significant reduction in the energy supplied via the control port of the variable stiffness actuator by reusing energy stored in the springs. Adding stiffness regulation reduces the energy efficiency, but the controller still performs better than the nominal controller. It was found that the strict time dependency of the reference trajectory in the simulation can sometimes cause the controllers to perform poorly. This is due to the inherent oscillatory behaviour of the springs. We believe that, in limit cycle trajectory tracking applications, the advantages of the proposed control strategy will become more apparent. Since in such trajectory tracking application time is no longer restrictive, the controller may perform better by taking a state dependent response to the disturbance.

Future work will focus on controlling multiple degree of freedom systems under influence of significant disturbances, where the energy storing capabilities of the springs are more useful. The aim is to control the joints in a coordinated way, and come to an energy efficient disturbance correction. In particular, in the control of walking robots, the energy losses, associated with the impacts of the feet, can be reduced using our proposed control method.

5.2 Energy Efficient Control by Stiffness Tuning

In this Section, it is shown how tuning the joint stiffness is beneficial to energy efficient actuation of oscillatory motions, if the stiffness change itself is energy efficient.

5.2.1 Introduction

In bipedal locomotion, the forward velocity is directly related to the gait frequency [43, 44, 45]. It has been shown that matching the natural frequency of the joints to the frequency of the desired motion can reduce the energy consumption [46, 47, 48]. The natural frequency of the joint and the connected link is a function of the joint stiffness and the link inertia, and thus, to match the motion frequency and minimize energy consumption, the robot needs to have the ability to change the joint stiffness. This can be achieved with variable compliance actuators.

It is often underestimated that the stiffness regulation itself requires additional energy, which in the case of continuous regulation due the varying frequency of the locomotion gait, can lead to increased energy consumption. In other words, if the required energy to change the stiffness is considerably high, then changing the stiffness in order to fit the natural frequency to the motion frequency would not be energetically valuable.

Looking at the different variable stiffness actuators in most of the implementations, the mechanism which changes the stiffness requires substantial amount of energy, for instance in antagonistic setups [32, 49, 39, 50, 51], and series setups, in which the stiffness tuning is based on the pretension of the elastic element [33, 52, 53, 54, 55, 56]. In particular, in antagonistic setups, two actuators (each one in series with an elastic element with a nonlinear force to deflection behavior) change the output position and stiffness. Changing the position is done by co-rotation of the actuators, while tuning the stiffness is based on their relative motion: counter-rotation of the actuators in one direction makes the joint more compliant, and counter-rotation in the other direction makes it stiffer. As in these setups both actuators are directly counteracting against each other and the elastic element, substantial effort and therefore energy is required to change the stiffness.

In the stiffness regulation principle of the series implementations, one motor is used to change the output position, and a second motor to change the stiffness by setting the pretension of an elastic element connected to the output. In these setups, the motor that tunes the stiffness directly counteracts with the spring force, which again requires substantial energy.

In [45], it is suggested to keep the stiffness fixed and not to change it during a certain repetitive motion due to high cost of energy to change the stiffness.

A solution to cope with the energy cost of the stiffness regulation is a mechanism in which the stiffness motor does not need to directly counteract the total spring force during the stiffness tuning. The Actuator with Adjustable Stiffness (AwAS I and II) [36, 57, 58] can tune the stiffness with minimal energetic cost. The novelty of the proposed design with respect to the existing systems is the principle used to regulate the compliance. This is done not through the tuning of the pretension of the elastic element, but by controlling the location of the elastic elements (springs) using the variable lever arm principle. An important consequence of this approach is that the displacement needed to change the stiffness is perpendicular to the forces generated by the springs, thus this helps to minimize the energy/power required to tune the stiffness.

This Section demonstrates this capability of AwAS to change the stiffness with low energy cost, and how this property can be used to reduce the energy consumption while tracking periodic motion profiles of fixed and variable frequency.

5.2.2 Dynamic Model of AwAS

AwAS can be physically modeled as a system consisting of two masses, connected by a spring with variable stiffness, a shown in Figure 5.7. The masses represent the inertia of the internal motors and the inertia of the output link plus load respectively. The dynamics can be formulated as:

$$\begin{cases} I_M\ddot{\theta} + B_M\dot{\theta} + K(\theta - q) = T_M \\ (I_L + ML^2)\ddot{q} + B_L\dot{q} + K(q - \theta) = T_L \end{cases} \tag{5.15}$$

where I_M and I_L denote the motor inertia (including gearbox) and output link inertia respectively. The coefficients B_M and B_L denote motor side and output friction. The output position is denoted by θ, and the motor position (after the gearbox) is denoted by q. The torques T_M and T_L denote motor torque and output torque. The load has mass M and is mounted at a distance L of the joint rotation. K denotes the joint stiffness. The damping at the output link side is minimum (as it rotates on low friction ball bearings) and can be neglected ($B_L = 0$). To eliminate the effect of gravity ($T_L = 0$), the actuator is fixed parallel to the horizontal plane during the experiment, as shown in Figure 5.8.

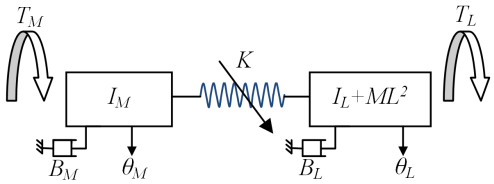

Figure 5.7: Physical model of AwAS.

From the link torque equilibrium equation of (5.15), the trajectory of the internal motor can be found as:

$$\theta = \frac{I_M + ML^2}{K}\ddot{q} + q \tag{5.16}$$

The natural frequency f_n of such a system is:

$$f_n = \frac{1}{2\pi}\sqrt{\frac{K}{I_M + ML^2}}$$

5.2.3 Experimental Validation

In the first step of this experiment, the link is asked to perform a sinusoidal trajectory:

$$q = A\sin 2\pi f t \tag{5.17}$$

with amplitude $A = 0.2$ rad and a fixed frequency of $f = 2.5$ Hz. The relevant parameters of the experimental setup presented in Figure 5.8 are shown in Table 5.1.

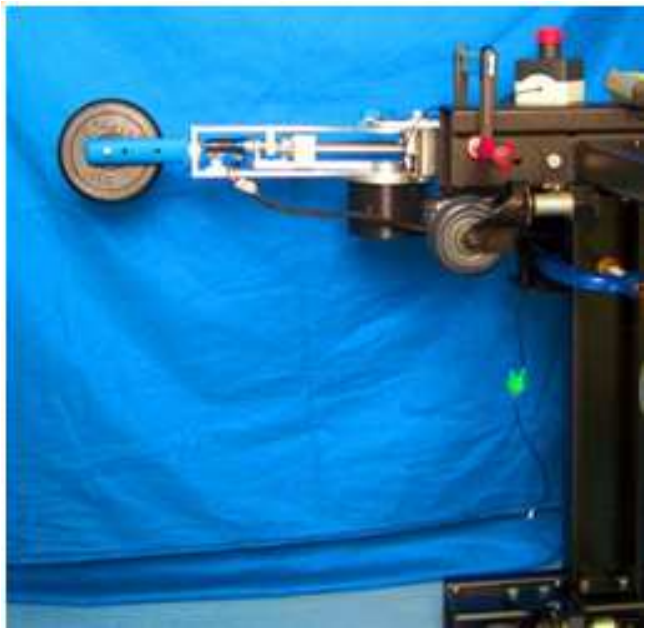

Figure 5.8: Experimental setup. AwAS is fixed horizontally and a ‘ kg mass is attached at the end of the link.

Parameter	Value
I_M	0.35 Nms^2/rad
I_L	0.1 Nms^2/rad
M	1 kg
L	0.34 m

Table 5.1: Parameters of the experimental setup

Using (5.17), the stiffness corresponding to the frequency of the desired motion can be calculated as:

$$K = 4\pi^2 f_n^2 (I_L + ML^2) = 51.8 \text{ Nm/rad}$$

We experimentally verify this, by setting the level of the stiffness to this value. Oscillations were then manually triggered at the output link by pulling the output link out of its equilibrium position and then releasing it. As a result, the output link starts oscillating around the equilibrium position at its natural frequency. Figure 5.9 presents the output link position showing a natural frequency of 2.5 Hz, as expected from (5.17) for the preset stiffness of 51 Nm/rad.

Following this, the level of stiffness was set to different values from 30 Nm/rad to 70 Nm/rad, and the energy consumption of AwAS to perform one complete cycle was measured for each of these levels of stiffness. As expected, Figure 5.10 shows that the minimum energy consumption occurs when stiffness is close to the natural frequency of the joint, near 50 Nm/rad, demonstrating how by exploiting natural dynamics of the output link the energy consumption can be minimized.

The experimental trajectories of the output link and of the motor, for three level of stiffness, are shown in Figure 5.11. It can be observed that the amplitude of the trajectory of the motor is minimized when the natural dynamics of the link is exploited. This also can

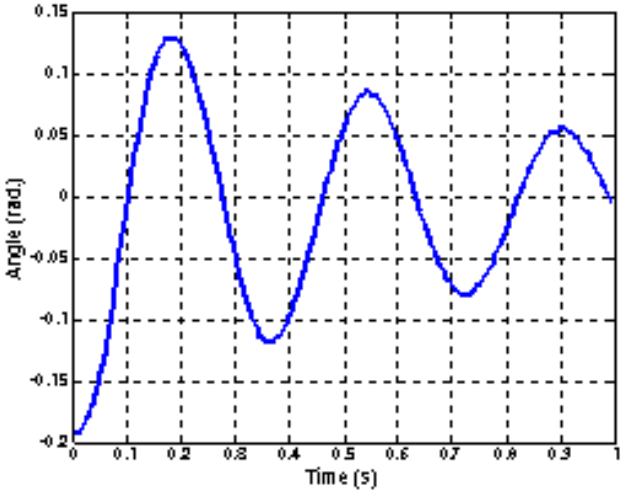

Figure 5.9: Oscillation showing the natural frequency of the link when the joint stiffness is set to 51 Nm/rad.

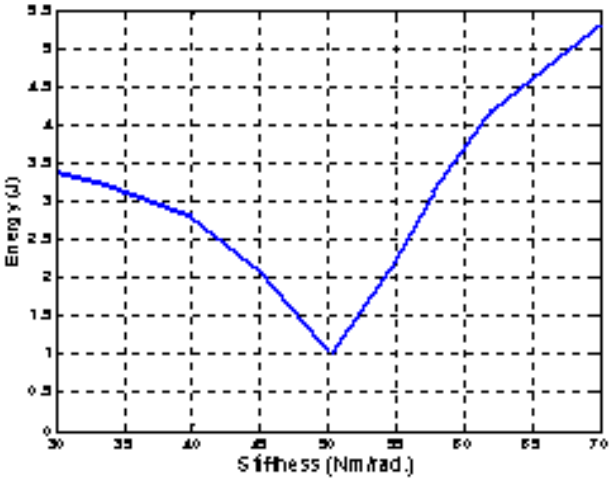

Figure 5.10: Energy consumption of AwAS for different levels of stiffness.

be observed from (5.16), for the frequency equal to the natural frequency:

$$\theta = \left(1 - \frac{I_L + ML^2}{K} 4\pi^2 f_n^2\right) q = 0 \tag{5.18}$$

Following this, a varying frequency sinusoidal trajectory was used as the reference position for the output link. As shown in Figure 5.12, the frequency of the sinusoidal reference signal starts at 3 Hz and smoothly decreases to 2 Hz within a time interval of 10 seconds.

To minimize the energy required while tracking the reference trajectory, two stiffness regulation strategies were considered and evaluated. In the first approach, the stiffness is kept fixed during the whole duration of the motion. The energy consumption of AwAS to execute the reference trajectory was measured for different levels of stiffness and a fixed optimum value for the stiffness for this particular motion profile was found. In the second strategy, the stiffness was continuously tuned based on the varying frequency of the reference trajectory, in such a way that the natural dynamics of the output link was

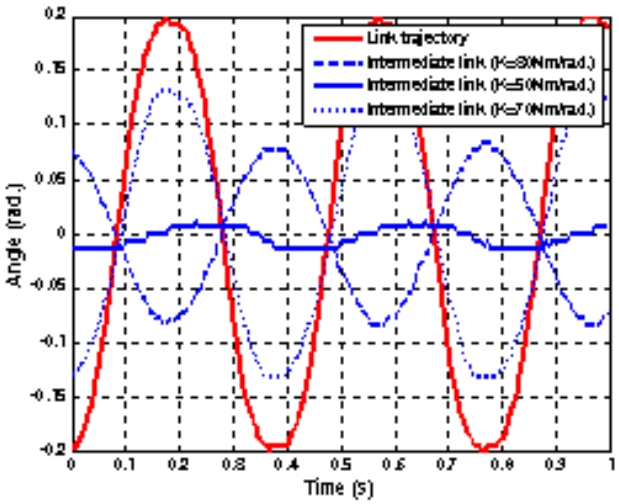

Figure 5.11: Link and motor trajectories for different level of stiffness.

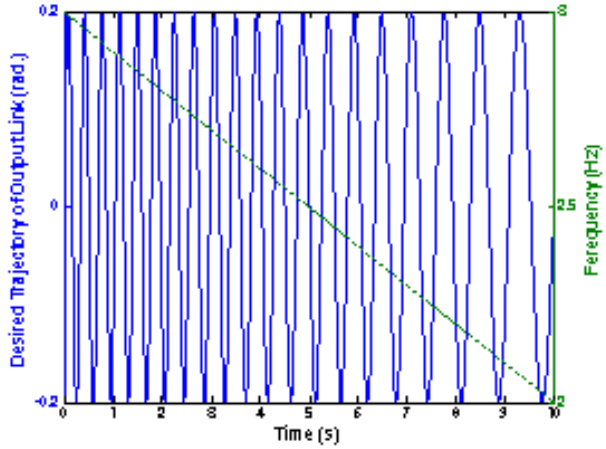

Figure 5.12: Position (solid) and frequency (dotted) of the desired link trajectory as a function of time.

continuously exploited.

Figure 5.13 shows the power consumption of AwAS for different levels of fixed stiffness while the frequency is changing, and the power consumption of AwAS when stiffness is continuously regulated (solid line). For the first strategy, each curve has its minimum power consumption when frequency of the motion matches the natural frequency of the output link. The energy consumption is the surface area under each curve.

For the first strategy, the minimum energy consumption is 28.6 J, whereas with the continuously varying stiffness strategy the total energy consumption of AwAS (of both the main joint position actuator and the stiffness actuator) was reduced to 21.3 J, which is 7.3 J (25%) less than the minimum energy consumption achieved by the first strategy. The reason is that, since to change the stiffness, AwAS does not consume a high amount of energy, changing the stiffness continuously during this task is energetically beneficial. This will not be the case for most of the other implementation of variable stiffness actuators, which have higher energy costs for the stiffness tuning.

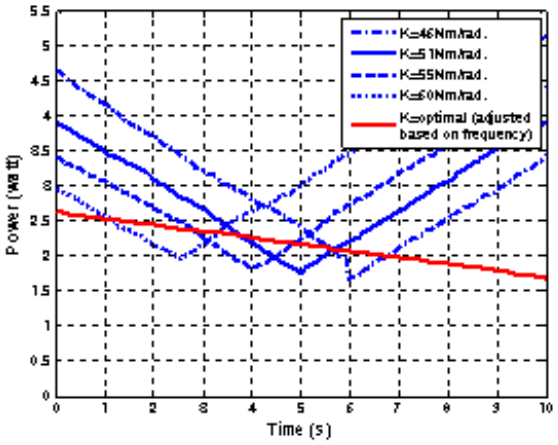

Figure 5.13: Power consumption of AwAS as a function of time for different fixed value of the stiffness while frequency is changing and also when stiffness changes based on the frequency.

The output link and intermediate link trajectories for the second strategy are shown in Figure 5.14. Due to continuous adaptation of the natural dynamics the motion amplitude of the intermediate link (main joint actuator) is kept very small, which reduces the energy consumption.

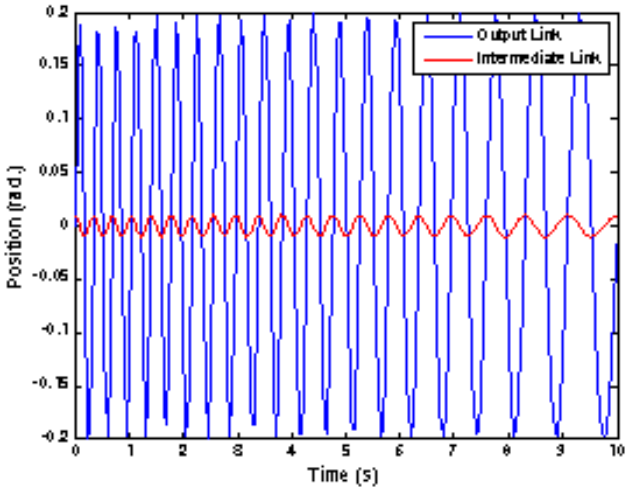

Figure 5.14: Link (blue) and Intermediate link (red) trajectories when natural dynamics is exploited based on the frequency in the real time.

Chapter 6

Zero Moment Point in Walking

The goal of this Chapter is to present an analysis on zero moment point (ZMP) walking and, in particular, the results presented in [59].

6.1 Geometric interpretation of the ZMP

The Zero-Moment Point (ZMP) [60], is widely known in the area of walking robots. Numerous researchers have investigated this point and have given their own definitions and interpretations of it (for references, see section 6.2). Even more researchers have used the ZMP as a gait synthesis or control tool, which shows the importance of this point.

The theory on screws, introduced by Ball [61] in 1900 is, unfortunately, less used among roboticists. The theory gives a 6D generalization of velocity and force, being the Twist and Wrench respectively. This approach is coordinate-free, meaning that the equations and their results are invariant for the choice of coordinates. So, one does not have to choose coordinates at all before writing down the motion equations for the system. The lack of coordinates gives greater flexibility (the equations work for any orientation of the robot; they are not limited to a certain pose in the world), reduces the chance of errors (*e.g.*, one cannot be tempted to make assumptions like 'the robot will walk approximately in x-direction, so let's use the x-coordinate for the distance traveled' because the lack of coordinates implies that no x-direction was defined in the first place), and most importantly, mimic what happens in nature: nature does not have coordinates at all; the laws are completely dictated by the physics of the system, by nothing more. The concept is also called 'geometric dynamics', emphasizing the fact that everything follows from the geometric properties of the system (in a broad sense, *e.g.*, geometric mass and force distribution), not from the way you look at the system (*i.e.*, which coordinates you use).

In this Chapter, we combine the knowledge of the Zero-Moment Point and screw theory, to give a novel, geometric interpretation of the Zero-Moment Point. We will show how the position of the ZMP can be found from the ground reaction wrench (generalization of the well-known ground reaction force) and geometric rules on wrench decomposition. This leads to more insight in the position of the ZMP and how this relates to the ground wrench exerted on the foot. Firstly, in sections 6.2 and 6.3 we will introduce the key terms of this Chapter further. We will address some issues of the ZMP, and show how a wrench can be shown uniquely in a graphical way. In section 6.4 we will show and prove three ways of decomposing a wrench into two separate components (analogous to decomposition of a

force into two components). Then, in section 6.5, we will present the main contribution of this Chapter, being the relation between the ground reaction wrench and the ZMP. In section 6.6 it will be shown that this leads to a simple explicit expression for the ZMP position. Finally the conclusions and future work will be discussed in section 6.7.

6.2 The Zero-Moment Point

The Zero-Moment Point, ZMP, was introduced by by M. Vukobratović and D. Juričić around 1969 [62, 63] (although the term ZMP was only introduced a few years later). It should be noted that "...the notion of ZMP has never been introduced in the form of a formal definition..." [60]. This has given rise to dozens of researchers giving their own definitions and interpretations to this point. In general, the definitions of the ZMP can be divided into two groups:

1. Definitions in which the position of the ZMP is related to gravity and inertia forces, *e.g.*:
   - "The ZMP is defined as that point, on the ground at which the net moment of the inertial forces and the gravity forces has no component, along the horizontal axes." [64]
   - "The ZMP is the point on the ground where the tipping moment acting on the biped, due to gravity and inertia forces, equals zero, the tipping moment being defined as the component of the moment that is tangential to the supporting surface." [65]
2. Definitions in which the position of the ZMP is related to the ground-reaction force acting on the robot, *e.g.*:
   - "The ZMP (Zero-Moment Point) is defined to be a point on the ground at which the tangential component of the moment generated by the ground reaction force/moment becomes zero." [66]
   - "The pressure under supporting foot can be replaced by the appropriate reaction force acting at a certain point of the mechanism's foot. Since the sum of all moments of active forces with respect to this point is equal to zero, it is termed the Zero-Moment Point (ZMP)."[1] [67]

Interestingly, both cited definitions in group 1 (as well as most others in this group) fail to include external disturbance forces (such as someone pushing the robot), which makes these definitions incomplete. After fixing this (for example, the first definition would become: The ZMP is defined as that point, on the ground at which the net moment of the inertial forces, the external disturbance and gravity forces has no component, along the horizontal axes), all definitions are correct and (necessarily) will give the same location for the ZMP.

[1] At first glance, this definition seems incorrect because it is well-known that the existence of a moment around the ZMP *is* allowed as long as it is has no component along the ground surface. However, the author (the inventor of the ZMP) cleverly chose to use the 'pressure under supporting foot', which, by definition, only has a component perpendicular to the ground surface. This indeed results in an appropriate reaction force at the ZMP having no moment at all. The friction forces along the ground surface, that *would* give a vertical moment around the ZMP, were simply ignored.

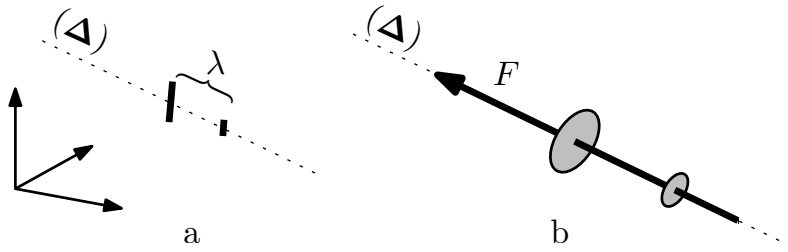

Figure 6.1: a) Graphical representation of a screw S. The pitch λ is shown with two small ticks on the axis (direction from the large to the small disk). b) Graphical representation of a wrench in a 3D space: the magnitude of force F along axis (Δ) is indicated by the length of the arrow. The magnitude of moment M along (Δ) is indicated by the distance between the two discs (direction from the large to the small disc). Note that we did not explicitly draw the pitch anymore, as drawing the magnitude of the moment directly gives the same information but in a more intuitive way.

This location is equal to the location of the Center of Pressure (CoP). A sufficient amount of papers have already been written to prove all this [68, 65], so we will not repeat that[2].

Contrary to what is stated in many papers (*e.g.*, [60]), there is no direct relation between the ZMP lying strictly within the support polygon (as opposed to lying on the edge of it) and 'falling' of the robot. Two examples suffice to show this:

1. Consider a bipedal robot standing on one leg, having unactuated ankles. This system acts like an (unstable) inverted pendulum and thus the robot falls down. However, as no torques were exerted on the foot, the foot could remain on the ground without starting to rotate, so the ZMP was always inside the support polygon.

2. Consider a bipedal robot walking exactly like a human, without falling. Just like humans do, the robot will rotate its feet about the front and rear edge while walking, so the ZMP sometimes does lie on the edge of the support polygon (not strictly within it) although the robot is not falling.

To be short, the ZMP lying strictly within the support polygon only tells us that the stance foot (or feet, if the robot is in double-support phase) will not start to rotate about one of its edges. This is neither a sufficient nor a necessary condition for walking without falling. It must be said however, that having the ZMP strictly within the support polygon makes continuous pose control of the robot a lot easier[3], which is probably the reason that so many people think that it is the only solution.

6.3 Wrench — a 6D force

In this Chapter, we will use the widely known concept of wrenches, from geometric mechanics [61, 69] . A wrench is a 6D generalization of a force. Any combination of (linear)

[2]Note that in these papers it was assumed that there are no external disturbances, but the results still hold if there are.

[3]When the foot is rotating about one of its edges, we essentially have an underactuated system, which is hard to control exactly. Luckily, for walking without falling, we believe it is not necessary to exactly control the robot's pose at all times.

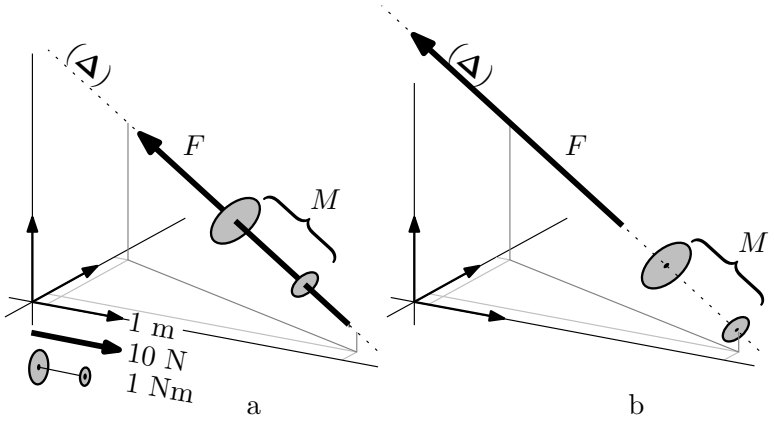

Figure 6.2: a) Introduction of reference lengths. In the lower left, a scale for meter, Newton and Newton meter are given. It can be deduced that this wrench has $|F| = 35$ N, $|M| = 2.4$ Nm and (thus) $\lambda = -0.07$ m. The vector and discs can (independently) be freely translated along the axis without losing meaning, hence b) represents the same wrench. Unless otherwise noted, we will use the scaling shown in this figure for the other figures in this chapter.

forces and (rotational) moments can be replaced by a single force and a moment in a plane perpendicular to the force (Poinsot's theorem, [61]) and therefore by one wrench.

Before introducing the wrench, we will introduce the notion of a *screw*. A screw S consists of an (undirected) axis $(\boldsymbol{\Delta})$ in space and an associated scalar $\lambda \in \mathbb{R}$ called the *pitch* (the unit of λ is [m]). The axis can be fully specified by the position r of some point on the axis and a (unit) direction vector ω, such that $(\boldsymbol{\Delta}) = \{r + \alpha\,\omega | \alpha \in \mathbb{R}\}$. The pitch defines the ratio between 'translation (or translational force) along the axis' and 'rotation (or rotational moment) about the axis'. A graphical representation of a screw is shown in figure 6.1a. Note that, because the axis is undirected, the screw $S = (\omega, r, \lambda)$ is the same screw as $S^* = (-\omega, r, \lambda)$.

A wrench W, having *intensity* v, on a screw S (having axis $(\boldsymbol{\Delta})$ and pitch λ) can be interpreted as a combination of:

1. A (linear) force $F = v \cdot \omega$ along axis $(\boldsymbol{\Delta})$, and
2. A (rotational) moment $M = \lambda F = \lambda\, v \cdot \omega$ along axis $(\boldsymbol{\Delta})$.

The pitch λ is the ratio between amount of moment (in [Nm]) and amount of force (in [N]). In order for the wrench to be fully specified, the parameters of the screw S must be known, as well as the intensity v of the wrench. This is similar to the case of a linear force on an axis: there the parameters of the axis as well as the magnitude of the force are enough for the force to be fully specified. In order to specify the direction of the force (either towards one end of the axis or towards the other), we will use the direction of vector ω: if the force goes into the direction of ω, we will denote a positive v, otherwise a negative one.

A graphical representation of a wrench is shown in figure 6.1b. The magnitude of the force (which is equal to the intensity of the wrench) and magnitude of the moment are indicated with the lengths of the arrow and distance between the disks respectively. In order to have a meaning, 'reference lengths' must be given. This is shown in figure 6.2: a 3D reference frame is given for the positions, and 1D references (aligned with one axis of

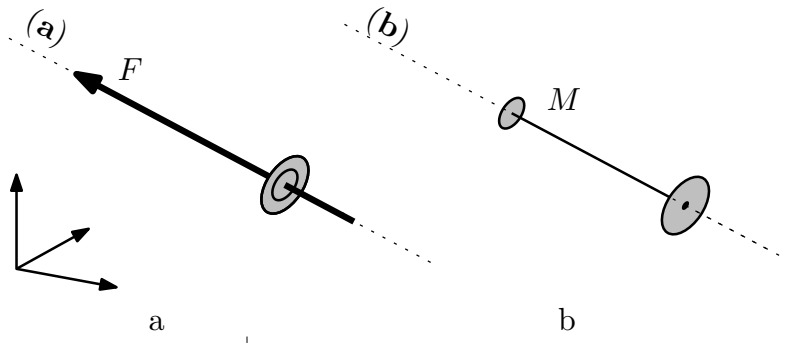

Figure 6.3: a) A wrench representation of a pure force ($\lambda = 0$). b) The wrench representation of a pure moment ($\lambda = \infty$). For reference lengths, see figure 6.2.

the 3D reference frame) are given for force and moment magnitude. Because the unit lengths for forces and moments do not need to be the same (as is the case in figure 6.2), a pitch of $\lambda = 1$ [m] is not necessarily represented by a vector and disks that have the same length/distance.

The numerical expression of the wrench depends on the choice of coordinates, thus on the chosen reference frame Ψ_{ref}. Hence, when expressing a wrench in numbers, the choice of coordinates *must* always be given, otherwise it is unclear what the numbers actually mean. In this Chapter, we use a pre-pended superscript to express the reference frame, in the following way:

$$^{a}W: \text{ A wrench expressed in reference frame } \Psi_a. \tag{6.1}$$

Note that it is necessary to denote the reference frame only when a wrench is expressed in numbers; not when drawing the wrench graphically (which makes drawing wrenches completely coordinate-free).

One way to numerically represent a wrench is in so-called *Plücker coordinates* [70]:

$$^{\text{ref}}W = \begin{pmatrix} m \\ f \end{pmatrix} = v\,(\underbrace{\begin{pmatrix} r \wedge \omega \\ \omega \end{pmatrix}}_{\text{linear force}} + \lambda \underbrace{\begin{pmatrix} \omega \\ 0 \end{pmatrix}}_{\text{moment}}), \tag{6.2}$$

where v refers to the intensity of the wrench, r is a vector from the reference frame's origin to some point on the screw axis, ω is the unit vector indicating the direction of the axis and λ is the pitch. The $\wedge$ denotes the cross product. m and f are (3×1) vectors. The coordinates $\left(\begin{smallmatrix} m \\ f \end{smallmatrix}\right)$ can be interpreted as follows: the wrench W is equal to a linear force f exerted at the origin of the reference frame, plus a moment m. Clearly, the coordinates depend on the choice of reference frame, as r and ω depend on the reference frame. A special case is obtained when $r = 0$, *i.e.*, the reference frame is on the axis $(\mathbf{\Delta})$. In that case we obtain

$$^{(\mathbf{\Delta})}W = v(\begin{pmatrix} 0 \wedge \omega \\ \omega \end{pmatrix} + \lambda \begin{pmatrix} \omega \\ 0 \end{pmatrix}) = \begin{pmatrix} \lambda v \cdot \omega \\ v \cdot \omega \end{pmatrix} = \begin{pmatrix} M \\ F \end{pmatrix}, \tag{6.3}$$

which is again the form we began with.

A pure force F along an axis $(\mathbf{a})$ can be represented by a wrench with intensity $v = |F|$ along a screw with axis $(\mathbf{a})$ and zero pitch. In Plücker coordinates this results in:

$$^{\text{ref}}W^{\text{force}} = v\,(\begin{pmatrix} r \wedge \omega \\ \omega \end{pmatrix} + 0 \cdot \begin{pmatrix} \omega \\ 0 \end{pmatrix}) = v \begin{pmatrix} r \wedge \omega \\ \omega \end{pmatrix}. \tag{6.4}$$

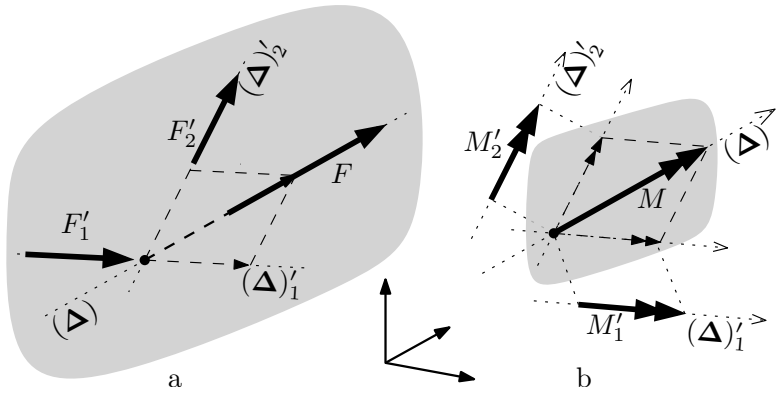

Figure 6.4: a) A linear force F, decomposed into two components F_1' and F_2'. b) A moment M, decomposed into two components M_1' and M_2'.

So, even though this describes a pure force, the moment part in Plücker coordinates is non-zero. A pure moment M about an axis $(\mathbf{b})$ can be represented by a wrench with intensity $v \to 0$ along a screw with axis $(\mathbf{b})$ and infinite pitch $\lambda \to \infty$; such that the magnitude of the moment becomes a finite value: $v^* = \lambda v = |M|$. Here we introduced the *pseudo-intensity* v^* in order to circumvent problems with zero intensity. In Plücker coordinates we have:

$$\begin{aligned} {}^{\text{ref}}W^{\text{mom}} &= \lim_{\substack{v\to 0 \\ \lambda v \to |M|}} v\,\Big(\begin{pmatrix} r \wedge \omega \\ \omega \end{pmatrix} + \lambda \begin{pmatrix} \omega \\ 0 \end{pmatrix}\Big) = \lambda v \begin{pmatrix} \omega \\ 0 \end{pmatrix} \\ &= v^*\Big(\frac{1}{\lambda}\begin{pmatrix} r \wedge \omega \\ \omega \end{pmatrix} + \begin{pmatrix} \omega \\ 0 \end{pmatrix}\Big) = v^* \begin{pmatrix} \omega \\ 0 \end{pmatrix}. \end{aligned} \tag{6.5}$$

From (6.5) it is clear that, indeed, a pure moment is invariant for translation of its axis: the position of the axis, indicated by r, falls out of the equation. In figure 6.3 the graphical representation of a pure force and a pure moment as wrench are shown.

6.4 Decomposition of a wrench

The principle behind decomposition of wrench W is to find wrenches $W_1' \ldots W_n'$ that, together, do the same work as W when applied on a moving rigid body for any motion. Mathematically this is not challenging at all, since wrenches represented in Plücker coordinates can be summed:

$${}^{\text{ref}}W = \sum_i \left({}^{\text{ref}}W_i'\right). \tag{6.6}$$

Geometrically however, the problem is much more interesting: given n screws $S_1' \ldots S_n'$, do there exist wrench intensities $v_1' \ldots v_n'$ such that the composition of the n wrenches together yields the original wrench W?

In this section, we give conditions for the decomposition of a wrench W on screw S into two components W_1', W_2' along screws S_1', S_2'. Decomposition into more than two forces is not considered because it is not needed in this Chapter. Before that, we will review some decomposition rules for pure forces and pure moments:

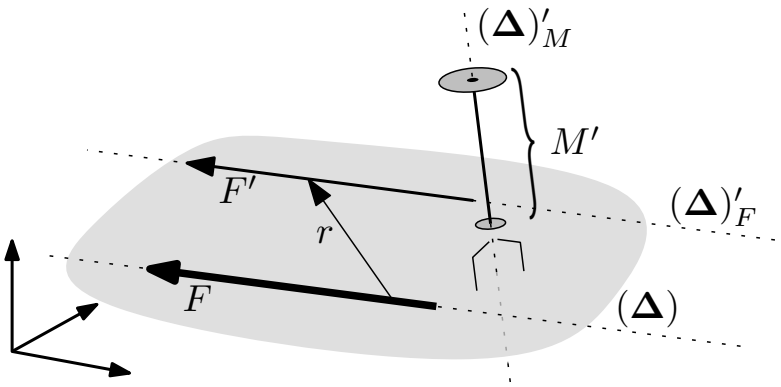

Figure 6.5: Decomposition of force F into (translated) force F' and moment M'. F and r are not necessarily perpendicular.

DEC1 A pure force F along axis (Δ) can be decomposed in pure forces F'_1 and F'_2 along axes $(\Delta)'_1$ and $(\Delta)'_2$ if and only if:

1. either the axes (Δ), $(\Delta)'_1$ and $(\Delta)'_2$ intersect each other in one point p and the plane spanned by the direction vectors ω'_1 and ω'_2 (which must have distinct directions) contains the direction vector ω,
2. or all axes (Δ), $(\Delta)'_1$ and $(\Delta)'_2$ are parallel and lie in the same plane.

It can be shown that the second condition is actually the limit case for $p \to \infty$ of the first condition. If $(\Delta)'_1$ and $(\Delta)'_2$ are different from each other, then the decomposition is unique, *i.e.*, there exists exactly one set of force magnitudes $\{|F'_1|, |F'_2|\}$ that yield a valid decomposition.

DEC2 A pure moment M along an axis (Δ) can be decomposed in pure moments M'_1, M'_2 along axes $(\Delta)'_1, (\Delta)'_2$ if and only if:

1. either the plane spanned by the direction vectors ω'_1 and ω'_2 (which must have distinct directions) contains the direction vector ω,
2. or all axes (Δ), $(\Delta)'_1$ and $(\Delta)'_2$ are parallel.

In the first case, the decomposition is unique, in the second case it is not. Note that the decomposition rule for a pure force (DEC1) is a subset of the decomposition rule for a pure moment. Hence, a moment can always be decomposed along axes that fulfill the conditions for force decomposition.

DEC3 A force F along axis (Δ) can be decomposed into a force F' along axis $(\Delta)'_f$ and a moment M' about an axis $(\Delta)'_m$ if and only if $(\Delta) \parallel (\Delta)'_f$ and $(\Delta)'_m$ is perpendicular to the plane spanned by (Δ) and $(\Delta)'_f$. Let r be a vector from some point on (Δ) to some point on $(\Delta)'_f$. Then $|F'| = |F|$ and $|M'| = -r \wedge F$. See figure 6.5.

For general wrenches, things are a bit more complicated: we do not only have restrictions on the axes, but also on the pitches of each screw. Firstly, we will present two trivial cases of a wrench decomposition into two components.

Theorem 1 *A wrench W on screw S can be decomposed into one wrench W'_f on screw S'_f representing a pure force ($\lambda'_F = 0$) plus one wrench W'_m on screw S'_m representing a pure moment ($\lambda'_m = \infty$), if axis $(\mathbf{\Delta})'_f$ coincides with $(\mathbf{\Delta})$ and axis $(\mathbf{\Delta})'_m$ is parallel to $(\mathbf{\Delta})$.*

Proof: Assume that the conditions on axes $(\mathbf{\Delta})'_f$ (defined by ω'_f and r'_f) and $(\mathbf{\Delta})'_m$ (defined similarly) are met, *i.e.*, $\omega'_f = \pm\omega$; $r'_f = r$; $\omega'_m = \pm\omega$; $r'_m =$ artbitrary. Without loss of generality we can assume that $\omega'_f = \omega'_m = \omega$ (by changing the sign of the wrench (pseudo-)intensities v'_f and $v^{*\prime}_m$ if necessary). By expressing the wrench in Plücker coordinates (and using (6.4) and (6.5)), we can show that indeed there exist intensities v'_f and $v^{*\prime}_m$ that give a valid decomposition $W = W'_f + W'_m$:

$$v \begin{pmatrix} r \wedge \omega \\ \omega \end{pmatrix} + \lambda v \begin{pmatrix} \omega \\ 0 \end{pmatrix} = v'_f \begin{pmatrix} r'_f \wedge \omega'_f \\ \omega'_f \end{pmatrix} + v^{*\prime}_m \begin{pmatrix} \omega'_m \\ 0 \end{pmatrix} \tag{6.7}$$

so choosing $v'_f = v$ and $v^{*\prime}_m = \lambda v$ will do. This is actually just the way a wrench is built in the first place: it consists of a pure force $F = v \cdot \omega$ along axis $(\mathbf{\Delta})$ plus a pure moment $M = \lambda v \cdot \omega$ around this axis. □

The converse of this theorem (decomposition is possible only if the screw axes satisfy the constraints) is not true. As a counter-example see DEC3, where a wrench (a pure force in this case) is decomposed into a pure force and pure moment while the screws are perpendicular instead of parallel.

Theorem 2 *A wrench W of intensity v on screw S, can be decomposed into two wrenches W'_1 and W'_2 on screws S'_1 and S'_2 if the axes $(\mathbf{\Delta})'_1$ and $(\mathbf{\Delta})'_2$ satisfy the conditions of DEC1 and the pitches satisfy $\lambda'_1 = \lambda'_2 = \lambda$.*

Proof: The screws S, S'_1 and S'_2 can be represented by axis locations r, r'_1 and r'_2, axis directions ω, ω'_1 and ω'_2 and common pitch $\lambda = \lambda'_1 = \lambda'_2$.

First condition — Without loss of generality we can assume that the location vectors point to the intersection point and thus $r = r'_1 = r'_2$. The condition that ω'_1 and ω'_2 span a plane which contains ω implies that there exist an α and β such that $\omega = \alpha\omega'_1 + \beta\omega'_2$. Now by choosing intensities $v'_1 = \alpha v$ and $v'_2 = \beta v$, we can write

$$\begin{aligned} W'_1 + W'_2 = \\ v'_1\Big(\begin{pmatrix} r \wedge \omega'_1 \\ \omega'_1 \end{pmatrix} + \lambda \begin{pmatrix} \omega'_1 \\ 0 \end{pmatrix} \Big) + v'_2\Big(\begin{pmatrix} r \wedge \omega'_2 \\ \omega'_2 \end{pmatrix} + \lambda \begin{pmatrix} \omega'_2 \\ 0 \end{pmatrix} \Big) = \\ \begin{pmatrix} r \wedge (v'_1\omega'_1 + v'_2\omega'_2) \\ v'_1\omega'_1 + v'_2\omega'_2 \end{pmatrix} + \lambda \begin{pmatrix} v'_1\omega'_1 + v'_2\omega'_2 \\ 0 \end{pmatrix} = \\ v\Big(\begin{pmatrix} r \wedge \omega \\ \omega \end{pmatrix} + \lambda \begin{pmatrix} \omega \\ 0 \end{pmatrix} \Big) = W \end{aligned} \tag{6.8}$$

which shows that indeed there exists a decomposition.

Second condition — All axes are parallel, thus $\omega = \omega'_1 = \omega'_2$. Without loss of generality we can assume that r, r'_1 and r'_2 lie on one line, thus there exist an α such that

$r = \alpha\, r'_1 + (1-\alpha) r'_2$. Now by choosing $v'_1 = \alpha v, v'_2 = (1-\alpha)v$, we can write

$$W'_1 + W'_2 = v'_1\left(\begin{pmatrix} r'_1 \wedge \omega \\ \omega \end{pmatrix} + \lambda \begin{pmatrix} \omega \\ 0 \end{pmatrix}\right) + v'_2\left(\begin{pmatrix} r'_2 \wedge \omega \\ \omega \end{pmatrix} + \lambda \begin{pmatrix} \omega \\ 0 \end{pmatrix}\right) = \begin{pmatrix} (v'_1 r'_1 + v'_2 r'_2) \wedge \omega \\ (v'_1 + v'_2)\,\omega \end{pmatrix} + (v'_1 + v'_2)\lambda \begin{pmatrix} \omega \\ 0 \end{pmatrix} = v\left(\begin{pmatrix} r \wedge \omega \\ \omega \end{pmatrix} + \lambda \begin{pmatrix} \omega \\ 0 \end{pmatrix}\right) = W \tag{6.9}$$

which shows that indeed there exists a decomposition. □

The converse of this theorem is not true: there are many sets of screws $\{S'_1, S'_2\}$ along which a wrench can be decomposed that do not satisfy the above conditions.

Continuing on Theorem 1, a more general theorem can be stated, which will be useful for the determination of the ZMP later on:

Theorem 3 *A wrench W of intensity v on screw S, can be decomposed into a wrench representing a pure force W'_f on screw S'_f (having $\lambda'_f = 0$) and a wrench representing a pure moment W'_m on screw S'_m (having $\lambda'_m = \infty$) if and only if:*

- *axes $(\boldsymbol{\Delta})$ and $(\boldsymbol{\Delta})'_f$ are parallel (i.e., S'_f is obtained by translating S a certain distance $(r'_f - r)$), and*
- *the translation vector $(r'_f - r)$ is such that*

$$\omega \wedge (r'_f - r) + \lambda\omega \parallel \omega'_m. \tag{6.10}$$

Proof: A valid decomposition can be made if and only if there exist (pseudo-)intensities v'_f and $v^{*\prime}_m$ such that $W = W'_f + W'_m$:

$$v\begin{pmatrix} r \wedge \omega \\ \omega \end{pmatrix} + v\lambda \begin{pmatrix} \omega \\ 0 \end{pmatrix} = v'_f \begin{pmatrix} r'_f \wedge \omega'_f \\ \omega'_f \end{pmatrix} + v^{*\prime}_m \begin{pmatrix} \omega'_m \\ 0 \end{pmatrix}. \tag{6.11}$$

The lower line of (6.11) implies that $v\omega = v'_f \omega'_f$, thus (because ω and ω'_f are unit vectors) $\omega'_f = \pm\omega$ and $v'_f = \pm v$. Again, without loss of generality we may assume that ω and ω'_f have the same direction (*i.e.*, are not opposite). The top line of (6.11) can now be written as

$$(r - r'_f) \wedge \omega + \lambda\omega = \frac{v^{*\prime}_m}{v}\,\omega'_m. \tag{6.12}$$

Indeed, a suitable $v^{*\prime}_m$ can be found if and only if the left hand side of (6.12) is parallel to ω'_m. □

This result implies that for a given ω, ω'_m and $\lambda \neq 0$ there exists one location of screw S'_f for which a valid decomposition exists (any translation $(r - r'_f)$ which satisfies (6.12) gives the same axis location; only translated along the axis itself, for which the axis is invariant). If $\lambda = 0$ (W is a pure force), then there are two possibilities: either $\omega'_m \perp \omega$, in which case a valid decomposition exists for any translation of S perpendicular to ω'_2 (this is equivalent to DEC3), or no decomposition on S'_f and S'_m exists at all. If one would take $\omega'_m = \omega'_f = \omega$, then the system reduces to the system described Theorem 1; then indeed (6.12) only has a solution for $r'_f = r$, *i.e.*, the screws S and S'_f coincide.

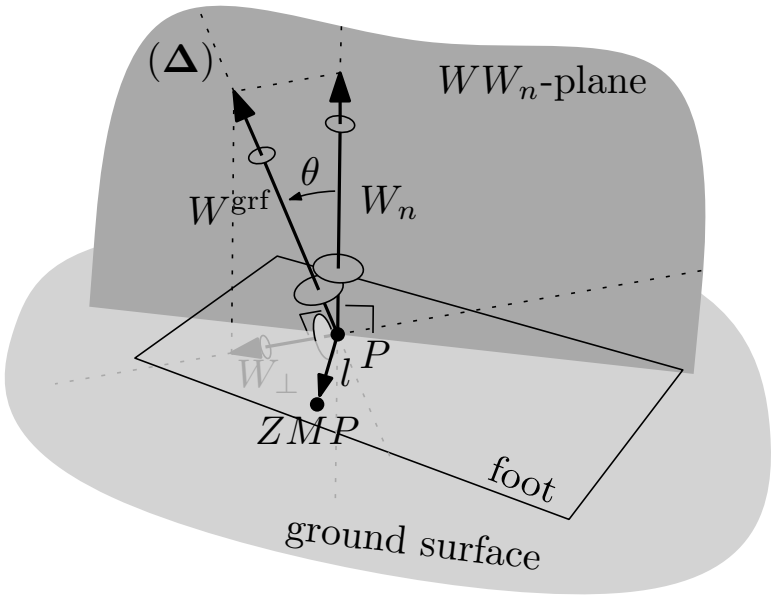

Figure 6.6: Geometric construction of the Zero-Moment Point from the ground contact wrench W^{grf}.

6.5 Construction of the ZMP using the ground reaction wrench

If the ground reaction wrench W^{grf} is known, the Zero-Moment Point can quite easily be found geometrically. First we show how this is done; second we will prove that indeed this algorithm gives us the ZMP.

1. Given the ground contact wrench W^{grf}, on screw S (defined by axis $(\boldsymbol{\Delta})$ and pitch λ), find the point P, being the intersection between $(\boldsymbol{\Delta})$ and the ground plane.

2. By using theorem 2, decompose W^{grf} (which has a force component f and a moment component $m = \lambda f$) into a wrench W_n normal to the ground surface plus a wrench $W_\perp$ perpendicular to W^{grf}, intersecting each other in point P. The force and moment components of the obtained wrenches are denoted $f_n, f_\perp$ and $m_n, n_\perp$ respectively. Note that $m_n = \lambda f_n$, $m_\perp = \lambda f_\perp$ and $W_n + W_\perp = W^{\mathrm{grf}}$.

3. Construct a vector l from point P, perpendicular to the plane spanned by W and W_n (this plane is denoted by WW_n), having magnitude $|l| = \lambda \frac{|f_\perp|}{|f|}$ (more precisely, the direction of l follows from applying the right-hand rule, going from W_n to W^{grf}).

4. Now l points to the Zero-Moment Point.

The whole procedure is also sketched in figure 6.6.

Proof: The proof shows that the ground reaction wrench is equivalent to a pure force f' acting on the ZMP plus a moment m'_n that is perpendicular to the ground surface.

We introduce a euclidean fixed-world frame Ψ_0 somewhere in space with an arbitrary orientation, a vector p pointing from the fixed world's origin to point P and a vector $z = p + l$

pointing from the fixed world's origin to the supposed position of the ZMP. f' and m'_n can be written as a wrench as $W^{f'} = \begin{pmatrix} z \wedge f' \\ f' \end{pmatrix}$ and $W^{m'_n} = \begin{pmatrix} m'_n \\ 0 \end{pmatrix}$ respectively.

Assume that indeed l points to the ZMP, then the above defined f' and m'_n should exist such that

$$\begin{gathered} W^{\text{grf}} = W^{f'} + W^{m'_n} \\ \begin{pmatrix} p \wedge f \\ f \end{pmatrix} + \lambda \begin{pmatrix} f \\ 0 \end{pmatrix} = \begin{pmatrix} z \wedge f' \\ f' \end{pmatrix} + \begin{pmatrix} m'_n \\ 0 \end{pmatrix}. \end{gathered} \tag{6.13}$$

From this, it follows directly that $f' = f$. Because $z = p + l$, we can write the top row of (6.13) as $p \wedge f + \lambda f = p \wedge f' + l \wedge f' + m'_n$ which can be simplified to ($f = f'$)

$$\lambda f = l \wedge f + m'_n. \tag{6.14}$$

It can be shown that $l \wedge f = m_\perp$ by proving the following (sufficient) conditions:

1. $m_\perp \perp l$ — l is perpendicular to W and W_n and, consequently, to any vector in the plane spanned by them. Now $W_\perp$ is in this plane, and thus so is $m_\perp$ (which has the same direction as $W_\perp$).

2. $m_\perp \perp f$ — $W_\perp$ was constructed perpendicularly to W. By construction $m_\perp \parallel W_\perp$ and $f \parallel W$. Therefore we have indeed $m_\perp \perp f$.

3. $|l \wedge f| = |m_\perp|$ — by $|l \wedge f| = |l| \cdot |f| = \lambda \frac{|f_\perp|}{|f|} \cdot |f| = |\lambda f_\perp| = |m_\perp|$.

4. $l \wedge f = m_\perp$ follows the right-hand rule — by inspection of figure 6.6.

By using $l \wedge f = m_\perp$, (6.14) can be rewritten as

$$\lambda f = m = m_\perp + m'_n \tag{6.15}$$

so we can conclude that indeed there exists an $f' = f$ and $m'_n = m_n$ that satisfy (6.13), so indeed l points to the Zero-Moment Point. □

Remark 6.5.1 Both step 1 and 2 of the algorithm are only possible if $(\boldsymbol{\Delta})$ is not parallel to the ground plane. This is logical because if $(\boldsymbol{\Delta})$ were parallel to the ground plane, the ground does not exert a normal force; i.e., the ground does not support the foot and in that case the ZMP does not exist. ◁

Remark 6.5.2 If $(\boldsymbol{\Delta})$ is almost vertical, i.e., the friction forces are much smaller than the normal force, we can approximate the magnitude $|l|$ as follows: let θ be the angle between f_n and f (see figure 6.6); then $\frac{|f_\perp|}{|f|} = \tan\theta \approx \theta \Rightarrow |l| \approx \lambda\theta$. ◁

Remark 6.5.3 As l is perpendicular to W_n (and thus to the ground's normal), it it automatically parallel to the ground surface. Therefore, l points to a point belonging to the ground surface; which is in agreement with the common-known fact that the ZMP is a point on the ground surface. ◁

Remark 6.5.4 We never stated that the ground should be horizontal. In fact, we did not even draw the reference from which a 'world's horizontal plane' could be deduced. This method works for any orientation of the ground plane (and the orientation does not need to be known either). Of course, the ground surface should be flat where it is in contact with the foot, otherwise the ZMP notion makes no sense [71].

◁

Remark 6.5.5 From a decomposition point of view, the algorithm can be interpreted as follows. The ground reaction wrench consists of a force f and a moment m along the same axis (Δ). In order to find the ZMP, we want to find a decomposition in a purely vertical moment and a pure force. The moment m can be seen as the composition of a'wanted' vertical component m_n and an 'unwanted' remainder $m_\perp$. In order to cancel the latter, we can translate f (according to Theorem 3) along l, which introduces a canceling moment $-m_\perp$. The result is a translated version of f and the sum of all moments $m_n + m_\perp + (-m_\perp) = m_n$, which is exactly what we were looking for. ◁

6.6 Explicit expression for the ZMP position, given the ground reaction wrench

Assume that a reference frame Ψ_0 is attached to the ground surface, such that the frame's xy-plane coincides with the ground surface and the frame's z-axis points out of the ground (note that we do not require the ground surface be horizontal) and that the ground reaction wrench is known expressed in this frame, being ${}^0W^{\mathrm{grf}}$. By using (6.13), it is easy to find an explicit expression for the position of the ZMP, as shown below. The ground reaction wrench can be written as

$$ {}^0W^{\mathrm{grf}} = \begin{pmatrix} {}^0m \\ {}^0f \end{pmatrix} = \begin{pmatrix} {}^0z \wedge {}^0f' \\ {}^0f' \end{pmatrix} + \begin{pmatrix} {}^0m'_n \\ 0 \end{pmatrix} \tag{6.16} $$

where ${}^0z$ (the position of the ZMP expressed in coordinates of Ψ_0) is the unknown. Expanding the cross product and noting that ${}^0f' = {}^0f$, we obtain for the top row of (6.16)

$$ \begin{pmatrix} {}^0m_x \\ {}^0m_y \\ {}^0m_z \end{pmatrix} = \begin{pmatrix} -{}^0z_z \cdot {}^0f_y + {}^0z_y \cdot {}^0f_z \\ {}^0z_z \cdot {}^0f_x - {}^0z_x \cdot {}^0f_z \\ -{}^0z_y \cdot {}^0f_x + {}^0z_x \cdot {}^0f_y \end{pmatrix} + \begin{pmatrix} {}^0m'_{nx} \\ {}^0m'_{ny} \\ {}^0m'_{nz} \end{pmatrix} . \tag{6.17} $$

The actually chosen position and orientation of Ψ_0 implies that the coordinates of the ZMP, ${}^0z$, and the normal moment, ${}^0m'_n$, satisfy

$$ {}^0z = \begin{pmatrix} {}^0z_x \\ {}^0z_y \\ {}^0z_z \end{pmatrix} = \begin{pmatrix} \bullet \\ \bullet \\ 0 \end{pmatrix} ; {}^0m'_n = \begin{pmatrix} {}^0m'_{nx} \\ {}^0m'_{ny} \\ {}^0m'_{nz} \end{pmatrix} = \begin{pmatrix} 0 \\ 0 \\ \bullet \end{pmatrix} . \tag{6.18} $$

By rewriting the first two lines of (6.17) and substituting the results from (6.18), we obtain the simple explicit equation for the position of the ZMP expressed in coordinates of frame Ψ_0:

$$ {}^0z = \begin{pmatrix} {}^0z_x \\ {}^0z_y \\ {}^0z_z \end{pmatrix} = \begin{pmatrix} -{}^0m_y / {}^0f_z \\ {}^0m_x / {}^0f_z \\ 0 \end{pmatrix} . \tag{6.19} $$

6.7 Conclusions and future work

In this Chapter, we have shown that the concept of screws and wrenches gives us tools to geometrically establish the relation between the ground reaction wrench and the Zero-Moment Point. In order to arrive at this, we showed how a wrench can be decomposed into separate components. The proposed method gives a general, completely coordinate-free way to find the ZMP and contributes in improving the geometrical insight.

We are planning to extend this theory, and give geometric interpretations of other concepts, such as the capture point and capture region. In order to do this, we will firstly try to capture the dynamics of the system in terms of screws (which can certainly be done, as the (generalized, 6D) momentum of a rigid body can be seen as a screw as well [72].

Bibliography

[1] J. Rose and J. Gamble, *Human Walking*. Williams & Wilkins, 2005.

[2] V. Inman, H. Ralston, and F. Todd, *Human Walking*. Williams & Wilkins, 1981.

[3] D. A. Winter, *The Biomechanics and Motor Control of Human Gait: Normal, Elderly, and Pathological*. University of Waterloo Press, 1991.

[4] R. Ünal, R. Carloni, E. Hekman, S. Stramigioli, and H. Koopman, "Conceptual design of an energy efficient transfemoral prosthesis," in *Proceedings of the IEEE/RSJ International Conference on Intelligent Robots and Systems*, 2010.

[5] R. Ünal, S. Behrens, R. Carloni, E. Hekman, S. Stramigioli, and H. Koopman, "Prototype design and realization of an innovative energy efficient transfemoral prosthesis," in *Proceedings of the IEEE/RAS-EMBS International Conference on Biomedical Robotics and Biomechatronics*, 2010.

[6] R. Ünal, R. Carloni, E. Hekman, S. Stramigioli, and H. Koopman, "Biomechanical conceptual design of a passive transfemoral prosthesis," in *Proceedings of the IEEE/EMBS International Conference on Engineering in Medicine and Biology, 2010*, 2010.

[7] A. van der Schaft, L_2*-Gain and Passivity Techniques in Nonlinear Control*. Springer, 2000.

[8] S. H. Strogatz, *Nonlinear Dynamics and Chaos*. Addison-Wesley, 1994.

[9] S. Wiggins, *Introduction to Applied Nonlinear Dynamical Systems and Chaos*. Springer-Verlag, 1990.

[10] H. K. Khalil, *Nonlinear Systems*. Prentice-Hall, 1996.

[11] M. van Dijk and S. Stramigioli, "Energy efficient limit cycle oscillation," in *Proceedings of the IFAC World Congress, 2008*, 2008.

[12] M. Jafarian, "Variable stiffness actuator for robust and energy efficient planar bipedal locomotion," 2010, MSc Thesis.

[13] T. McGeer, "Passive dynamic walking," *International Journal of Robotics Research*, vol. 9, no. 2, pp. 62–82, 1990.

[14] M. Wisse, *Essentials of dynamic walking*. PhD Dissertation, Technical University of Delft, 2004.

[15] G.-B. Stan, *Global analysis and synthesis of oscillations: a dissipativity approach.* PhD Dissertation, Universite de Liege, 2005.

[16] A. Goswami, B. Thuilot, and B. Espiau, "A study of the passive gait of a compass-like biped robot: symmetry and chaos," *International Journal of Robotics Research*, vol. 17, no. 12, pp. 1282–1301, 1998.

[17] J. Rummel, Y. Blum, H.-M. Maus, C. Rode, and A. Seyfarth, "Stable and robust walking with compliant legs," in *Proceedings IEEE International Conference of Robotics and Automation*, 2010.

[18] D. Hobbelen, *Limit cycle walking*. PhD Dissertation, Technical University of Delft, 2008.

[19] M. Garcia, A. Chatterjee, A. Ruina, and M. Coleman, "The simplest walking model: stability, complexity, and scaling," *ASME Journal of Biomechanical Engineering*, vol. 120, pp. 281–288, 1998.

[20] V. Duindam and S. Stramigioli, *Modeling and Control for Efficient Bipedal Walking Robots: A Port-Based Approach*. Springer, 2009.

[21] D. Ruspini and O. Khatib, "Collision/contact models for dynamic simulation and haptic interaction," in *In 9th International Symposium of Robotics Research (ISRR99), Snowbird*, 1999, pp. 185–195.

[22] N. Diolaiti, C. Melchiorri, and S. Stramigioli, "Contact impedance estimation for robotic systems," *IEEE Transactions on Robotics*, vol. 15, pp. 925–935, 2005.

[23] Controllab Products B.V. (2011) 20-sim. [Online]. Available: http://www.20sim.com

[24] T. McGeer, "Passive walking with knees," in *Proceedings IEEE International Conference on Robotics and Automation*, 13-18 1990.

[25] B. Vanderborght, R. van Ham, D. Lefeber, T. Sugar, and K. Hollander, "Comparison of mechanical design and energy consumption of adaptable, passive-compliant actuators," *International Journal of Robotics Research*, vol. 28, no. 1, pp. 90–103, 2009.

[26] V. Duindam, A. Macchelli, S. Stramigioli, and H. Bruyninckx, *Modeling and Control of Complex Physical Systems*. Springer, 2009.

[27] S. Stramigioli, *Modeling and IPC Control of Interactive Mechanical Systems: a Coordinate-free Approach*. Springer, 2001.

[28] L. C. Visser, R. Carloni, R. Ünal, and S. Stramigioli, "Modeling and design of energy efficient variable stiffness actuators," in *Proceedings of the IEEE International Conference on Robotics and Automation*, 2010.

[29] L. C. Visser, R. Carloni, and S. Stramigioli, "Variable stiffness actuators: a port-based analysis and a comparison of energy efficiency," in *Proceedings of the IEEE International Conference on Robotics and Automation*, 2010.

[30] ——, “Energy efficient variable stiffness actuators,” 2010, submitted to IEEE Transactions on Robotics.

[31] A. Jafari, N. Tsagarakis, B. Vanderborght, and D. Caldwell, “Minimizing energy consumption through optimal mechanical design and stiffness regulation,” in *Workshop for Young Researchers on Human-Friendly Robotics*, 2009.

[32] G. Tonietti, R. Schiavi, and A. Bicchi, “Design and control of a variable stiffness actuator for safe and fast physical human/robot interaction,” in *Proceedings of the IEEE International Conference on Robotics and Automation*, 2005.

[33] S. Wolf and G. Hirzinger, “A new variable stiffness design: Matching requirements of the next robot generation,” in *Proceedings of the IEEE International Conference on Robotics and Automation*, 2008.

[34] H. Nijmeijer and A. van der Schaft, *Nonlinear Dynamical Control Systems*. Springer, 1990.

[35] M. W. Griffis, “Kinestatic control: A novel theory for simultaneously regulating force and displacement,” Ph.D. dissertation, University of Florida, 1991.

[36] A. Jafari, N. Tsagarakis, B. Vanderborght, and D. Caldwell, “A novel actuator with adjustable stiffness (AwAS),” in *Proceedings of the IEEE/RSJ International Conference on Intelligent Robots and Systems*, 2010.

[37] B.-S. Kim and J.-B. Song, “Hybrid dual actuator unit: A design of a variable stiffness actuator based on an adjustable moment arm mechanism,” in *Proceedings of the IEEE International Conference on Robotics and Automation*, 2010.

[38] J. Hurst, J. Chestnutt, and A. Rizzi, “An actuator with physically variable stiffness for highly dynamic legged locomotion,” in *Proceedings of the IEEE International Conference on Robotics and Automation*, 2004.

[39] R. Schiavi, G. Grioli, S. Sen, and A. Bicchi, “VSA-II: A novel prototype of variable stiffness actuator for safe and performing robots interacting with humans,” in *Proceedings of the IEEE International Conference on Robotics and Automation*, 2008.

[40] L. C. Visser, R. Carloni, and S. Stramigioli, “Energy efficient control of robots with variable stiffness actuators,” in *Proceedings of the IFAC International Symposium on Nonlinear Control Systems*, 2010.

[41] F. Bullo and A. Lewis, *Geometric Control of Mechanical Systems*. Springer, 2004.

[42] A. Ben-Israel and T. Greville, *Generalized Inverses*. Springer, 2003.

[43] T. McMahon and G. Cheng, “The mechanics of running: How does stiffness couple with speed?” *Journal of Biomechanics*, vol. 23, no. 1, pp. 65–78, 1990.

[44] C. Farley and O. Gonzalez, “Leg stiffness and stride frequency in human running,” *Journal of Biomechanics*, vol. 29, no. 2, pp. 181–186, 1996.

[45] B. Vanderborght, B. Verrelst, R. V. Ham, M. V. Damme, D. Lefeber, B. M. Y. Duran, and P. Beyl, "Exploiting natural dynamics to reduce energy consumption by controlling the compliance of soft actuators," *Journal of Robotics Research*, vol. 25, no. 4, pp. 343–358, 2006.

[46] J. Pratt and G. Pratt, "Exploiting natural dynamics in the control of a planar bipedal walking robot," in *Proceedings of the Annual Allerton Conference on Communication Control and Computing*, 1998.

[47] S. Miyakoshi and G. Cheng, "Ballistic walking by compass-like biped walker-exploiting physical dynamics in achieving human-like walking," in *Proceedings of the 5th International Conference on Climbing and Walking Robots and the Support Technologies for Mobile Machines*, 2002.

[48] J. Pratt, "Exploiting inherent robustness and natural dynamics in the control of bipedal walking robot," Ph.D. dissertation, Massachusetts Institute of Technology, 2000.

[49] S. A. Migliore, E. A. Brown, and S. P. DeWeerth, "Biologically inspired joint stiffness control," in *Proceedings of the IEEE International Conference on Robotics and Automation*, 2005.

[50] J. Yamaguchi, D. Nishino, and A. Takanishi, "Realization of dynamic biped walking varying joint stiffness using antagonistic driven joints," in *Proceedings of the IEEE International Conference on Robotics and Automation*, 1998.

[51] M. G. Catalano, G. Grioli, F. Bonomo, R. Schiavi, and A. Bicchi, "VSA-HD: From the enumeration analysis to the prototypical implementation," in *Proceedings of the IEEE/RSJ International Conference on Intelligent Robots and Systems*, 2010.

[52] B. Vanderborght, N. Tsagarakis, C. Semini, R. van Ham, and D. Caldwell, "MACCEPA 2.0: Adjustable compliant actuator with stiffening characteristic for energy efficient hopping," in *Proceedings of the IEEE International Conference on Robotics and Automation*, 2009.

[53] R. V. Ham, B. Vanderborght, M. V. Damme, B. Verrelst, and D. Lefeber, "MACCEPA, the mechanically adjustable compliance and controllable equilibrium position actuator: Design and implementation in a biped robot," *Robotics and Autonomous Systems*, vol. 55, no. 10, pp. 761–768, 2007.

[54] J. Hurst and A. Rizzi, "Series compliance for robot actuation: Application on the electric cable differential leg," *IEEE Robotics and Automation Magazine*, 2008.

[55] O. Eiberger, S. Haddadin, M. Weis, A. Albu-Schäffer, and G. Hirzinger, "On joint design with intrinsic variable compliance: Derivation of the DLR QA-joint," in *Proceedings of the IEEE International Conference on Robotics and Automation*, 2010.

[56] A. Albu-Schäffer, O. Eiberger, M. Grebenstein, S. Haddadin, C. Ott, T. Wimböck, S. Wolf, and G. Hirzinger, "Soft robotics," *IEEE Robotics and Automation Magazine*, vol. 15, no. 3, pp. 20–30, 2008.

[57] N. Tsagarakis, A. Jafari, and D. Caldwell, "A novel variable stiffness actuator: Minimizing the energy requirements for the stiffness regulation," in *Proceedings of the IEEE/EMBS International Conference on Engineering in Medicine and Biology*, 2010.

[58] A. Jafari, N. Tsagarakis, and D. Caldwell, "Awas-ii: An novel actuator with adjustable stiffness based on variable lever arm ratio and moving pivot principle," in *Proceedings of the IEEE International Conference of Robotics and Automation*, 2011.

[59] G. van Oort and S. Stramigioli, "Geometric interpretation of the zero moment point," in *Proceedings of the IEEE International Conference of Robotics and Automation*, 2011.

[60] M. Vukobratović and B. Borovac, "Zero-moment point — thirty five years of its life," *International Journal of Humanoid Robotics*, vol. 1, no. 1, pp. 157–173, 2004.

[61] R. S. Ball, *A treatise on the theory of screws*. Cambridge University Press, Cambridge, 1900.

[62] M. Vukobratović and D. Juričić, "Contribution to the synthesis of biped gait," *Proc. IFAC Symp. Technical and Biological Problem and Control*, 1968.

[63] ——, "Contribution to the synthesis of biped gait," *IEEE Transaction on Bio-Medical Engineering*, vol. 16, no. 1, 1969.

[64] A. Dasgupta and Y. Nakamura, "Making feasible walking motion of humanoid robots from human motion capture data," in *IEEE International Conference on Robotic and Automation*, 1999, pp. 1044–1049.

[65] P. Sardain and G. Bessonnet, "Forces acting on a biped robot. center of pressure-zero moment point," *Systems, Man and Cybernetics, Part A: Systems and Humans, IEEE Transactions on*, vol. 34, no. 5, pp. 630 – 637, sept. 2004.

[66] K. Harada, S. Kajita, K. Kaneko, and H. Hirukawa, "Zmp analysis for arm/leg coordination," in *Intelligent Robots and Systems, 2003. (IROS 2003). Proceedings. 2003 IEEE/RSJ International Conference on*, vol. 1, 27-31 2003, pp. 75 – 81.

[67] M. Vukobratović, B. Borovac, and D. Surdilovic, "Zero-moment point — proper interpretation and new applications," *International Conference on Humanoid Robots*, 2001.

[68] A. Goswami, "Postural stability of biped robots and the foot-rotation indicator (FRI) point," *I. J. Robotic Res.*, vol. 18, no. 6, pp. 523–533, 1999. [Online]. Available: http://ijr.sagepub.com/cgi/content/abstract/18/6/523

[69] R. M. Murray, Z. Li, and S. S. Sastry, *A Mathematical Introduction to Robotic Manipulation*. CRC, March 1994. [Online]. Available: http://www.worldcat.org/isbn/0849379814

[70] R. Featherstone, *Rigid Body Dynamics Algorithms*. Secaucus, NJ, USA: Springer-Verlag New York, Inc., 2007.

[71] T. Takenaka and T. Hasegawa, "Gait generation system for a legged mobile robot," *US Patent 5357433*, 1994.

[72] S. Stramigioli and H. Bruyninckx, “Geometry of dynamic and higher-order kinematic screws,” in *Proc. International Conference on Robotics and Automation*, 2001, pp. 3344–3349.